Politecnico di Milano

SCUOLA DI INGEGNERIA INDUSTRIALE E DELL'INFORMAZIONE

Laurea Magistrale – Ingegneria Aeronautica

Hydrodynamic design of an autonomous underwater glider

Relatore

Prof. Maurizio BOFFADOSSI

Candidato

Lorenzo Maria BIRKMAIER – 945930

Anno Accademico 2021 – 2022

Contents

List of Figures

List of Tables

Listings

Sommario

L'obiettivo di questo progetto è quello di sviluppare un concept di AUG (Autonomous Underwater Glider). Inizialmente è stata fatta un'analisi dello stato dell'arte, con il quale sono state determinate le principali caratteristiche dei glider attualmente in commerico in funzione delle loro possibili tipologie di missione. A seguito di uno studio della dinamica di volo di questi sistemi, sono stati definiti i parametri fondamentali per il design idrodinamico. Da lì si è passati alla progettazione dello scafo, cercando di massimizzare la percentuale di flusso laminare che lo investe. Per fare ciò, l'ostacolo maggiore è stata la predizione della transizione del flusso, per la quale sono stati utilizzati i criteri di Granville e la trasformazione di Mangler, utili nel caso di corpi assialsimmetrici. In seguito sono state progettate le ali senza un vincolo di simmetria, diversamente da tutti i modelli di AUG attualmente in commercio. I principali software utilizzati sono stati xFoil e Athena Vortex Lattice, i quali sono basati sulle teorie dell'aerodinamica classica, quali la teoria del flusso potenziale, dei profili sottili e della linea portante. Infine sono stati fatti degli studi di CFD per avere un termine di paragone per i risultati sullo scafo, dato che la transizione del flusso rimane uno degli aspetti più delicati e difficili da predire.

Lo studio delle ali ha prodotto risultati positivi, con apprezzabili miglioramenti delle performance idrodinamiche, grazie soprattutto ad un approccio al problema diverso che ha permesso di aggirare il vincolo di simmetria delle ali, mentre nel caso dello scafo i risultati sembrano essere promettenti, ma richiedono uno studio più approfondito, possibilmente con delle prove sperimentali.

Abstract

The aim of this project is to develop a concept of AUG (Autonomous Underwater Glider). Initially, an analysis on the state of the art was made, through which the main characteristics of the gliders currently on commerce were determined as a function of their possible missions. Following a study on the flight dynamics of these systems, the fundamental parameters for the hydrodynamic design were defined. From this point, the plan of the hull was tackled, with the aim to maximize the portion of laminar flow over it. To do so, the biggest obstacle was the prediction of flow transition, for which Granville's criteria and Mangler's transformation were used, devised specifically for axialsymmetric bodies. Afterwards, the wings were designed without a symmetry constraint, opposed to all the other commercially available models. The main softwares used for this task were xFoil and Athena Vortex Lattice, which are based on classical aerodynamics theories, such as potential flow theory, thin airfoil theory and lifting line theory. Finally, a series of CFD analyses was made in order to have a term of comparison for the hull results, since flow transition remains one of the most delicate aspects to predict.

The wing design has produced positive results, with noticeable improvements in hydrodynamic performances, due especially to the different approach to the problem which allowed to bypass the symmetry constraint, while in the case of the hull the results do seem promising, but require a more in depth study, possibly with some experimental tests.

Introduction

The work described in the following chapters revolves around the design process of an Autonomous Underwater Glider, a type of unmanned submarine which, rather than a conventional propeller, uses a combination of variable buoyancy and the action of wings to attain a specific "saw-tooth" motion. This motion has a velocity with an approximately constant longitudinal component and a direction alternating vertical component. These devices have been gaining popularity since the beginning of the century for oceanographic research and monitoring, mainly due to their economical advantages and their convenient motion, which allows them to retrieve data samples from a wide range of depths. This data may be helpful for marine ecological preservation, a topic which has been gaining more traction. Furthermore, in recent years, by mounting microphone arrays on AUGs, the study of marine mammals has undergone a small revolution, as these can be tracked much more easily now. An additional use may be for military research, as knowledge of specific waters in certain regions can help optimize the ability of submarines to operate within them.

History and principles of operation

The first concept of an underwater glider was developed by General Dynamics Corporation in the 1960s, known as the Concept Whisper. This vehicle required the presence of two pilots to power it. Effectively it was a DPV (Diver Propulsion Vehicle) rather than an AUG (Autonomous Underwater Glider), but it introduced some of the ideas that characterize modern unmanned models. The two main concepts were those of buoyancy propulsion and sawtooth motion. By varying its buoyancy, a glider can travel vertically, by alternately becoming more and less dense than water. Through the use of hydrofoils, it can also produce a longitudinal component to its velocity, creating the aforementioned “sawtooth motion”, shown in Figure 1.

The exact mechanism through which the Concept Whisper changed its buoyancy is unclear, as most of the papers talking about it are still confidential, but the fact

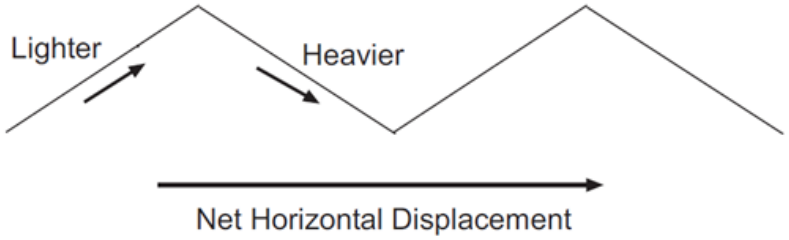

Figure 1: Simplified sketch of the trajectory of an autonomous underwater glider.

that it was powered by man can suggest that its missions were not designed to be very long, and as a matter of fact its purpose was that of a swimmer delivery vehicle, rather than the more common oceanographic research purposes of modern AUGs. The idea did not have many further developments, as variable buoyancy systems are generally very slow in their longitudinal motion, rendering them less than ideal for transportation missions.

About twenty years passed before a new interest in underwater gliders re-emerged. Doug Webb, who in the 1980's was working on buoyancy variability systems for floats, had an idea which would be the base of the modern AUGs and especially the Slocum Thermal. His idea was to render the buoyancy systems more efficient by garnering energy from the temperature gradient present in the ocean. A specific type of fluid would be used which would expand or shrink depending on its temperature, activating a pump which would change the buoyancy of the float (how this mechanism works will be described shortly). In general, floats descend to a certain depth, take various measurements for a certain amount of time, then descend even further for another amount of time before resurfacing and transmitting the data that they gathered. Webb's system would not allow a float to stay at the same depth for extended amounts of time though, so he started thinking of other systems to gather oceanographic information and had the idea of an autonomous underwater glider. He shared his idea with Henry Stommel, who to this day is considered one of the most important oceanographers in history. In 1988 the two developed a concept of underwater glider called Slocum, after Joshua Slocum, the first man to circumnavigate the globe by himself. In 1989 Stommel published an article on the journal "Oceanography" called "The Slocum mission", a fictional story set in the distant future of 2021, in which an oceanographer describes a sea monitored by thousands of underwater gliders. The technical characteristics of these gliders and their missions were very well defined: they would continuously move vertically through a buoyancy propulsion system and they would translate horizontally though the use of wings, transmitting their data to a satellite and

getting new route information at the end of each dive-ascent cycle. The gliders would then be able to control their pitch and roll through an internal ballast and would be able to travel at speeds of half a knot, equivalent to roughly 0.25 m/s. The article really succeeded in bringing attention on these gliders, especially by pointing out their economy and range.

Throughout the 1990's Webb's company, Webb Research Inc, produced prototypes that over the years accumulated new feats, such as dives of 1000 meters and an autonomy of up to 4000 kilometers. In parallel to them, other gliders such as the SeaGlider, the Spray and the SeaExplorer were developed. The first AUG to be available commercially was the Slocum Electric, in 2002. This glider was powered by electric batteries, rather than through the ocean's thermal gradient, but since then Thermal variant has also been produced.

Since then, more AUGs have been developed and they have become the main tool for oceanographic research. Besides their cost-effectiveness, their greatest advantage for such tasks comes from the sawtooth motion, which allows them to sample data at different depths on temperature, pressure, salinity, chlorophyll luminescence and so on. This data can be used for environmental studies or even for military use. In the past decade, these vehicles have also gained the attention of marine biologists, who have found use in them to track marine mammals by mounting hydrophone arrays on the gliders, as they are cheaper to operate than conventional naval expeditions and can operate even under adverse weather conditions. Further uses have also been proposed, such as monitoring areas where it is forbidden to transit or to fish.

Main aspects and components

Besides the sawtooth motion of the glider, one of the most critical aspects is the speed at which it travels. The vast majority do not travel at more than 1.0-1.5 m/s, with some going as slow as 0.2 m/s. Even though water has a larger kinematic viscosity compared to air, the Reynolds number is quite small, ranging in the order of 10^4 for the airfoils and 10^5 for the hull. Therefore large parts of the flow surrounding the glider might be laminar. In addition, unlike most other gliders, a very high glide ratio is generally not very desirable for the types of missions in which they are employed.

The majority of AUGs have a relatively simplistic shape. The main hydrodynamic components are the hull, the wings and the rudder. The most simplistic hull shape which can be found among commercial gliders can be recognized especially on the Slocum Glider, where The section remains constant throughout most of the body, except for the nose and the tail, which only take a small fraction of the total

length. Other hulls' cross-sections, such as the one of the SeaGlider, instead have a gradient, with an radius widening until it reaches the half-point of the hull, which allows to maintain a laminar flow without the formation of transition bubbles or boundary layer separation. Of course, the optimal shape will vary depending on the mission profile. The wings generally do not have a smooth connection with the fuselage. Most of them have a simple tapered shape or even a constant chord, with a sweep angle that varies depending on the length of the wings: the shorter they are, the less they will be swept. None of the most popular models have any control surfaces on the wings. The airfoils tend to be very thin, as it favors low Reynolds flows. In some cases, even simple thin plates are used, since their behavior is not as affected by changes in the Reynolds number. Most gliders, apart from the SeaExplorer, have a rudder, although it is not always steerable.

Inside the hull, the major components will be the buoyancy engine, the battery pack, the onboard computers and the payload, which is most commonly comprised of various sensors and transducers. The battery pack, which is also the heaviest part of the glider, is commonly split in multiple parts, which are going to be used as ballasts, allowed to move along the longitudinal axis of the glider to control its pitch, or to rotate, in the case of asymmetrical ballasts, allowing the vehicle to roll. The disposition of these masses is a critical aspect for the dynamics of the glider, as these will be extremely sensible to the position of the center of gravity. Below is shown a plan of the Spray Glider, which summarizes the most common characteristics of such a vehicle.

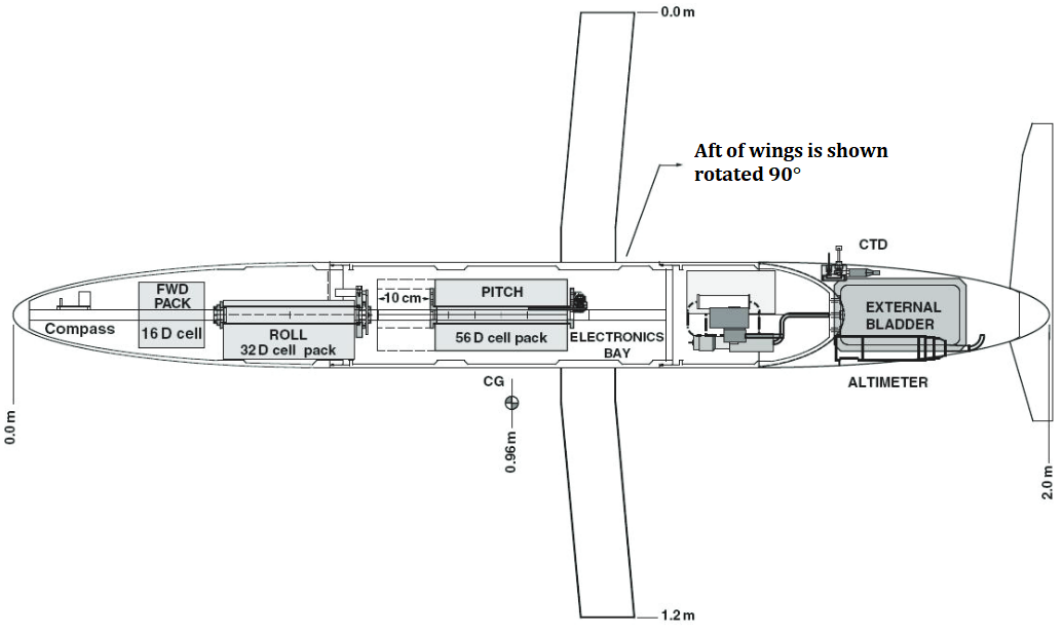

Figure 2: Plan of the Spray glider.

Before moving on, it is also important to understand how the buoyancy engine

operates. In general, the total volume of the glider will remain more or less unchanged, neglecting the variation caused by the pressure increase at the lower depths. The way that the glider will change its buoyancy will therefore be by a variation of its mass. In its initial condition, the whole glider system will have a specific weight which is slightly lighter than that of water, allowing it to float. It will then start intaking water, which will increase its weight and make it sink, initiating the dive. Once the deepest point of the dive is reached, the buoyancy engine is activated, inflating a bladder with oil or water coming from a high-pressure reserve. The bladder will then expel the seawater that the glider first accumulated, making it positively buoyant once again and allowing its climb. Once it reaches the surface again, the bladder will deflate, allowing for the glider to intake seawater again and repeat the whole process. The buoyancy engine therefore only has to work at the highest and lowest points of the trajectory of the glider. Therefore, besides the actual efficiency of the pumps, what will have a significant impact on the range of the glider's mission will be the depth of each dive, its glide ratio, and the volume of water that will be displaced at each cycle.

Problems and challenges

Although the gliders operate in water, their design process can have a similar structure to that of a conventional aircraft and can therefore be divided in the following categories: hydrodynamics, propulsion, flight dynamics, control, weights and structures.

For hydrodynamics, the main challenges are related to the low Reynolds number at which the AUG operates. Drag coefficients tend to be larger at lower Re, gradually decreasing until reaching an approximately constant level only at Re circa equal to $10^6 - 10^7$, depending on the shape of the specific body. Around airfoils, the formation of transition bubbles can be extremely detrimental to the hydrodynamic efficiency. Therefore an appropriate solution must be found by conveniently sizing the glider and by studying ideal airfoil shapes. In addition, the airfoils will need to be symmetrical, since the roles of the upper and lower surfaces will reverse between the climb and dive phases.

Contrary to standard aircraft, the propulsion system of an underwater glider will have no direct effect on the hydrodynamics, and in fact it will tend to be active only in the proximity of the peaks of the glider's trajectory. However, there are different strategies for the intake and release of water from the hull, so the most efficient system must be determined. In addition, a convenient location within the hull must be located, keeping in mind that a considerable amount of volume will be taken by the propulsion system. In general, it will be either at the tail or at

the nose (or both in some cases), depending on where it is more convenient for the control system.

The development of a dynamic model of the glider will be one of the first steps towards the definition of the concept. In this case the vehicle is maneuvered by moving the masses in the hull and the consequent center of gravity, rather than by moving control surfaces, so the model will have to be capable of determining the effects of the displacements of the ballasts and allow to make an assessment on an ideal sizing to obtain determined flight characteristics. In the course of this work, latero-directional dynamics will only be touched upon briefly, while the main focus will be on longitudinal dynamics.

The weights problem is a particularly critical one. To maximize efficiency, the intake of water when starting the dive must be very low. To give an idea, the Slocum Glider, which weighs approximately 60 kg, can potentially initiate a dive through a change in buoyancy of 25 grams. This means that it is fundamental to make an estimate of the total weight and volume of the concept glider from the very beginning, so that it can have a density as close as possible to that of saltwater. In general, the AUGs will tend to be slightly lighter than water, since it is always possible to just add some extra weight if necessary. The criticality of weights is further amplified by the fact that the problem is strongly coupled with those associated with propulsion, flight dynamics, control and structures.

Finally, the structural problem is quite different compared to that of conventional aircraft. While normally the most critical aspect is the bending moment and the displacement of a wing, in the case of an underwater glider the loads that the wings have to withstand are minimal. The lift and drag forces have to balance the difference between buoyancy and gravity which, even for reasonably large gliders, will hardly ever be larger than 10 N. The constraints will be posed on the design of the fuselage, which will have to be able to withstand pressures at depths of hundreds of meters (if not thousands, in certain cases).

Unfortunately, most of the problems described are coupled and in an industrial context require the collaboration of several departments. In general, the development of a new vehicle takes several years, tens of engineers with various specializations, and large amounts of funding. So, unless the prototype is a completely new concept developed for an unprecedented mission, it is better to base its design (or part of it) on previous models, on which appropriate changes will be made to better suit the specific mission requirements. For this purpose, some of the most popular underwater gliders will be examined.

Outline

In the following, the contents of this thesis are summarized chapter by chapter. It is thus structured:

Chapter One deals with the state of the art, with a description of the main qualities and missions of each of the most commercially successful AUG models currently available. From that basis, the mission profile and the minimum qualities required by the model to be designed will be listed.

Chapter Two is tasked with the description of the dynamics acting upon a generic underwater glider. The reference frames are described and the kinematic equations that relate them are derived. After that, the translational and rotational equilibrium equations are obtained and the external forces and torques are reported. At this point the focus is posed in particular on the longitudinal dynamics, which describe the most basic and common motion of an AUG, the steady descending or ascending glide. From the equations of longitudinal motion, the relations between angle of attack, bank angle, buoyant mass and center of gravity will be highlighted, along with the importance of the hydrodynamic efficiency of the glider.

Chapter Three deals with the hydrodynamic design and optimization of the hull. The focus will be on the minimization of parasitic drag, and a calculation method for it will be devised in order to avoid using computationally expensive CFD. An optimization process will then be actuated in order to obtain a near optimal solution. After that, the results from the model devised will be compared with some experimental and numerical data in order to assess its accuracy.

Chapter Four will then move on to the design of the wings. A method to assess the best airfoil will be described and once it is found, an optimization procedure will be actuated through the use of XOptFoil, a software which interfaces with xFoil. From some initial estimates, an optimal planform will also be developed through the use of the softwares Athena Vortex Lattice, Matlab and Python.

Chapter Five will report the procedure of CFD analysis done on the finalized concept, mainly to give a second check to the predictions on hull drag and compare the results obtained from different calculation methods. Initially, a study on the airfoils will also be made to assess the best turbulence model to use in the RANS equations.

Chapter 1

State of the Art

1.1 Commercial AUGs

In the next few paragraphs, the main commercial models, their characteristics, and their main purposes will be described. The first gliders that will be dealt with will be the ones with a mission profile more similar to the one of the prototype to be designed. Other models will be also described to see how different mission profiles affect the overall design of the vehicle.

1.1.1 Slocum Electric glider

The Slocum glider[1][2] remains one of the most popular commercial models. Thanks to the possibility of applying customizations, the newer models can be adapted to operate at different conditions, therefore having a wide range of missions. Their main use is for oceanographic data sampling, although it has happened that some were also used by marine biologists to determine marine mammal locations and behavior, by mounting hydrophone arrays on the glider[3][4]. The maximum depth that the Slocum glider can reach is dictated by the buoyancy engine that is mounted on it. The smaller engine allows depths ranging from 4 to 150 meters, while the larger one is advised for missions of 40 to 1000 meters. Note that the depth rating is not dependent in this case by the shape of the glider, which remains unchanged. The length of the mission can also vary significantly, depending on a number of factors, mainly the type of batteries mounted. Alkaline batteries, the cheapest option, can allow missions to last 350-1200 km, or 15-50 days, rechargeable lithium batteries can allow a deployment of 700-3000 km, or 30-120 days, while lithium non rechargeable can last 3000-13000 km, or 4-18 months. These ranges, still quite wide, will mainly be dependent on two further variables: vehicle speed and maximum depth. A higher vehicle speed will make the deployment length shorter. In general, the average speed of the Slocum is between 0.15-0.5 m/s, although it can

increase to 1.0 m/s with the use of auxiliary thrusters, which have been available since the Slocum G3 model was released. As previously mentioned, the other aspect that has a significant impact on the efficiency of the glider is the depth at which it operates. Not only because different buoyancy engines have different efficiencies at different depths, but especially because a glider that reaches deeper waters will need to use the buoyancy engine less frequently.

The payload generally consists of a number of sensors, transducers or hydrophones, but for navigation and communication purposes, all Slocum gliders are equipped with an RF modem, an acoustic modem, a GPS system, a pressure sensor, an altimeter, and dead reckoning, which is a system that allows to determine the position in time of an object through an estimation of its position at an initial time and an estimation of the evolution of its velocity.

The geometry of the hull is quite simple, being mostly cylincrical with short nose and tail, a diameter of 0.22 m and a total length of 1.5 m. The shape of the wings is also very simple, as they are trapezoidal with a taper ratio of 0.5, with a total surface of $0.10m^2$, an aspect ratio of 7 and a back sweep of 43°. Rather than common airfoils, it used to employ simple thin plates (although the newer models do use symmetric profiles). The reason for this, other than practicality, will be explained in future chapters, and is related to the low Reynolds numbers at which it operates.

The total mass of the glider can vary between 55-70 kg, depending on the configuration of the glider. Such a wide variation is possible due to the fact that the payload can and may be mounted externally to the glider, increasing its overall buoyancy.

So overall, the design of the Slocum allows it to perform in a wide range of missions, although it is best suited for depths of 1000 meters, and velocities of 0.25 m/s. Its glide ratio is generally in the range of 2-3.

1.1.2 Slocum Thermal Glider

The Thermal variation[5] has a very similar design to the Slocum Electric glider. The shape of the hull and of the wings are identical, but the main difference is that the buoyancy engine is powered by harvesting energy from the ocean's temperature gradient. A reservoir of a particular wax which melts at low temperatures is used. The thermocline of the ocean causes it to change states from liquid to solid, shrinking it and allowing room for the passage of oil in the buoyancy engine. Therefore, even though electric batteries are still required to power the on-board computers and devices, the length of the mission is drastically increased, lasting up to 40000 km. Performances of the Slocum Thermal are nearly identical to its electric counterpart,

but there are downsides to the Thermal configuration. The main one is the lack of mission flexibility, since a certain amount of depth is required to reach a sufficient temperature decline. This condition limits also the environments in which it can operate to about two thirds of the world's seas. For example, in the Mediterranean Sea, where the temperature at a depth of 1000 meters can reach 13°, the glider would not be able to function.

To summarize, the Slocum Thermal is much more efficient and can travel far greater distances, but the mission profile range is going to be significantly limited. The rest of the specifics will not be mentioned and no picture of the inner components will be shown, as they are nearly identical to the previously described electric counterpart.

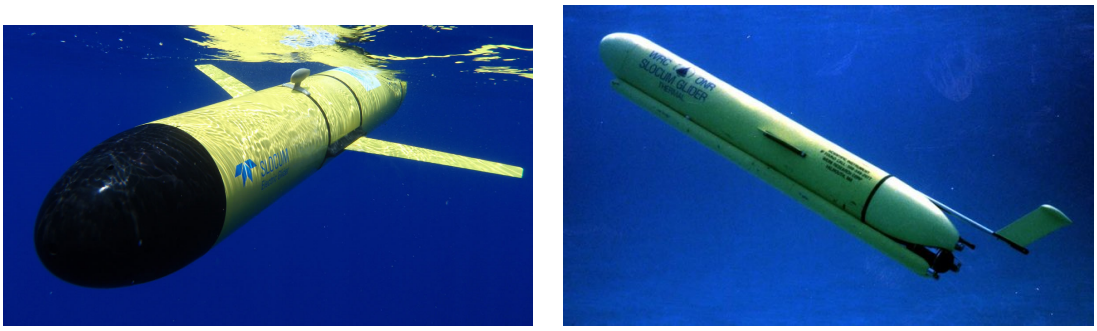

Figure 1.1: Slocum Electric and Thermal gliders in water.

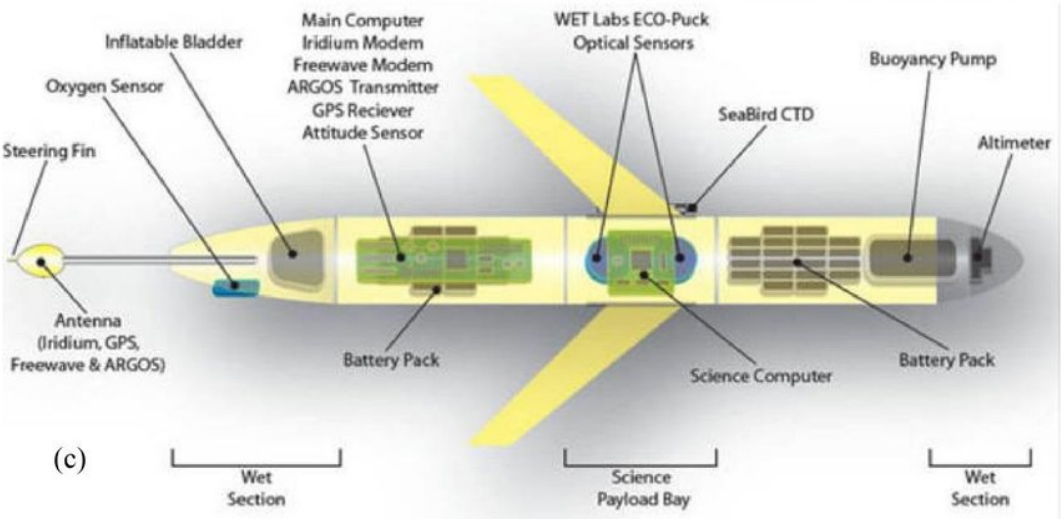

Figure 1.2: Internal components of the Slocum Electric Glider.

1.1.3 Spray

The Spray[6][7] is an autonomous underwater glider developed by Bluefin Robotics. Currently there are on average ten models deployed at any given time in the whole

world, mainly on the coasts of North America and in Oceania. Its missions are quite similar to those of the Slocum glider, so it is not surprising that it is quite similar also in overall design. Only one variant of buoyancy engine is present, with a maximum depth rating of 1500 meters. Only one type of battery pack is available, made by non-rechargeable lithium batteries, with a total storage of 17.5 MJ. This allows the glider to travel for a range of 3500-4800 km, or 4-6 months. The range depends mainly on the pitch angle of the glider, which varies between $18 - 25°$, meaning that the glide ratio is going to be approximately in the range of 2.1-3.1. For a pitch angle of 18° (glide ratio equal to 3.1) the glider's maximum distance travelled is optimized, while for a pitch angle of 25° (glide ratio equal to 2.1) the glider's velocity will be maximized. As one can expect, even in this case the velocity of the glider has a negative effect on the longevity of the mission. No auxiliary thrusters are available, and the velocity at which the Spray operates is in the range of 0.2-0.35 m/s. In order to reach these velocities, the buoyancy engine can vary its volume by $\pm 350cc$. Its empty weight is of 52 kg, making the ratio between total mass and variable mass circa 74:1.

An altimeter is not necessarily present, but can be included in the payload, which generally consists of at least a CTD sensor (Conductivity/Temperature/Depth) and transducers to measure dissolved oxygen, turbidity and fluorescence. In order to communicate and navigate, the glider is equipped with a compass, a GPS and waypoint boundary navigation, and an Iridium antenna placed on both wings. So when the glider reaches the surface, in order to communicate it doesn't lift its tail through the use of a buoyancy engine, but rolls 90°, allowing one of its antennas to resurface.

Although the shape of the hull is similar to that of the Slocum, it is not a perfect cylinder for most of the body, having a slightly more hydrodynamic shape. Its maximum diameter is 20 cm, and its total length is of 213 cm, making it slenderer than the Slocum glider. The wings on the other hand are even simpler, as they have a constant chord of 0.1 m, a span of 1.2 m and a sweep angle of 5°. Even in this case the airfoils are simple thin plates. The most notable difference with the Slocum model is the sweep angle, which is much more restrained.

1.1.4 SeaGlider

The SeaGlider[8], also known as the Deep Glider, was developed by the University of Washington, and is currently produced and marketed by Kongsberg Underwater Technology Inc. Besides its standard oceanographic research purposes, older models have notably been used to monitor the incident of the Deepwater Horizon oil spill and for detection by the US Navy[6], mostly for anti-submarine warfare. Its rated

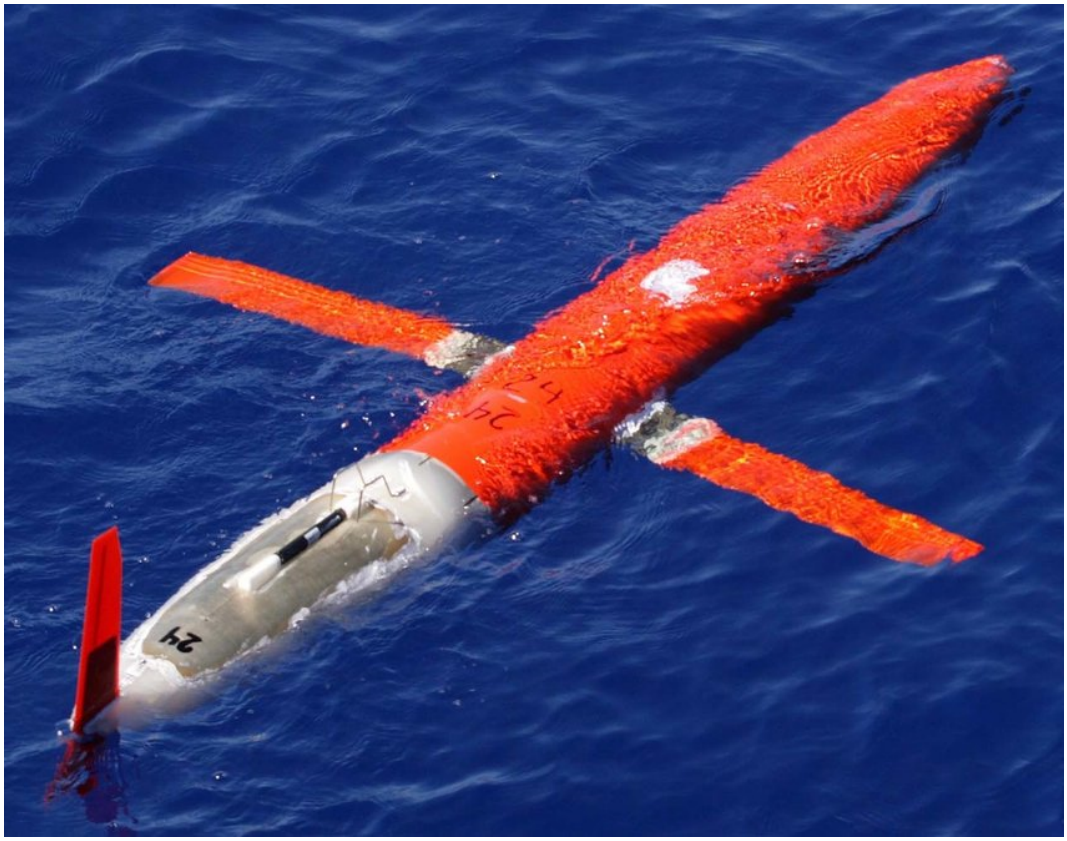

Figure 1.3: Spray glider in water.

depth is of 1000 meters. Its battery pack, made of lithium primary batteries, has a storage of 17 MJ, slightly less than the Spray. Nonetheless, even with the same energy storage and velocity, which is generally around 0.25 m/s for the Seaglider, its missions can last significantly longer, up to 10 months. Even in this case there are no auxiliary thrusters. In the previous models, there were two possible configurations, one with a single pump and one with a main pump and a booster pump. The first one was ideal to reach depths of 120 meters, while the second was better for deeper dives.

Currently two configurations are also available, but they are related to the payload. There is a standard configuration, with CTD sensors, antenna with Iridium and GPS, compass, acoustic altimeters, and an ogive configuration, which has a larger volume to store additional sensors, to measure things such as turbidity, dissolved oxygen, fluorescence etc. In order to navigate, the glider is commanded by the GPS system whenever it reaches the surface and makes use of Dead Reckoning when it is underwater. Its antenna is positioned past the tail, as shown in figure 1.4.

The empty weight of the glider ranges from 52-60 kg, depending on the configuration adopted, and its buoyancy is modulated through a bladder which can inflate

up to 850 cc, so the empty load to weight variability ratio is in the range of 60-70:1.

The hull has a much more peculiar shape than the other models. It is slimmer in the front and thicker in the aft section, with a maximum diameter of 30 cm. While the design is more complex and the manufacturing is not as simple, the advantage of such a shape is that it reduces drag. In its common operating conditions, the Reynolds numbers (referred to body length) are quite low, in the ranges of 500.000-1.000.000. Those numbers can be inconvenient, since drag can be larger at smaller Reynolds numbers. To improve performances, the design of the hull is so that for the majority of it there is a favorable pressure gradient, maintaining a laminar flow for over 70% of the body and minimizing drag. The wings have a trapezoidal shape, with a span of 1 meter, taper ratio of 0.5, a root chord of 0.24 m, a sweep angle at the leading edge of 16° and 0° at the trailing edge.

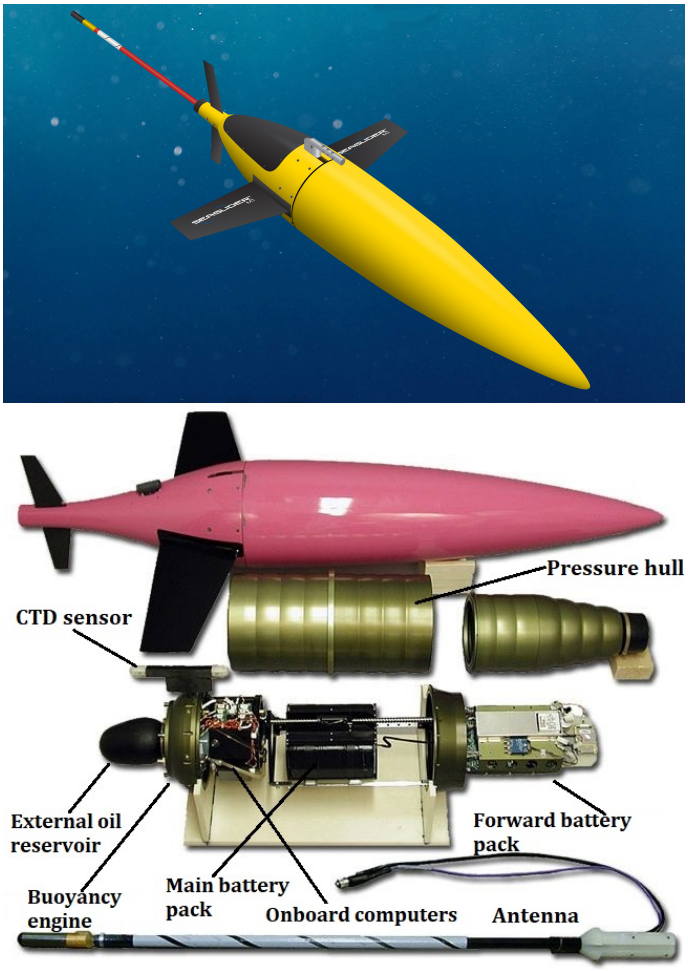

Figure 1.4: Render of the SeaGlider in water and overview of its components.

1.1.5 SeaExplorer

The SeaExplorer[9] is a French AUG produced by Alcen-Alseamar. Its main missions include oceanography research, detection of water pollution and anti-submarine warfare. One difference from other gliders is that the hull is composed of five sections rather than three, allowing the glider to be much more customizable. Its operational depth is of 1000 meters, although it is suited for both deep and shallow water missions. The battery pack, which just as in previous cases is used to control pitch and roll, is customizable, with the possibility to choose rechargeable lithium-ion or non-rechargeable lithium batteries. In general, while rechargeable batteries are more cost-effective, primary batteries have the advantage of lasting longer, mainly because of their high specific energy and their long storage times, making them indispensable in AUGs for longer uninterrupted missions. The SeaExplorer can travel 1300-3200 km, or 64-160 days, with a speed ranging from 0.25-0.5 m/s. Although no auxiliary thrusters or pumps are present in the glider, its buoyancy engine can produce a larger volume variability, of up to 1000 cc. This is to allow the glider to operate in waters with high density gradients and in the presence of stronger currents.

For communication and navigation, it uses a GPS, Iridium satellite, a radio triple antenna and an altimeter. Its payload is the most notable one, with the standard package having sensors for CTD, dissolved oxygen, turbidity, fluorescence, nitrates, pCO2 and an echosounder, with additional optional sensors for hydrocarbons, sewage, pesticides, methane, microturbulence, metal traces and a passive acoustic recorder.

The empty weight of the glider is of 59 kg, so the ratio between empty weight and variable weight is approximately 59:1.

Although the shape of the hull isn't as peculiar as that of the SeaGlider, it is still more complex than that of the Spray or the Slocum, having a length of 2 meters and a variable diameter that reaches a maximum of 25 cm at the middle of the body. The main distinguishing feature though is the absence of proper wings. Of course, although Alcen-Alseamar claims that the SeaExplorer is wingless, for forward propulsion in reality it does have lifting surfaces, but they are four small fins located at the aftbody, with symmetric dihedral angles and no control surfaces. According to the manufacturers, this design choice, more than for hydrodynamic advantages, is due to a lower risk of entanglements, breaks or damages.

Overall, the SeaExplorer, although it can also sustain long missions, and has been designed with the main idea of making it withstand more adverse conditions and environments, further expanding its range of mission profiles, as can also be deduced from the wide range of sensors with which it can be equipped.

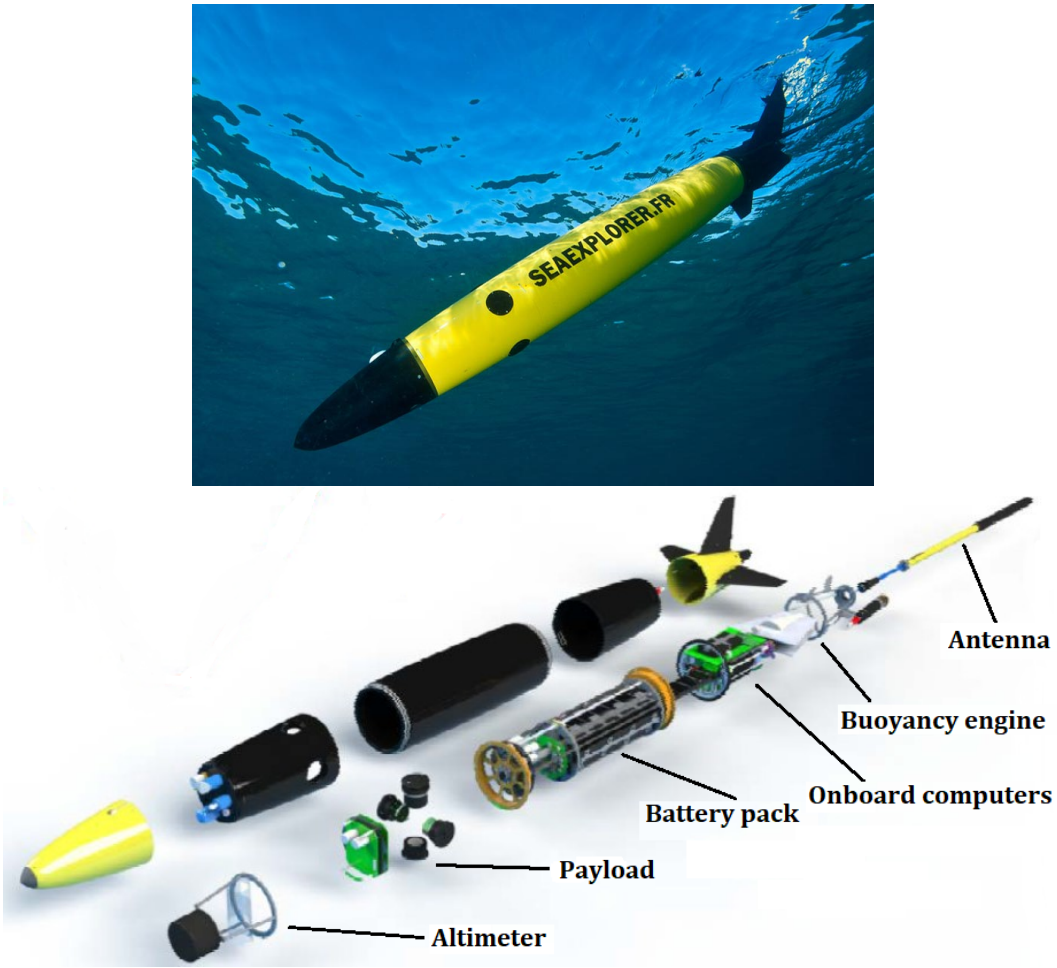

Figure 1.5: SeaExplorer in water and overview of its components.

1.1.6 Liberdade ZRay

The Liberdade ZRay[10] is quite different from all of the AUGs listed in this chapter. It is the culmination of the efforts by the US Navy, Scripps Institution of Oceanography, University of Washington, UT Austin, MIT, Penn State University, Woods Hole Oceanographic Institution, SAIC and Bluefin Robotics, and an evolution from the previous models Stingray, XRay1 and XRay2. It is an experimental vehicle, which vastly improves many of the features of the other gliders. Nonetheless, its large dimensions make it difficult to be used by a wide audience and significantly raise its cost, so unfortunately it is not commercially produced, and not a lot of data is available. The reason behind its mention is that it is the only blended wing underwater glider, so it is interesting to see its performances and main features. Blended wing vehicles in general have an improved aerodynamic (or hydrodynamic in this case) efficiency, mainly due to the reduction in interference drag and the more aero/hydrodynamic shape of the fuselage. But beside the increased manufacturing expenses, even the design process will be more complex, making a 2D study of the

performances impossible and thus requiring 3D CFD simulations even during the optimization process, which increases dramatically the computational costs. The final results though, in the case of the Liberdade ZRay, are remarkable. At a tested operational depth of 300 meters, it can glide at a speed of 0.5-1.5 m/s, a maximum velocity which is three times larger than the average AUG. More notably than that, its lift to drag ratio, or glide ratio, is 35:1, so even though it operates at much shallower depths, its missions can last up to 1500 km. Its wings can house an array of 27 hydrophones, vector sensors and electric field sensors. Its main mission is that of marine mammal tracking and detection of submarines. it is employed by the US Navy's Persistent Littoral Undersea Surveillance Network (PlusNet) system of unmanned surveillance vehicles.

What also gives a hydrodynamic advantage to the Liberdade ZRay is its size, which along the increased velocity contributes to dramatically increase the Reynolds number, avoiding the issue of a laminar flow hindering the maximum lift achievable. The wings have a span of 6.1 meters, and are highly tapered. Previous models also had winglets, which subsequently were discarded, possibly for the symmetricity requirements of the glider, making the hydrodynamic optimization useful only during the dive (although this is only speculations, since there is a lack of hard data). It has a dry weight of approximately 680 kg, so the displacement of the battery pack is not sufficient to give a good attitude control of the vehicle. Instead, it uses water jets for this purpose, which can also be used as propulsion when it is at the surface.

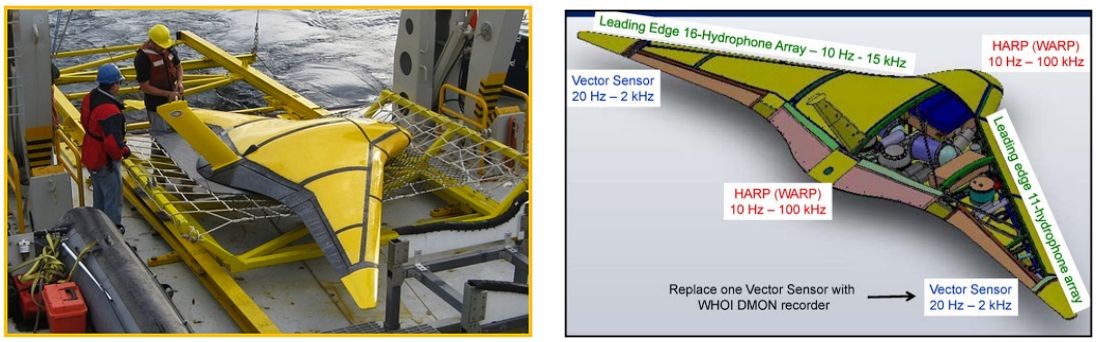

Figure 1.6: Liberdade ZRay in deployment and CAD of its inner components.

1.1.7 Folaga

The Folaga[11][12] is an AUV produced by GRAALTech, a laboratory of the University of Genoa. Its main characteristic is its payload modularity, which not only allows to select the type of sensors that one might want to use, but also the propelling system. The Folaga is more of an underwater vehicle in the broader

sense, equipped with both a propeller and a buoyancy engine, which can be used as a profiler, a glider or a standard AUV. Its modularity even allows it to operate with or without wings. Despite the simplistic design, this vehicle is the most versatile among the ones listed, when dealing with short range missions. In addition, thanks to its bi-directional rear thruster and its 8 jet-pumps, it is extremely maneuverable without the need for it to be in motion. The main uses for the Folaga in general are quick oceanographic assessments, bottom mapping, inspection and monitoring. It is also possible to use it to test control systems designed for academic or commercial purposes. It is more indicated to use along coasts, because of its relatively low depth rating, which is of 80 meters for the ROV (Remotely Operated Vehicle) mode and 50 meters for the AUG mode. Its battery pack can use lithium-ion or nickel-metal hybrid batteries, which in both cases are rechargeable, a more convenient solution since the missions tend to be shorter. The reason for the relatively low range (14 hours in AUV mode and several days in AUG mode) is the reduced dimensions of the vehicle, which has the shape of a simple tube, with a diameter of 15.5 cm and a length of 2.0 meters, reducing the space in which to allocate the battery pack. On the other hand, it is capable of reaching velocities of up to 1 m/s in glider mode and 2 m/s in AUV mode. Even when not using the thrusters, its gliding speed is higher than other gliders, even though the variable buoyant volume is 700 cc, in line with the Slocum model. The total dry mass of the Folaga is of 31 kg, making the ratio between it and the variable mass approximately 45:1.

The Folaga is equipped also with a GPS, radio, an acoustic modem, a depth-meter and a 3D inclinometer. To the payload it is also possible to add a CTD sensor, an optical sensor, a towed array and a sidescan sonar.

Figure 1.7: Folaga models with different payloads.

1.2 Summary of AUG characteristics

The following tables summarize all of the main characteristics of the gliders listed above.

Mission specifications				
Glider	**Depth Range**	**Endurance**	**Navigation**	**Applications**
Slocum E	4-200 m or 40-1000 m	350-1200 km (15-50 days)	GPS, altimeter, dead reckoning, RF modem	Oceanographic research, marine mammal detection
Slocum T	1000 m	40000 km	See Slocum E	See Slocum E
Spray	1500 m	3500-4800 km (4-6 months)	Compass, GPS, Iridium antenna	Oceanographic research
SeaGlider	120-1000 m	9000 km (10 months)	GPS, altimeter, Dead reckoning, Iridium antenna	Oceanographic research, oil spill detection, ASW
SeaExplorer	1000 m	1300-3200 km (64-160 days)	GPS, altimeter, Iridium antenna	Oceanographic research, pollution detection, ASW
ZRay	300 m	1500 km	Unknown	Marine mammal tracking, sea surveillance
Folaga	50-80 m	6-24 hours	GPS, acoustic modem, radio, 3D inclinometer	Oceanographic assessment, academic purposes

Table 1.1: Summary of the mission profiles of the various gliders.

Geometry				
Glider	**Hull length**	**Diameter**	**Wing surface**	**Wingspan**
Slocum E	1.5-2 m	0.22 m	0.1 m^2	1 m
Slocum T	See Slocum E	See Slocum E	See Slocum E	See Slocum E
Spray	2.13 m	0.2 m	0.12 m^2	1.2 m
SeaGlider	1.8 m	0.3 m	0.18 m^2	1 m
SeaExplorer	2 m	0.25 m	Wingless	(4 winglets)
ZRay	$\sim$ 2 m	Blended	6.1 m	Unknown
Folaga	2.0-2.2 m	0.155 m	Unknown	Unknown

Table 1.2: Summary of the mission profiles of the various gliders.

Weights and velocity				
Glider	**Weight**	**Buoyancy**	**Velocity**	**Payload**
Slocum E	55-70 kg	$\geq \pm 400\,cc$	0.5 m/s (1 m/s with thrusters)	Large, high modularity
Slocum T	See Slocum E	See Slocum E	See Slocum E	See Slocum E
Spray	52 kg	$\pm 350\,cc$	0.2-0.35 m/s	Large, low modularity
SeaGlider	52-60 kg	$\pm 425\,cc$	0.2-0.5 m/s	Large, medium modularity
SeaExplorer	59 kg	$\pm 500\,cc$	0.25-0.5 m/s	Large, low modularity
ZRay	680 kg	Unknown	0.5-1.5 m/s	Large, low modularity
Folaga	28-31 kg	$\pm 350\,cc$	1 m/s (2 m/s with thrusters)	Small, high modularity

Table 1.3: Summary of weights and consequent velocities of the gliders.

1.3 Mission profile

The models previously examined have a wide range of missions, in particular the Slocum, the SeaGlider, the Spray and the SeaExplorer, which also happen to be the most commercially successful. These gliders have been deployed along the coasts and seas of many countries. Even in Italy, despite the presence of GraalTech's Folaga, the most popular ones are the Slocum and the SeaGlider, most likely due to their considerably longer ranges. The AUG technology though is still relatively young and there are potentially many aspects which can be optimized. A major example is the simplicity of the wings and hull shape on the Slocum. Part of the simplicity in design is related to the low Reynolds numbers. In fact, the velocity and dimensions of the wings pose them at a Reynolds range in the tens of thousands, which is generally a critical zone in which there can be major differences in aerodynamic performances for conventional airfoils. The problem is not only caused by the fact that the Reynolds number is low, but also by its variability. In fact, between the surface level and a depth of 1000 m there can be a temperature gradient exceeding 20 K, which unfortunately greatly affects the kinematic viscosity of water. As an example, a wing with a chord length of 0.2 meters and a velocity of 0.5 m/s will have a Reynolds number of 10^5 when the freestream temperature is of 293 K, but for a temperature of 275 K the Reynolds number plummets to $6 \cdot 10^4$. To give an idea of the effect of such a difference, in figure 1.8 is a graph showing the variation of the aerodynamic efficiency as a function of the Reynolds number.

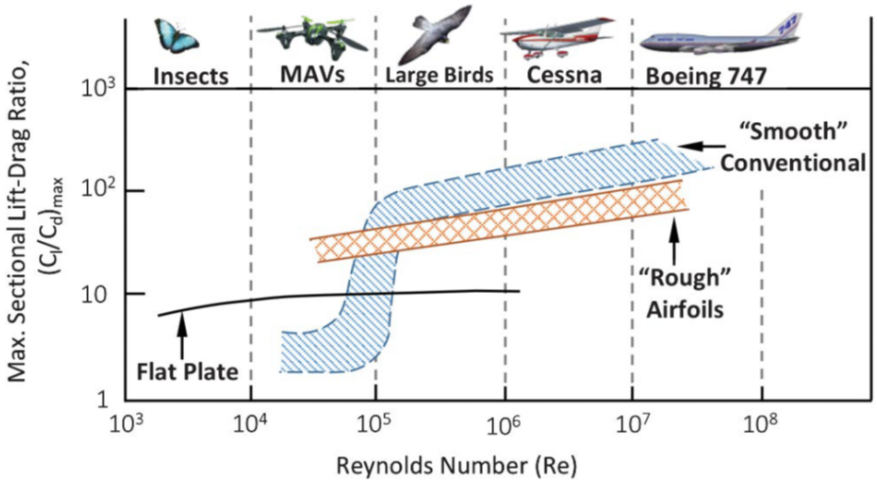

Figure 1.8: Maximum aerodynamic efficiency as a function of the Reynolds number for conventional smooth airfoils, rough airfoils and flat plates.

The graph explains the choice behind the employment of a thin plate as a wing on some gliders. Despite the worse performances at higher Reynolds numbers, it has a stable behaviour, allowing it to maintain fairly consistent performances at any depth.

The thermocline can also vary quite considerably for different seas and at different seasons. An example is the Mediterranean Sea, whose deeper waters have an average temperature of 285 K, meaning that the surface temperature may even be colder, depending on the season.

The goal of this project is therefore to design a glider which can improve the hydrodynamic efficiency of the current commercial models while maintaining most of their versatility. Following is a list of the characteristics which will be sought after.

Depth rating: The AUG must be capable of diving up to a depth of 1000 meters. This allows to travel a further distance with a single buoyancy pump cycle, to have a more varied measurement profile, but also to capture the sounds emitted by marine mammals such as beaked whales, which frequently dive to those depths to find food. The main components that are affected by this constraint are the shape and size of the pressure hull, which must withstand the pressures of about 10 MPa, and the buoyancy engine, whose functioning and efficiency also depends on the pressures at which it operates.

Velocity: There are no lower bounds on the velocity of the glider, in some cases it is useful to travel more slowly, either for efficiency reasons, or because the mission requires so (for example if the transducers employed have a low sampling rate). The maximum velocity reached by most commercial AUGs varies between 0.5 and 1.0 m/s. The maximum velocity reached by the glider depends mostly on the size of the buoyant mass, but of course the overall size and hydrodynamic properties of the hull and wings will also be influential on it.

Payload: The versatility of a mission is obviously related to the size of the payload, which allows to store a larger number of transducers, sensors, and measurement devices. Of course, this will influence the total volume of the glider and the mass distribution. Some gliders mount these devices externally, reducing the constraints but with a cost on hydrodynamic performances, since drag will increase.

Range: This aspect is perhaps the most alluring of AUGs, since they can run uninterrupted for months and thousands of kilometres. The range of a glider is highly dependent on its mission, which will determine its velocity, the number of active sensors and its depth range. For each mission though, the length of the deployment will be determined by the battery pack. This is the heaviest component of the glider, and considering that it is usually also used to vary the gravity centre of the AUG, its impact on the overall sizing of the vehicle will be considerable. Gliders such as the Spray and the SeaGlider have a battery pack with a capacity of 17 MJ, but with significant differences in total ranges. For the model to be designed in this project, a range to aim at, when considering a 1000 meters depth range and a velocity of 0.27 m/s, would be of at least 4 months, or 2800 km.

Chapter Bibliography

[1]William P.Barker, 2012, *An Analysis of Undersea Glider Architectures and an Assessment of Undersea Glider Integration Into Undersea Applications*, Naval Postgraduate School Thesis of Monterey California, page 11

[2]https://www.naval-technology.com/projects/slocum-underwater-glider/

[3]Mark F. Baumgartner, David M. Fratantoni, Thomas P. Hurst, Moira W. Brown, Tim V. N. Cole, Sofie M. Van Parijs, Mark Johnson, 2013, *Real-Time reporting of baleen whale passive acoustic detections from ocean gliders*, Acoustical Society of America, page 1815, DOI: 10.1121/1.4816406

[4]Pierre Cauchy, Karen J. Heywood, Denise Risch, Nathan D. Merchant, Bastien Y. Queste, Pierre Testor, 2020, *Sperm whale presence observed using passive acoustic monitoring from gliders of opportunity*, Endangered Species Research, Vol. 42, page 135, DOI: 10.3354/esr01044

[5]William P.Barker, 2012, *An Analysis of Undersea Glider Architectures and an Assessment of Undersea Glider Integration Into Undersea Applications*, Naval Postgraduate School Thesis of Monterey California, page 12

[6]Russ E. Davis, Charles C. Eriksen, Clayton P. Jones, 2002, *Autonomous Buoyancy-Driven Underwater Gliders*, Environmental Science, chapter 3, page 47, DOI: 10.1201/9780203522301

[7]William P.Barker, 2012, *An Analysis of Undersea Glider Architectures and an Assessment of Undersea Glider Integration Into Undersea Applications*, Naval Postgraduate School Thesis of Monterey California, page 10

[8]https://pdf.nauticexpo.com/pdf/kongsberg-maritime/seaglider/31233-105713.html

[9]https://www.alseamar-alcen.com/products/underwater-glider/seaexplorer

[10]https://en.wikipedia.org/wiki/Liberdade_class_underwater_glider

[11]https://auvac.org/100-2/

[12]https://www.graaltech.com/wp-content/uploads/2021/02/Data-Sheet_X-300-AUV-1.pdf

Chapter 2

Physical modeling of AUG motion

Chapter Symbology

$\mathbf{a}$	Generic acceleration
$\mathbf{e}_{321}$	Vector with the angular position on the inertial frame
$\mathbf{f}$	Generic force
g	Gravitational constant, equal to 9.81 m/s^2
m	Mass of the glider
m_x	Total moment acting on a body about axis x
m_y	Total moment acting on a body about axis y
m_z	Total moment acting on a body about axis z
p	Roll rate
q	Pitch rate
r	Yaw rate
$\mathbf{r}_{GQ}$	Distance vector between the center of gravity and a generic point Q
$\mathbf{v}$	Generic velocity
x	Longitudinal position on inertial/navigational reference frame
y	Lateral position on inertial/navigational reference frame
z	Vertical position on inertial/navigational reference frame
x/y	Subscript indicating the kinetic property of x on reference frame y
C_D	Drag coefficient
C_L	Lift coefficient
$\mathbf{G}$	Center of gravity of the glider
J	Generic inertia, to be defined with a proper subscript
L	Moment about the x axis of the glider
M	Moment about the y axis of the glider
N	Moment about the z axis of the glider
$\mathbf{P}$	Generic position of a body in a certain reference frame

$\mathbf{Q}$	Generic point of a body
$\mathbf{R}$	Generic rotational matrix
S	Generic surface
$\mathbf{S}_G$	Static moment tensor
U	Longitudinal velocity component in the wind frame
V	Lateral velocity component in the wind frame
W	Vertical velocity component in the wind frame
$, AM, Co$	Subscript standing for "Added mass, Coriolis"
$, BF$	Subscript standing for "Body and Fin"
D_{rag}	Drag force
$, HD$	Subscript standing for "Hydrodynamic"
$, HS$	Subscript standing for "Hydrostatic"
$, f$	Subscript standing for "fin"
$, h$	Subscript standing for "hull"
$, w$	Subscript standing for "wing"
L_{ift}	Lift force
V_{rel}	Relative velocity between the glider and the current
α	Angle of attack
β	Sideslip angle
δe	Elevator deflection
δr	Rudder deflection
φ	Roll angle
ϑ	Pitch angle
ψ	Bank angle
ρ	Water density
ω	Angular velocity, better defined by an appropriate subscript
$\bigtriangledown$	Volume of water displaced by the glider

2.1 Kinematics

Before the development of a dynamic model for the glider, it is necessary to set a number of reference systems which describe the kinematics of the glider. There are different types which can be more or less appropriate for the problem at hand. In general, three of them are the most used for aircraft modeling: the body frame, the inertial frame and the wind frame. The body frame (b_1, b_2, b_3) generally has its origin coincident with the center of gravity of the body in motion, but in this case, it will be more useful to use its center of buoyancy. The unit vector b_1 points towards the nose of the glider, b_2 is parallel to the right wing, which hypothetically has null dihedral and sweep angles, and b_3 is orthogonal to both, pointing towards

the bottom of the hull. An inertial frame (i_1, i_2, i_3) commonly used has an origin at the center of the Earth, a unit vector pointing towards the North pole and the other two at the Equator line. In this case, rather than an inertial frame, a navigational one will be used. A navigational reference system (n_1, n_2, n_3) has its origin on a prescribed point on the surface of the Earth, a unit vector pointing towards the center of the Earth, one towards the North Pole, and one towards the local East. Considering the navigational reference frame as an inertial one is more convenient for the purposes of this study and does not significantly affect the accelerations of the body. As a matter of fact, it is fairly straightforward to measure the effect of this simplification. One can develop the second derivative of the position of the body relative to the inertial frame, which in this case will be

$$\boldsymbol{P}_{B/I} = \boldsymbol{P}_{B/N} + \boldsymbol{P}_{N/I} \tag{2.1}$$

where $P_{B/N}$ is the position of the body in relation to the navigational frame and $P_{N/I}$ is the position of the navigational frame in relation to the inertial one. This will result in the following formula:

$$\boldsymbol{a}_{B/I} = \boldsymbol{a}_{N/I} + \boldsymbol{a}_{B/N} + \boldsymbol{\alpha}_{N/I} \times \boldsymbol{P}_{N/I} + 2\boldsymbol{\omega}_{N/I} \times \boldsymbol{v}_{B/N} + \boldsymbol{\omega}_{N/I} + \boldsymbol{\omega}_{N/I} \times \boldsymbol{P}_{N/B} \tag{2.2}$$

The angular acceleration of the navigational frame with respect to the inertial one can be considered null, while the angular velocity vector will be equal to $\Omega_E i_3$, the angular velocity of Earth's rotation. In addition, $\boldsymbol{a}_{N/I} = \boldsymbol{\omega}_{N/I} + \boldsymbol{\omega}_{N/I} \times \boldsymbol{P}_{N/I}$. Therefore, the difference between the body's acceleration in the inertial frame and in the navigational frame is:

$$\boldsymbol{a}_{B/I} - \boldsymbol{a}_{B/N} = 2\boldsymbol{\omega}_{N/I} \times \boldsymbol{v}_{B/N} + \boldsymbol{\omega}_{N/I} + \boldsymbol{\omega}_{N/I} \times (\boldsymbol{P}_{B/N} + \boldsymbol{P}_{N/I}) \tag{2.3}$$

$\boldsymbol{P}_{B/N}$ is negligible compared to $\boldsymbol{P}_{N/I}$, which is equal to the Earth's radius, 6371 km, $\boldsymbol{v}_{B/N}$ is approximately 0.5 m/s, and the Earth's rotation has an angular velocity of $7.2722 \times 10^{-5} rad/s$. Substituting these numbers brings to a difference in accelerations of 0.0034 g, which can be considered negligible. The different reference systems are shown graphically in figure 2.1.

In order to switch from inertial to body reference frame, three planar rotations must be done. The Euler angles describe the relation between the two systems and in the case of the glider they will be bank, pitch and heading angles, noted as $(\varphi, \vartheta, \psi)$. The first planar rotation is of an angle ψ about the i_3 unit vector. This will generate a new reference frame where i_1 and i_2 will change to a new orientation, i_1' and i_2'. At this point, a new rotation of ϑ degrees about the i_2' axis will be actuated. Finally, a rotation of an angle φ will occur about the $i_1'{}'$ axis, and the

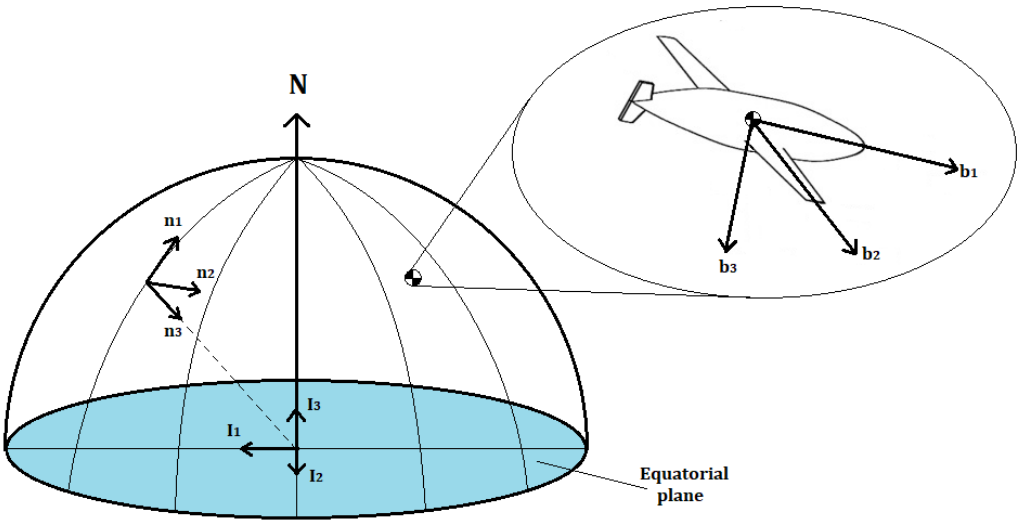

Figure 2.1: On the left are the navigational and inertial reference frames, respectively on a generic point of the surface of Earth and at its center. On the right the body frame is depicted, aligned with the glider.

final result will coincide with the glider's body reference frame. Each rotation can be mapped with its corresponding matrix.

$$\boldsymbol{R}_{\psi}^{T} = \begin{bmatrix} \cos\psi & \sin\psi & 0 \\ \sin\psi & \cos\psi & 0 \\ 0 & 0 & 1 \end{bmatrix} \tag{2.4}$$

$$\boldsymbol{R}_{\vartheta}^{T} = \begin{bmatrix} \cos\vartheta & 0 & -\sin\vartheta \\ 0 & 1 & 0 \\ \sin\vartheta & 1 & \cos\vartheta \end{bmatrix} \tag{2.5}$$

$$\boldsymbol{R}_{\varphi}^{T} = \begin{bmatrix} 1 & 0 & 0 \\ 0 & \cos\varphi & \sin\varphi \\ 0 & -\sin\varphi & \cos\varphi \end{bmatrix} \tag{2.6}$$

The matrix $\boldsymbol{R^T}$ that converts the inertial system into the body system will therefore be the matrix product between these three:

$$\boldsymbol{R}^{T} = \boldsymbol{R}_{\varphi}\boldsymbol{R}_{\vartheta}\boldsymbol{R}_{\psi} \tag{2.7}$$

and will have the following structure:

$$\boldsymbol{R}^T = \begin{bmatrix} \cos\psi\cos\vartheta & \sin\psi\cos\vartheta & -\sin\vartheta \\ -\sin\psi\cos\vartheta + \cos\psi\sin\vartheta\sin\varphi & \cos\psi\cos\vartheta + \sin\varphi\sin\vartheta\sin\psi & \cos\vartheta\sin\varphi \\ \sin\psi\sin\varphi + \cos\psi\sin\vartheta\cos\varphi & -\cos\psi\sin\varphi + \cos\varphi\sin\vartheta\sin\psi & \cos\vartheta\cos\varphi \end{bmatrix} \tag{2.8}$$

To pass from the body frame to the inertial frame, the matrix will be:

$$\boldsymbol{R} = \boldsymbol{R}_\psi \boldsymbol{R}_\vartheta \boldsymbol{R}_\varphi =$$

$$= \begin{bmatrix} \cos\psi\cos\vartheta & -\sin\psi\cos\vartheta + \cos\psi\sin\vartheta\sin\varphi & \sin\psi\sin\varphi + \cos\psi\sin\vartheta\cos\varphi \\ \sin\psi\cos\vartheta & \cos\psi\cos\vartheta + \sin\varphi\sin\vartheta\sin\psi & -\cos\psi\sin\varphi + \cos\varphi\sin\vartheta\sin\psi \\ -\sin\vartheta & \cos\vartheta\sin\varphi & \cos\vartheta\cos\varphi \end{bmatrix} \tag{2.9}$$

So one matrix is the transpose of the other.

Once the rotation matrix is defined, it is possible to write the first three kinematic equations, which relate the motion of the glider in the inertial/navigational frame to the one in the body frame. It is first necessary to define a few more parameters though. First of all, the state variables of the glider in the inertial frame will be defined as $(x, y, z, \varphi, \vartheta, \psi)$, which represent the spatial coordinates and the angles of the glider about the i_1, i_2 and i_3 axes of the inertial reference frame. In addition, one must define also the vector (U, V, W, p, q, r), which indicates the velocity components of the glider in its body axes and the angular velocities about them. The last three are more commonly known as roll, pitch and yaw rates. The standard is to name the subvector $(\varphi, \vartheta, \psi)$ as $\boldsymbol{e}_{321}$, while the subvector (p, q, r) will be referred to as $\boldsymbol{\omega}^B$. In this case the matrix relating them will be directly reported, without any derivation, for brevity and the sources will be available in the bibliography[1]. The relation between the two vectors will be

$$\dot{\boldsymbol{e}_{321}} = \boldsymbol{S}_{321}^{B-1} \boldsymbol{\omega}^B \tag{2.10}$$

where

$$\boldsymbol{S}_{321}^{B-1} = \begin{bmatrix} 1 & \tan\vartheta\sin\varphi & \tan\vartheta\cos\varphi \\ 0 & \cos\varphi & -\sin\varphi \\ 0 & \sec\vartheta\sin\varphi & \sec\vartheta\cos\varphi \end{bmatrix} \tag{2.11}$$

Of course the inverse will be

$$\boldsymbol{\omega}^B = \boldsymbol{S}_{321}^{B} \dot{\boldsymbol{e}_{321}} \tag{2.12}$$

where

$$\boldsymbol{S}_{321}^{B} = \begin{bmatrix} 1 & 0 & -\sin\vartheta \\ 0 & \cos\varphi & \cos\vartheta\sin\varphi \\ 0 & -\sin\varphi & \cos\vartheta\cos\varphi \end{bmatrix} \tag{2.13}$$

So at this point the six kinematic equations will be

$$(\dot{x},\dot{y},\dot{z})^{T} = \boldsymbol{R}\begin{bmatrix} U \\ V \\ W \end{bmatrix} \tag{2.14}$$

$$\dot{\boldsymbol{e}_{321}} = \boldsymbol{S}_{321}^{B-1}\boldsymbol{\omega}^{B} \tag{2.15}$$

These equations can be rendered explicit as:

$$\begin{aligned} \dot{x} = U(\cos\vartheta\cos\varphi) + V(-\sin\psi\cos\vartheta + \cos\psi\sin\vartheta\sin\varphi) + \\ + W(\sin\psi\sin\varphi + \cos\psi\sin\vartheta\cos\varphi) \end{aligned} \tag{2.16}$$

$$\dot{y} = U(\sin\psi\cos\vartheta) + V(\cos\psi\cos\vartheta + \sin\varphi\sin\vartheta\sin\psi) + W(\cos\varphi\sin\vartheta\sin\psi) \tag{2.17}$$

$$\dot{z} = U(-\sin\vartheta) + V(\cos\vartheta\sin\varphi) + W(\cos\vartheta\cos\varphi) \tag{2.18}$$

$$\dot{\varphi} = p + q(\tan\vartheta\sin\varphi) + r(\tan\vartheta\cos\varphi) \tag{2.19}$$

$$\dot{\vartheta} = q(\cos\varphi) + r(-\sin\varphi) \tag{2.20}$$

$$\dot{\psi} = q(\sec\vartheta\sin\varphi) + r(\sec\vartheta\cos\varphi) \tag{2.21}$$

2.2 Dynamic model

An additional reference system which was previously mentioned is the wind frame (w_1, w_2, w_3). This system is not useful to write the kinematic equations, but it will become necessary when dealing with aerodynamic forces and moments. Its origin also coincides with the buoyancy center of the glider, but the first unity vector w_1 is parallel to the relative wind speed, w_3 is on the glider's symmetry plane and w_2 is orthogonal to the other two. Two parameters which are defined by the wind reference frame are the angle of attack and the sideslip angle. The angle of attack is defined as $\alpha = V_{rel,1}/V_{rel3}$, and the sideslip angle is defined as sin $\beta = V_2/V$, where $V_{rel,1}$, $V_{rel,2}$ and $V_{rel,3}$ are the components of the current's velocity V_{rel} measured in the body frame. Figure 2.2 clarifies this graphically.

The attack and sideslip angles are also important to determine the rotation matrix which transforms the body frame into the wind frame. Starting from the body axes, a rotation of angle α must be made about the unit vector b_2, generating

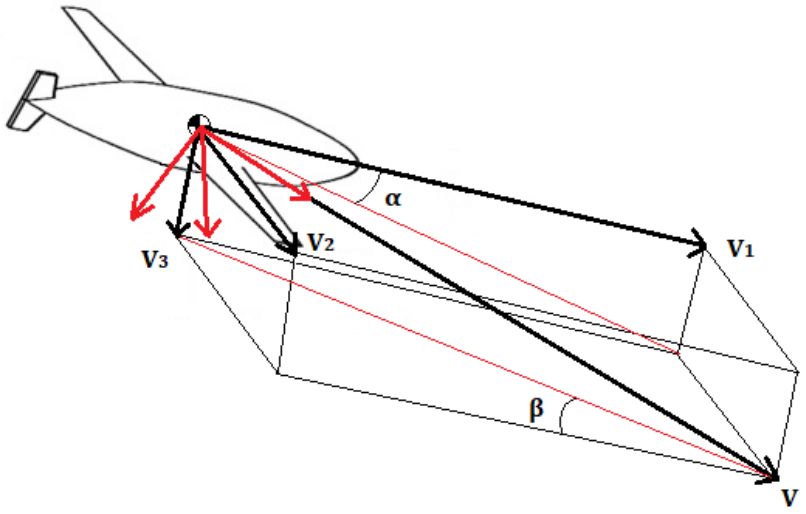

Figure 2.2: In black are the wind velocity components in the body reference frame, in red are the unit vectors, derivated by V and the angles α and β.

the triad (b'_1, b'_2, b'_3). The second and final rotation must occur about the unit vector b'_3 by an angle β. The consequent triad will coincide with that of the wind reference frame (w_1, w_2, w_3). So the rotation matrix will be

$$\boldsymbol{R}_W = \boldsymbol{R}_\beta \boldsymbol{R}_\alpha \tag{2.22}$$

with

$$\boldsymbol{R}_\alpha = \begin{bmatrix} \cos\alpha & 0 & \sin\alpha \\ 0 & 1 & 0 \\ -\sin\alpha & 0 & \cos\alpha \end{bmatrix} \tag{2.23}$$

$$\boldsymbol{R}_\beta = \begin{bmatrix} \cos\beta & \sin\beta & 0 \\ -\sin\beta & \cos\beta & 0 \\ 0 & 0 & 1 \end{bmatrix} \tag{2.24}$$

making the resulting matrix

$$\boldsymbol{R}_W = \begin{bmatrix} \cos\alpha\cos\beta & \sin\beta & \sin\alpha\cos\beta \\ -\cos\alpha\sin\beta & \cos\beta & -\sin\alpha\sin\beta \\ -\sin\alpha & 0 & \cos\alpha \end{bmatrix} \tag{2.25}$$

It is possible at this point to start deriving the dynamic equations that fully define the glider's model. Three equations are obtained from the translational equilibrium of the entire glider, meaning the condition in which the sum of all the forces acting on it is equal to zero, while the other three equations are derived from

rotational equilibrium, the condition in which the sum of all torques acting on the body is equal to zero. These forces and moments will be evaluated on and about each of the axes of the body reference frame. In this paragraph, the equations will not be derived and be given for granted, with just a summary description of the main terms.

Consider the center of gravity of the glider, G, coincident with the origin of the body center. The three translational equlibrium equations can be written as:

$$m\boldsymbol{I}\dot{\boldsymbol{v}}_{B/I} + \boldsymbol{S}_G^T\boldsymbol{\omega}_{B/I} + \boldsymbol{\omega}_{B/I} \times m\boldsymbol{I}\boldsymbol{v}_{B/I} = \boldsymbol{f} \tag{2.26}$$

In this case m is the total mass of the glider, so the integral over the whole volume of the glider $\int_V dm$, where dm is the infinitesimal mass of a single point of the body. $\boldsymbol{I}$ is the identity matrix, $\boldsymbol{v}_{G/I}$ is the velocity of the center of gravity, $\boldsymbol{S}_G^T$ is the transpose of the static moment tensor reduced to pole G, defined as $\int_V \boldsymbol{r}_{GQ} \times dm$, being $\boldsymbol{r}_{GQ}$ the distance vector between the points G and Q, where Q is a generic point of the body. In this case, since G coincides with the center of gravity of the glider, the static moment tensor will be equal to zero. Finally $\boldsymbol{\omega}_{B/I}$ is the angular velocity vector of the glider and $\boldsymbol{f}$ is the vector of the forces' components.

Regarding the rotational equilibrium equations, these can be written as:

$$\boldsymbol{S}_G\dot{\boldsymbol{v}}_{B/I} + \boldsymbol{J}_G\dot{\boldsymbol{\omega}}_{B/I} + \boldsymbol{v}_{G/I} \times (\boldsymbol{S}_G\boldsymbol{v}_{G/I} + \boldsymbol{J}_G\boldsymbol{\omega}_{B/I}) + \boldsymbol{\omega}_{B/I} \times (\boldsymbol{S}_G\boldsymbol{v}_{B/I} + \boldsymbol{J}_G\boldsymbol{\omega}_{B/I}) = \boldsymbol{m_G} \tag{2.27}$$

The two additional components to be described here are $\boldsymbol{J}_G$, which is the inertia tensor about the pole G and $\boldsymbol{m_G}$, which is the vector of the resultants of the torques acting on the glider about the pole G on each axis. The inertia tensor is defined as

$$\boldsymbol{J}_G = -\int_V \boldsymbol{r}_{GQ} \times \boldsymbol{r}_{GQ} \times dm \tag{2.28}$$

and its components would be noted as

$$\boldsymbol{J}_G = \begin{bmatrix} J_x & -J_{xy} & -J_{xz} \\ -J_{xy} & J_y & -J_{yz} \\ -J_{xz} & -J_{yz} & J_z \end{bmatrix} \tag{2.29}$$

But since the glider, as the vast majority of aircrafts, is symmetrical across its xz plane, the inertia tensor can be reduced to

$$\boldsymbol{J}_G = \begin{bmatrix} J_x & 0 & -J_{xz} \\ 0 & J_y & 0 \\ -J_{xz} & 0 & J_z \end{bmatrix} \tag{2.30}$$

Actually, in the case of many gliders, especially when they don't have a tail or where it is symmetric, there is symmetry even across the xy plane, making all the terms outside of the diagonal of $\boldsymbol{J}_G$ null. In the case of this project though, as it will be explained in later chapters, one of the aims is to design a glider that doesn't require symmetry on the xy plane, so this further simplification will not be applied.

Writing the equations explicitly, the following will be obtained:

$$m(\dot{U} + Wq - Vr) = f_x \tag{2.31}$$

$$m(\dot{V} + Ur - Wp) = f_y \tag{2.32}$$

$$m(\dot{W} + Vp - Uq) = f_z \tag{2.33}$$

$$J_x\dot{p} - J_{xz}(\dot{r} + pq) + (J_z - J_y)rq = m_x \tag{2.34}$$

$$J_y\dot{q} - J_{xz}(r^2 - p^2) + (J_x - J_z)pr = m_y \tag{2.35}$$

$$J_z\dot{r} - J_{xz}(\dot{p} - qr) + (J_y - J_x)pq = m_z \tag{2.36}$$

Although the equations are set and all the terms have been described, the next step is to better define the nature of the external forces and moments.

2.3 Forces and moments

In the following, the forces and moments acting on the glider will be analyzed. The main interest is in studying a steady gliding configuration, so any accelerations and angular velocities will be neglected. In more technical terms $\dot{U} = \dot{V} = \dot{W} = \dot{p} = \dot{q} = \dot{r} = p = q = r = 0$. This is a reasonable assumption during the normal functioning of the glider, since in general any manoeuvres are minimized during the gliding phases. The subdivision of these forces and moments will follow largely the model provided by Joo et al[2].

2.3.1 Longitudinal forces

The axial forces, corresponding to f_x, in the case of a glider will have the following components:

-**Hydrostatic**: this force is due to the combination of gravity and the buoyant force acting on the glider. It will be denoted as $f_{HS,x}$. Gravity is equal to the mass m of the glider times the gravitational constant g, and points downwards, towards the center of the Earth. The buoyant force is equal the weight of the volume of water displaced by the glider, but with opposite direction to the force of gravity.

So this component will be:

$$f_{HS,x} = g(\rho_w \bigtriangledown - m)\sin\vartheta \tag{2.37}$$

where ρ_w is the density of the water in which the glider operates and $\bigtriangledown$ is the volume of water displaced, equivalent to the volume of the glider. Of course the magnitude of such forces on the x axis will depend on the pitching angle of the glider. For a 90° angle the force will fully align with the longitudinal axis, while with a 0° angle the component vanishes.

-**Added mass and Coriolis**: these forces are all dependent on accelerations and angular velocities, so in this study they will be neglected. For the sake of completeness their formula is provided:

$$f_{AM,Co,x} = f_{x_{\dot{U}}}\dot{U} + f_{z_{\dot{W}}}wq + f_{z_{\dot{q}}}qq - f_{y_{\dot{V}}}Vr - f_{y_{\dot{r}}}rr \tag{2.38}$$

It should be noted that the notation $f_{x_{\dot{U}}}$ indicates the component of f_x which is directly proportional to $\dot{U}$.

-**Hydrodynamic**: These will be the main object of the studies in later chapters. Both lift and drag have a component on this axis. The general formulas for lift L and drag D are

$$L_{ift} = L_{ift,w} + L_{ift,h} + L_{ift,f} = \frac{1}{2}\rho_w V_{rel}^2(C_{L,w}S_w + C_{L,h}S_h + C_{L,f}S_f) \tag{2.39}$$

$$D_{rag} = D_{rag,w} + D_{rag,h} + D_{rag,f} = \frac{1}{2}\rho_w V_{rel}^2(C_{D,w}S_w + C_{D,h}S_h + C_{D,f}S_f) \tag{2.40}$$

The direction of lift is perpendicular to that of the relative wind, while the direction of drag is parallel to that of the relative wind. Therefore

$$\begin{aligned} f_{HD,x} = \frac{1}{2}\rho_w V_{rel}^2[&(C_{L,w}S_w + C_{L,h}S_h + C_{L,f}S_f)\sin\alpha + \\ &- (C_{D,w}S_w + C_{D,h}S_h + C_{D,f}S_f)\cos\alpha] \end{aligned} \tag{2.41}$$

A more compact but also more implicit way to write these components is:

$$f_{HD,x} = f_{x_{U|U|}}U|U| \tag{2.42}$$

-**Thrust**: The thrusting force is not provided by a propeller and the buoyancy engine does not generate an active force during the gliding phase (its action is taken into account by the buoyant force), so this force is effectively null for most gliders, with the rare exception of those equipped with an auxiliary propulsion system.

2.3.2 Lateral forces

The sum of the lateral forces, indicated with f_y, for a steady gliding path will generally be null, but it is important to be aware of them for the purpose of control. They are constituted by the following components.

-**Hydrostatic**: Similar to the axial case, but with opposite sign and dependent on the bank angle

$$f_{HS,y} = g(m - \rho_w \bigtriangledown) \cos\vartheta \sin\varphi \tag{2.43}$$

-**Added mass and Coriolis**: As in the case of the axial components, these will be neglected for the purposes of this study, but the general formula will be reported

$$f_{AM,Co,y} = f_{y_{\dot{V}}}\dot{V} + f_{y_{\dot{r}}}\dot{r} + f_{x_{\dot{U}}}Ur - f_{z_{\dot{W}}}Wp - f_{z_{\dot{q}}}pq \tag{2.44}$$

-**Crossflow drag**: In the presence of a sideslip angle there will also be crossflow hydrodynamic components. The aerodynamic coefficients in this case will be different from the conventional ones of lift and drag. So for now the components will be written as

$$f_{HD,y} = f_{y_{V|V|}}V|V| + f_{y_{r|r|}}r|r| \tag{2.45}$$

-**Body and fin lift**: These occur with sideslip or with a non-null yawing velocity and can be written as:

$$f_{BF,y} = f_{y_{UV,B}}UV + f_{y_{UV,F}}UV + f_{y_{Ur,F}}Ur + f_{y_{UU\delta r,F}}\delta r U^2 \tag{2.46}$$

In this case δr is the deflection of the rudder, if one is present.

2.3.3 Vertical forces

Just as the longitudinal forces, these will be critical towards understanding the typical gliding motion of the glider. Its components can also be classified similarly to the longitudinal forces:

-**Hydrostatic**: Just as in the other cases, the two main agents of the hydrostatic forces are gravity and buoyancy, with the obvious trigonometric differences. In the vertical axis the components will be:

$$f_{HS,z} = g(m - \rho_w \bigtriangledown) \cos\vartheta \cos\varphi \tag{2.47}$$

-**Added mass and Coriolis**: Once again, despite them not being taken into consideration for now, these components will be listed anyways for the sake of

completeness.

$$f_{AM,Co,z} = f_{z_{\dot{W}}}\dot{W} + f_{z_{\dot{q}}}\dot{q} + f_{x_{\dot{U}}}Uq - f_{y_{\dot{V}}}Vp - f_{y_{\dot{r}}}rp \tag{2.48}$$

-**Hydrodynamic**:The same forces of lift and drag previously seen among the longitudinal components are present here. The only difference here will be in trigonometrical nature.

$$\begin{aligned} f_{HD,z} = \frac{1}{2}\rho_w V_{rel}^2[&(C_{L,w}S_w + C_{L,h}S_h + C_{L,f}S_f)\cos\alpha + \\ &- (C_{D,w}S_w + C_{D,h}S_h + C_{D,f}S_f)\sin\alpha] \end{aligned} \tag{2.49}$$

As in the longitudinal case, the more compact form can be written as:

$$f_{HD,z} = f_{z_{W|W|}}W|W| + f_{z_{q|q|}}q|q| + f_{z_{UW,B}}UW + f_{z_{UW,F}}UW + f_{z_{Uq,F}}Uq + f_{z_{UU\delta e,F}}\delta eU^2 \tag{2.50}$$

where δe is the deflection of the elevator, if one is present.

2.3.4 Rolling moment

The rolling moment is the one that causes a change in the angular velocity p about the longitudinal body axis. These are generally caused by the same forces listed above, so they can be classified using the same subcategories:

-**Hydrostatic**: If the origin of the body system coincides with the gravity center, then the mass will have no effect on the hydrostatic moment. Therefore its rolling component will be:

$$L_{HS} = \rho_w \bigtriangledown g(y_G\cos\vartheta\cos\varphi - z_G\cos\vartheta\sin\varphi) \tag{2.51}$$

where y_G and z_G are the y and z coordinates of the gravity center in the body reference frame.

-**Added mass and Coriolis**: As usual this will be ignored, but it will be listed nonetheless:

$$L_{AM,Co} = L_{\dot{p}}\dot{p} \tag{2.52}$$

-**Rolling drag**: The drag force caused by the rolling motion will generate a rolling moment opposite to the roll direction.

$$L_{RD} = L_{p|p|}p|p| \tag{2.53}$$

-**Propeller**: The absence of a proper propelling system makes this component null.

2.3.5 Pitching moment

Unfortunately the pitching moment components have a longer list, but with the proper simplifications most of them will be negligible.

-**Hydrostatic**: This is similar to the rolling moment, but the longitudinal coordinate of the gravity center will play a role instead of the lateral one.

$$M_{HS} = -\rho_w \bigtriangledown g(x_G \cos\vartheta \cos\varphi + z_G \sin\vartheta) \tag{2.54}$$

-**Added mass and Coriolis**: This in particular is the scary looking part, but that fortunately will be negligible for most intents and purposes:

$$M_{AM,Co} = M_{\dot{W}}\dot{W} + M_{\dot{q}}\dot{q} + (f_{x_{\dot{U}}} - f_{z_{\dot{W}}})UW - f_{y_{\dot{r}}}Vp + (L_{\dot{p}} - N_{\dot{r}})rp - f_{z_{\dot{q}}}Uq \tag{2.55}$$

-**Hydrodynamic**: These include moments generated by crossflow drag and lift from body and fin:

$$M_{HD} = M_{W|W|}W|W| + M_{q|q|}q|q| + M_{UW,B}UW + M_{UU\delta e}U^2\delta e + M_{UW,F}UW + M_{Uq,F}Uq \tag{2.56}$$

2.3.6 Yawing moment

Similarly to the pitching moment, even here there are many components, but most of them can be considered negligible.

-**Hydrostatic**: The key coordinates here will be x_G and y_G, but the nature of the moment will remain similar to the other cases.

$$N_{HS} = \rho_w \bigtriangledown g(x_G \cos\vartheta \sin\varphi + y_G \sin\vartheta) \tag{2.57}$$

-**Added mass and Coriolis**: Once again, this is where most of the superfluous components are:

$$N_{AM,Co} = N_{\dot{V}}\dot{V} + N_{\dot{r}}\dot{r} + (f_{y_{\dot{V}}} - f_{x_{\dot{U}}})UV + f_{z_{\dot{q}}}Wp - (L_{\dot{p}} - M_{\dot{q}})pq + f_{y_{\dot{r}}}Ur \tag{2.58}$$

-**Hydrodynamic**: Same as the pitching moment, these include moments generated by crossflow drag and lift from body and fin:

$$N_{HD} = N_{V|V|}V|V| + N_{r|r|}r|r| + N_{UV,B}UV + N_{UU\delta r}U^2\delta r + N_{UV,F}UV + N_{Ur,F}Ur \tag{2.59}$$

2.4 Steady longitudinal gliding dynamics

When dealing with steady longitudinal dynamics, the main interest for the initial design of an AUG, an assortment of assumptions can be made which will simplify the dynamic equations and allow to understand which are the main aspects to focus on for the modeling of the glider.

The first assumption to make is that the glider is at a trim condition, so no accelerations, translational or rotational, are occurring. Specifically, the trim condition is that of steady climbing or steady descending flight, although in this case the two are conceptually the same thing. This means that $\dot{U} = \dot{V} = \dot{W} = 0$, $\dot{p} = \dot{q} = \dot{r} = 0$, but also that $p = q = r = 0$. In addition, while the heading and pitch angles in the inertial frame can be different from zero, the symmetry of the glider along the xz plane means that the bank angle must be null, so $\varphi = 0$. This type of trim does not exclude the presence of a sideslip angle, since there could be currents, so V doesn't necessarily have to be excluded, but for now the waters will be considered calm. Another assumption to make is that the rudder and elevator, if even present in the first place, will not be deflected, so $\delta e = \delta r = 0$. Once these premises are made, the dynamic equations not only simplify considerably, but also are not as strongly coupled anymore. It is possible to distinguish the longitudinal dynamics from the latero-directional dynamics by isolating the longitudinal and vertical translation equilibrium equations along with the pitching moment equilibrium equation. Respectively, these will have the following form:

$$\begin{aligned}\sum f_x = {} & g(\rho_w \bigtriangledown - m)\sin\vartheta + \\ & + \frac{1}{2}\rho_w V_{rel}^2[-(C_{L,w}S_w + C_{L,h}S_h + C_{L,f}S_f)\sin\alpha + \\ & + (C_{D,w}S_w + C_{D,h}S_h + C_{D,f}S_f)\cos\alpha] = 0\end{aligned} \tag{2.60}$$

$$\begin{aligned}\sum f_z = {} & g(\rho_w \bigtriangledown - m)\cos\vartheta\cos\varphi + \\ & + \frac{1}{2}\rho_w V_{rel}^2[(C_{L,w}S_w + C_{L,h}S_h + C_{L,f}S_f)\cos\alpha + \\ & + (C_{D,w}S_w + C_{D,h}S_h + C_{D,f}S_f)\sin\alpha] = 0\end{aligned} \tag{2.61}$$

$$\begin{aligned}\sum m_y = {} & -\rho_w \bigtriangledown g(x_G\cos\vartheta\cos\varphi + z_G\sin\vartheta) + M_{W|W|}W|W| + M_{UW}UW = \\ & = 0\end{aligned} \tag{2.62}$$

where $M_{UW} = M_{UW,B} + M_{UW,F}$.

To lighten the equations, the following is posed:

$$C_L S_{ref} = C_{L,w}S_w + C_{L,h}S_h + C_{L,f}S_f \tag{2.63}$$

$$C_D S_{ref} = C_{D,w} S_w + C_{D,h} S_h + C_{D,f} S_f \tag{2.64}$$

By rewriting equations (2.60) and (2.61) in the body reference frame rotated by ϑ, the following are obtained:

$$0 = \frac{1}{2}\rho_w V_{rel}^2 S_{ref}[-(C_L \sin(\alpha+\vartheta) + (C_D \cos(\alpha+\vartheta)] \tag{2.65}$$

$$g(\rho_w \bigtriangledown - m) + \frac{1}{2}\rho_w V_{rel}^2 S_{ref}[(C_L \cos(\alpha+\vartheta) + (C_D \sin(\alpha+\vartheta)] = 0 \tag{2.66}$$

Simplifying and manipulating equation (2.65) leads to:

$$\frac{C_D}{C_L} = \tan(\alpha+\vartheta) \tag{2.67}$$

This is a notable and quite convenient result once it is noticed that in the inertial reference frame the following kinematic equation holds, as can be deduced from figure 2.3:

$$\frac{\dot{z}}{\dot{x}} = \tan(\alpha+\vartheta) \tag{2.68}$$

Therefore the overall aerodynamic efficiency of the glider is equal to its glide ratio.

Through further manipulations of the translational equilibrium equations, specifically by dividing (2.60) by (2.61), it is possible to attain the following relation which, for a specific aerodynamic configuration, ties the pitch angle to the angle of attack:

$$\tan\vartheta = \frac{C_L \sin\alpha - C_D \cos\alpha}{C_D \sin\alpha - C_L \cos\alpha} \tag{2.69}$$

In addition, remembering the basic trigonometric relation $\sin^2\vartheta + \cos^2\vartheta = 1$, the equations (2.60) and (2.61) can be squared, summed and then elevated again by 0.5 to obtain the following equation, which ties the mass of the glider to its velocity modulus:

$$g(\rho_w \bigtriangledown - m) = \frac{1}{2}\rho_w V_{rel}^2 S_{ref} \sqrt{C_L^2(\alpha) + C_D^2(\alpha)} \tag{2.70}$$

Which can be useful for the sizing of the glider and in particular of the buoyant mass.

Finally, by using the pitch rotational equilibrium equation, the following relation can be obtained, which reveals the x coordinate of the gravity center as a function of the pitch angle:

$$x_G = \frac{(M_{W|W|}\alpha|\alpha| + M_{UW}\alpha)V_{rel}^2 - \rho_w \bigtriangledown g z_G \sin\vartheta}{\rho_w \bigtriangledown g \cos\vartheta} \tag{2.71}$$

Although these results will become necessary for the design of the glider, they also show that the aerodynamic qualities will also affect the relations considerably. So before putting these equations to use, the first step should be the design and optimization of the hydrodynamic surfaces, mainly hull and wings.

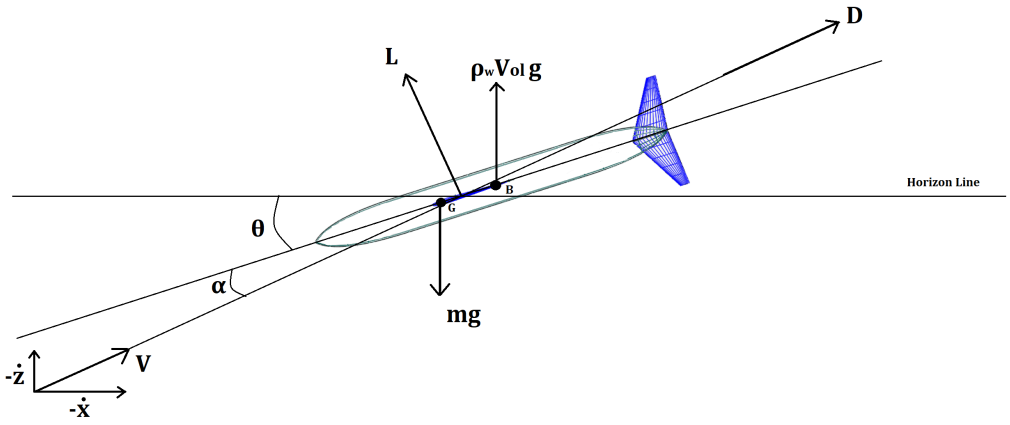

Figure 2.3: Representation of the forces acting on an AUG during its steady descending glide.

Chapter Bibliography

[1]Bandu N. Pamadi, 1998, *Performance, Stability, Dynamics and Control of Airplanes*, American Institute of Aeronautics and Astronautics, Chapter 3

[2]Moon G. Joo,Zhihua Qu, 2015, *An Autonomous Underwater Vehicle as an Underwater Glider and Its Depth Control*, International Journal of Control, Automation, and Systems, pages 1213-1214, DOI 10.1007/s12555-014-0252-8

Chapter 3

Hull Design

The first component of the AUG to be dealt with will be the hull. This is because the design of the wings is heavily dependent on the shape, size and mass distribution of the hull (or fuselages in a broader sense). Even if the lift contribution of the hull is negligible at best, the minimization of its drag is a crucial aspect of the design, since generally it will be of a similar magnitude as that of the wings. In the following paragraphs, the procedure to achieve an optimal design will be described.

Chapter Symbology

a	Length of the nose of the hull
b	Length of the midbody of the hull
c	Length of the tail of the hull
d	Maximum diameter
e	Energy
i, j	Subscripts indicating the generic component of a vector
l	Characteristic length
m	Mass of the glider
n	Nose shape parameter
$\dot{q}$	Heat flux
p	Local pressure
r	Local radius
u	Local flow velocity
x	Longitudinal coordinate of the glider's length, zero at the nose tip
$form$	Subscript: effect related to the normal pressure
$fric$	Subscript: effect related to shear stresses
ind	Subscript: effect related to lift generation

$interf$	Subscript: effect related to interference between different parts
$wave$	Subscript: effect related to transonic and supersonic velocities
C_D	Drag coefficient
C^p	Prismatic coefficient
D_{rag}	Drag force
L/D	Fineness ratio
L	Total length of the hull
M_∞	Free-stream Mach number
S_{ref}	Reference surface
Re	Reynolds number
U	Free-stream velocity
δ	Local boundary layer thickness
δ^1	Local boundary layer displacement thickness
δ^2	Local boundary layer momentum thickness
ν	Kinematic viscosity of the fluid
ϑ	Tail shape parameter
ρ_w	Water density
τ	Local shear stress
$\bigtriangledown$	Total volume of the glider
Φ	Flow potential

3.1 Hydrodynamics concepts

In this chapter the dynamic concept best examined will be that of drag, or hydrodynamic resistance, since lift and pitching moment tend to be irrelevant in the design of an AUG's hull. Drag is the force acting on a body in motion through a fluid with a direction parallel to the relative velocity between the body and the fluid, or the flow velocity. In the case of vehicle design, the objective is that of drag minimization, as it is for most purposes detrimental to the performances and efficiency of an aero/hydrodynamic system. To understand how to do so, it is necessary to describe the various components of drag and the physical principles upon which they act.

-Parasitic drag will be the main drag component examined for the design process of the hull, and can be divided in two components: form drag and friction drag. **Form drag** is due to the pressure differences on the surface of a body, which causes boundary layer separation and the formation of wake. The magnitude of such effects is dependent on the shape of the body, hence the naming of this category. **Friction drag** instead is due to the shear stresses acting on the surface of the body, due to the fluid's viscosity. This type of drag is mostly dependent on the

Reynolds number, which will soon be described in more detail, but partially also on the body's geometry.

-Induced drag is caused by the generation of lift force of an aero/hydrodynamic body. The physical explanation of it is that lift is generated by a pressure difference between the lower and upper surfaces. Therefore the fluid particles will tend to move from the higher pressure regions to the lower pressure ones, causing vortices at the wingtips, which will generate drag. In the case of the hull, induced drag will be negligible, since it produces nearly no lift, but it will become more relevant when dealing with the design of the wings.

-Wave drag, when present, is caused by the presence of shock waves, and increases dramatically the overall hydrodynamic resistance once a critical Mach number is reached. Such number is dependent on the shape of the body, but is generally larger than 0.3. Such glide conditions will never be reached by the AUG, and no propellers are present, so wave drag is not going to be a concern in the design of any unpropelled hydrodynamic component.

Another type which is more common among marine vehicles is the wave-making resistance. When a body moves on a water surface or slightly below it, waves at the nose and the wake are produced and their interaction causes an additional drag component, which is going to be affected by the Froude number, also known as the speed-length ratio. For AUGs, the Froude number is generally small enough to render this drag component negligible, and additionally the glider is only going to spend very limited amounts of time near the water surface, so even wave-making drag will be neglected.

-Interference drag is the most ambiguous type of resistance and is particularly difficult to predict. It is a generic term which indicates a number of effects that arise when multiple bodies are invested by the same flow. The consequence is that the sum of each component's drag is different from the actual drag of the whole system. Such difference corresponds with the interference drag.

So overall, the total drag is the sum of these components:

$$D_{rag} = D_{form} + D_{fric} + D_{ind} + D_{wave} + D_{interf} \tag{3.1}$$

but it can be summarized as a function of the characteristics of the free-stream multiplied by a coefficient dependent on the flow's properties and on the body's geometry, as seen in the previous chapter:

$$D_{rag} = \frac{1}{2}\,\rho\,U^2\,S_{ref}\,C_D \tag{3.2}$$

The next concept that needs to be highlighted is that of **boundary layer**. The

boundary layer is a part of the flow adjacent to the body which is slowed down compared to the free-stream due to the effects of viscosity, which imposes a no-slip condition on the surface of the body. The nature of the boundary layer has deep ties to the overall drag force acting on a body, of both form and friction type. In general it can be distinguished into two types:

-Laminar boundary layer: In this case the streamlines surrounding the body are nearly parallel. The flow surrounding the body is orderly and smooth. In general this type of boundary layer will lower the skin friction drag, but unfortunately it is also a lot less stable than the turbulent counterpart. This instability makes it usually inconvenient to attempt to have a laminar flow over a lifting surface such as a wing, but it can be favorable in the case of a hull or a fuselage, where skin friction is the most significant component of aero/hydrodynamic resistance.

-Turbulent Boundary layer: Opposed to the laminar boundary layer, the turbulent one is more disordered, with the formation of swirls, or "eddies". In general, every boundary layer starts off as laminar, only to devolve into a turbulent flow. The way in which this transition occurs is dependent on the shape of the body and on the so called Reynolds number. Below is a picture that illustrates the differences between laminar and turbulent flow and the transition between them on a flat plate, where U is the free-stream velocity, u is the local velocity and δ is the boundary layer thickness, defined as the region in which the ratio between the local velocity and the free-stream velocity is lower than 0.99.

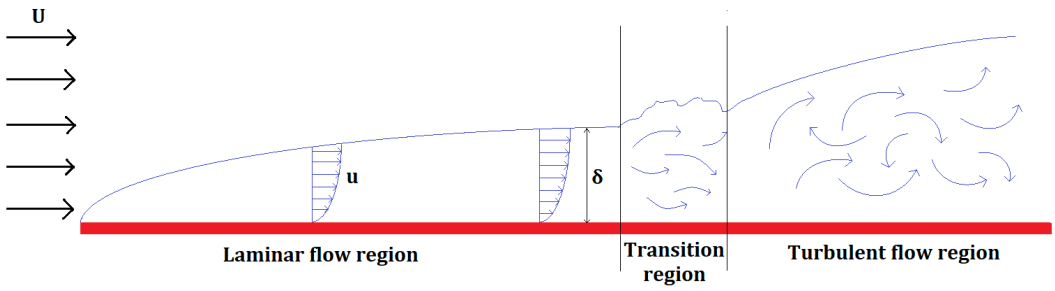

Figure 3.1: Development of a boundary layer over a flat plate.

The **Reynolds number** is an adimensional number that is used to determine the nature of the flow. Its basic formula is the following:

$$Re = \frac{l\,U}{\nu} = \frac{\rho\,l\,U}{\mu} \tag{3.3}$$

where ρ, U, ν and μ are respectively the density, the velocity and the kinematic and dynamic viscosity of the free-stream, while l is the characteristic length of the body, appropriately chosen based on its shape. Conceptually speaking, this number can be described as the ratio between viscous forces and inertial forces acting within

the fluid.

The Reynolds number's main use is for the prediction of the development of the boundary layer, which allows to make estimates on the overall aerodynamic forces to which the body invested by the flow is subjected. Through its knowledge, it is possible to determine the thickness and skin friction coefficient of a boundary layer for both laminar and turbulent flows.

Lastly, a fundamental concept, which will have significance for both the hull design and the wing design, is that of **pressure gradient**. This is the variation of the pressure along the surface of a body. In the case of a flat plate parallel to the flow, the gradient is equal to zero, but in the case of a curved surface it will behave as shown in the figure below. A so called favourable pressure gradient, in which $dP/dx < 0$, will flatten the velocity distribution, delaying separation and making the boundary layer more stable, while an adverse pressure gradient, in which $dP/dx > 0$, will do the opposite. The point in which the velocity distribution takes the shape of a cuspid is the point at which the separation occurs. Separation of the boundary layer has dramatic effects on the drag and lift of a body and should normally be delayed as much as possible.

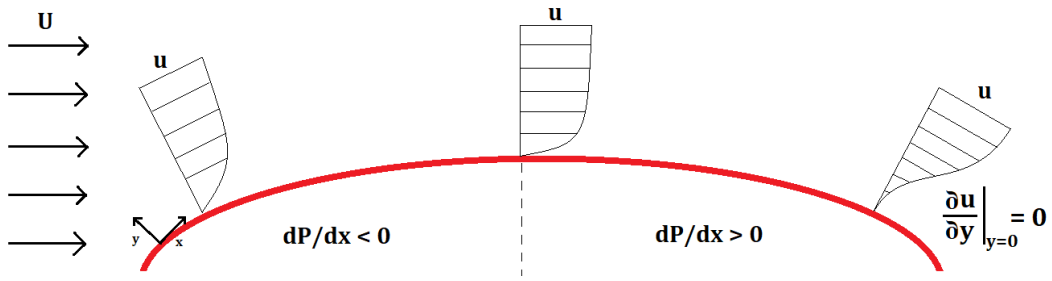

Figure 3.2: Development of a boundary layer over a curved surface.

3.2 Preliminary design parameters

While conventional aircraft fuselage design techniques are fairly easy to come across, the same can't be said about submarines, since these are generally employed for military purposes and therefore technical data is often not accessible to the public. Nonetheless, some information on the fundamental parameters is still available, and many of the concepts that are applied to aircraft fuselages for drag minimization can also be applied to a submarine's hull. Below are reported some of the characteristic parameters and their effect on the overall hydrodynamic performances, namely drag.

-The first fundamental parameter is the **fineness ratio L/D**, which is the ratio between length and maximum diameter of the hull. A higher fineness ratio will

increase the surface to volume ratio of the body, meaning that for a fixed volume there will be a larger wetted area and therefore a larger skin-friction component of drag. At the same time though, a higher fineness ratio will decrease the form drag component, since the body will be more slender, avoiding large adverse pressure gradients and delaying separation of the boundary layer. Therefore there must be an optimal value which minimizes the total drag. Such values are generally in the range of $6 < L/D < 7$ for conventional submarines[1], depending on the Reynolds number. It must be noted that most aircraft and submarines are unable to have such ratios, mainly for practical reasons related to their missions, but often even a fineness ratio of around 9 is deemed acceptable.

-The next fundamental parameter is the **prismatic coefficient C^p**, which is the ratio between the total volume of the hull and that of a cylinder with length and diameter equal to the length and maximum diameter of the body. This ratio will mostly influence the form resistance. For a C^p that tends to 1, the body will have a shape more similar to that of a cylinder, with a high nose and tail radius, but with a decreasing C^p there will be gradually steeper gradients, increasing the risks of flow separation. Once again, there will be an optimal value, which generally stands at about 0.60-0.61. It must be noted that it isn't sufficient to just set that value. For two hulls with equal C^p, if one has the section with maximum diameter close to the nose and one has it close to the tail, there can be considerable differences in the total resistance between the two of them. Arentzen and Mandel[2] have compiled a list with ideal parameters of each C^p. In this case, C^p_{noMB} is the prismatic coefficient of the hull without the midbody, while L_{MB} is the length of the midbody. The midbody is defined as the part of the hull where there the diameter is equal to its maximum value D and remains constant.

C^p	$C^p, noMB$	b
0.600	0.600	0.000
0.640	0.612	0.068
0.680	0.625	0.143
0.700	0.632	0.185
0.720	0.638	0.225
0.760	0.652	0.311
0.800	0.667	0.400
0.840	0.682	0.495
0.880	0.700	0.600

Table 3.2: Optimal midbody parameters as a function of C^p.

-Other significant parameters which are taken into consideration when designing a hull are the **nose and tail radii** and the **maximum cross-section location**.

Although these parameters will have an active role in the design of the hull, for now the standards for the most common vehicles will be ignored for a few reasons. First of all, most airplanes and submarines do not attempt to have a laminar flow over the fuselage or the hull, which conditions significantly the optimal position of the midbody. In fact, the maximum cross-section location will usually be set at $x = 0.32 \div 0.40L$ for conventional aircraft, but if it is desired for the laminar flow to cover an extensive portion of the body, then the midbody will have to be located much further towards the aft. In addition, the design of the tail for submarines takes into account the presence of propellers, which are absent in AUGs. Lastly, it is still up for debate how much of a difference the nose radius really makes to overall drag, so most submarines will give priority to the more practical aspects, such as the maximization of the total volume, rather than hydrodynamic ones.

To define the hull's geometry, a method which references the studies by Myring will be used, in which the hull is divided in three parts: forebody, midbody and aftbody. While the midbody will have a constant radius, the forebody and midbody will be parametrized with specific curves. This method will be described with more detail in the "Geometry definition" paragraph.

3.3 Constraints

Unfortunately, while many of the inconveniences present in most aircraft and submarines will be absent, the design of the AUG's hull will still have to abide to a set of constraints, which may hinder the optimization efforts.

-The first significant constraint is the total volume of the envelope. Since the volume is proportional to the total wetted surface and therefore to the total drag, ideally it should be as small as possible. The lower bound can generally be set through the knowledge of the total mass of the glider, since it will have to be balanced by the buoyancy force, which is exactly proportional to the total volume. From the vertical translational equilibrium equation, one will have

$$\bigtriangledown \simeq \frac{m}{\rho_w} \tag{3.4}$$

since the hydrodynamic forces will be much smaller. This is because they are proportional to the variable mass of the glider and, as seen in the state of the art chapter, the ratio between total and variable mass is in the range of 50-80 for commercial gliders. Still from the state of the art, one can see that the empty weight of a glider ranges between 50-60 kg, with an additional payload. For now a total mass of 60 kg will be estimated and from this, the minimum volume of the glider will have to be $0.06\,m^3$. Although not absolutely precise, this is a very

reasonable estimate to start with.

-Another crucial constraint comes from longitudinal stability requirements. In conventional flight dynamics, it is of paramount importance that the center of gravity stays ahead of the aerodynamic center. In the case of an AUG, the lift force is not very large, but the buoyancy force will be nearly equal to the gravity acting on the glider. Since they have opposite directions, a considerable moment could be generated, which the load on the wings is generally not going to be able to balance. So it is important for the center of gravity and the buoyancy center to be close to each other, with an additional disalignment on the vertical body axis to provide more stability.

-During the design it must be ensured that the hull is also structurally sound. In general, this is done by the inner pressure hull, which has to withstand the pressure difference between the inside of the AUG and the outside pressure, which can reach up to 10 MPa at a depth of 1000 m. While these pressures are high enough to crush humans or any payload of the glider, from a metallurgical standpoint they are not very large loads. For conventional submarines, the large size makes it so that a significant bending moment can develop towards the center of the hull, but for AUGs, which generally have a maximum length of 2 meters, even the bending moment does not require excessively sturdy structures to withstand it. Most of the commercial AUGs have aluminum pressure hulls. Alternatively, like in the case of the SeaGlider, it may be made of carbon fiber, taking up less space and weight, but with an additional cost on the manufacturing.

-This is not necessarily a constraint in most hulls and fuselages, but specifically in this project it will be attempted to obtain a laminar flow over a vast portion of the vehicle. As previously mentioned, the boundary layer undergoes transition and separation much faster in the presence of an adverse pressure gradient, so in order to maintain a laminar flow, the nose will have to take a considerable portion of the hull's length, since in this area

$$\frac{dr}{dx} > 0 \tag{3.5}$$

where r is the local radius, and therefore

$$\frac{dp}{dx} < 0 \tag{3.6}$$

It must also be noted that laminar flows over the hull are not very common, partly because of the larger dimensions of most submarines and aircraft, but also because of the numerous difficulties related to such flows. For some time it was believed that laminar hulls would be the next frontier of submarine design, but ultimately this idea was discarded because a laminar flow could be disrupted even

just by water impurities. This can suggest that the glider's wings will have to be positioned towards the aft of the body, where the flow has already transitioned, in order to impact as little as possible its laminar qualities.

There are additional geometrical constraints in the design of the glider that will be taken into consideration, but they are related more to the specific design methods, so it is better to list them in the next paragraph.

3.4 Geometry definition

Due to the purposes of most submarines, most data regarding their design and performances is classified. The following processes are based on NASA reports on the minimization of drag on blunt bodies[3] and on the previously cited report by Volker Bertram, which compiles some of the most crucial aspects of submarine design.

First of all, since AUGs lack of some of the constraints that many commercial fuselages have, the hull can be a perfect body of revolution, a solid obtained by rotating a curve about a straight axis, which in this case will be the longitudinal axis of the AUG. The hull is divided in three sections: nose, or forebody, midbody, and the tail, or aftbody. Along the nose, the hull's diameter monotonically increases until it reaches its maximum, which will be indicated as the nominal diameter and will mark the beginning of the midbody. Along the midbody the diameter remains constant until the tail is reached, and there it gradually shrinks. The curves that define the radius distribution of the nose and the tail are respectively defined with the following functions:

$$r(x) = \frac{1}{2}d\left[1 - \left(\frac{x-a}{a}\right)^2\right]^{\frac{1}{n}} \tag{3.7}$$

$$r(x) = \frac{1}{2}d - \left(\frac{3d}{2c^2} - \frac{tan\vartheta}{c}\right)(x-a-b)^2 + \left(\frac{d}{c^3} - \frac{tan\vartheta}{c^2}\right)(x-a-b)^3 \tag{3.8}$$

where a, b and c are the lengths of the nose, midbody and tail, n is a parameter which defines the nose shape (the higher it is the more the curve will be convex), ϑ is the semi-angle of the tail's trailing edge, and d is the nominal diameter. The nose will have a semi-elliptical radius distribution, while the tail will be defined by a third degree polynomial. So for a given length of the hull, the geometry is completely defined by 6 parameters, which are graphically represented in figure [3.3]. This method has been described thoroughly by Myring[4].

A method needs to be devised to define the values of these parameters in order

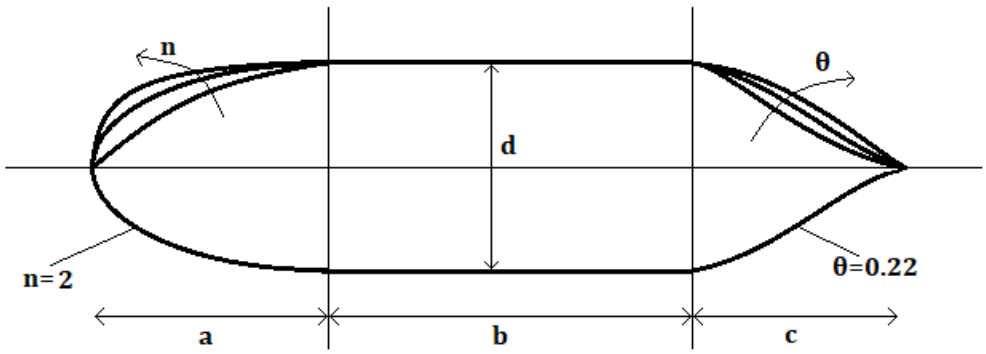

Figure 3.3: Effect of the six parameters on the geometry of a generic hull.

to obtain a functional design. A possibility could be to pose a few constraints on some of the design parameters which were previously mentioned, such as the prismatic coefficient and the consequent ideal length of the midbody, the fineness ratio, and the total volume of the hull. These boundaries are still less than the free parameters, so there can be multiple solutions that satisfy them. It is also useful, especially when programming a design system, to define some lower and upper boundaries to parameters such as n and ϑ. Usually, these last two do not have significant effects on the total drag developed by the glider, as long as they stay in their respective ranges of $0.5 - 3$ and $0 - 40°$. Things change though when longer noses and tails are considered, so the values of n will be restricted between $1.5 - 2.3$, in order to maintain some structural stability without hindering the laminar boundary layer.

The next step is to select a range for the parameters which will be optimized, in this case fr, and a. According to Volker Bertram, conventional submarines have an optimum fineness ratio that ranges between $6 - 7$, depending on the Reynolds number at which the vehicle operates. It must be underlined though that the submarines he refers to have Reynolds numbers which can be up to two orders of magnitude higher than those of commerical AUGs, and also they do not aim to attain laminar flow, so in this case, a wider range of fr will be considered, spanning from 6 to 9. He also recommends the nose to be equal approximately to 37% of the entire hull length, but for the same considerations made for the fineness ratio, the parameter a's range of values to be examined was extended to be $30 - 70\%$ of the entire hull length.

Five different values of the prismatic coefficient were then selected, ranging between 0.6 and 0.7, after consulting data on the most optimal values for drag. The total volume was estimated previously after surveying current commercial AUG models and was set at 0.06 m^3. Now, for each value of fr and C^p, the total length of the glider can be obtained through the definition of the prismatic coefficient:

$$C^p = \frac{\bigtriangledown}{\pi\frac{d^2}{4}L} \Rightarrow C^p = \frac{\bigtriangledown}{\pi\frac{(L/D)^{-2}}{4}L^3} = \frac{\bigtriangledown}{\pi\frac{(fr)^{-2}}{4}L^3} \Rightarrow L = (\frac{4\bigtriangledown fr^2}{\pi C^p})^{\frac{1}{3}} \tag{3.9}$$

Once the length is determined, the nominal diameter follows, through the definition of the fineness ratio. In addition, the length of the midbody is selected as a function of the prismatic coefficient, so the length of the tail can be considered dependent solely on the length of the nose. Therefore, for each value of a, the parameters ϑ and n can be tuned in order to obtain the desired total volume. In general, by increasing ϑ and n, the total volume will increase, since the nose and the tail will become "fuller".

To automate this process, a script was written in Matlab which, from a starting set of prismatic coefficients, fineness ratios, nose lengths and a specific volume, automatically creates a series of hull designs which will have ϑ and n as far as possible from their range boundaries. In total, about 10000 different configurations were created and examined before determining the optimal design.

3.5 Drag calculation and optimization methods

Once the hull geometries are generated, it is necessary to calculate their zero-lift drag. For the sole purpose of evaluating the total drag acting on the hull, a possible option would be to execute a CFD analysis. But this is quite costly, and is especially inconvenient when an optimization process is involved, since it would mean that for every iteration or configuration a CFD analysis would have to be repeated (or multiple analyses, depending on the type of optimization). Proper analyses can take up to several hours for grids that are fine enough to reach convergence, so an optimization process with hundreds of iterations could take months, making the use of CFD analysis excessively time consuming and computationally demanding. In this case, there isn't even a proper optimization process happening, but rather a survey of over 10000 different configurations, making the idea of using CFD analysis even more preposterous. Additionally, the approximations made to the Reynolds stresses in the RANS equations can be very wrong at times, especially when dealing with boundary layer transition. Therefore the drag calculation will be made by analyzing a 2D geometry, i.e. the profiles that were drawn with the previously described Myring method. Even after reducing the body of revolution to a bidimensional figure, a 2D CFD analysis can still be quite expensive to use for optimization, so a more basic panel method approach will be used. Panel methods are numerical schemes which solve the Prandtl-Glauert equation (or potential equation) for linear, inviscid and irrotational flows, reported below:

$$(1 - M_\infty^2)\Phi_{xx} + \Phi_{yy} = 0 \tag{3.10}$$

where Φ is the flow potential, of which the velocity is the gradient, and M_∞ is the free-stream Mach number, although it will small enough to be neglected. To do so, panel methods discretize the surface of an object in a flow and each of the geometry elements is transformed in an appropriate flow element, such as a sink, a source or a doublet, in order to satisfy the appropriate boundary conditions (most often that of impermeability). Panel methods take into account element interactions and also impose the condition that, far enough from the object to be analyzed, the flow tends to become the same as the freestream. This type of problem is going to be much easier to solve than the Reynolds Averaged Navier Stokes (RANS) equations that conventional CFD deals with, which will be dealt with in chapter 5.

Clearly the fact that the panel method applies to inviscid flows is a serious hindrance to the accuracy of the solution of a real flow, so it generally is combined with an integrated boundary layer method. Among the softwares that make use of these methods are OpenVSP and xFoil, which will both be used to a certain extent. OpenVSP allows to create 3D geometries and make assessments on their aerodynamic qualities with a variety of methods, and it will be described more in detail in the next paragraphs. XFoil uses an iterative method to integrate the boundary layer in its calculations. After making an initial inviscid calculation of the solution, it modifies the shape of the initial geometry, thickening it, in order to take into account the presence of a boundary layer displacement thickness, which slows down the flow near the body's walls. This generates a drag coefficient component and produces a decrease in lift, for a calculation obtained at a specific angle of attack. The drag's friction component can be calculated through Von Karman's flat plate analogy.

$$C_f = 2\frac{d\delta^2}{dx}$$

$$C_F = \int_0^L \frac{C_f}{L}\,dx = \int_0^L 2\frac{d\delta^2}{dx}\,dx = 2\delta_L^2 = C_D\frac{S_{ref}}{S_{wet}}$$

This is then compared to the drag coefficient calculated through Squire-Young's formula, in which it is simply a function of the boundary layer momentum thickness at the tail of the object.

$$C_D = 2\frac{\delta_{L,upper}^2}{c}\left(\frac{U_{e,upper}}{V_\infty}\right)^{\frac{H_{upper}+5}{2}} + 2\frac{\delta_{L,lower}^2}{c}\left(\frac{U_{e,lower}}{V_\infty}\right)^{\frac{H_{upper}+5}{2}}$$

where H is the ratio between boundary layer momentum thickness and boundary layer displacement thickness, also known as shape factor. So for each iteration the C_D is calculated and the shape of the profile is modified to take into account

the boundary layer, until a convergent solution is reached. The results that xFoil provides have been proven to be remarkably accurate even when compared to 2D CFD simulations, at least when dealing with low velocity streams, where the flow can be deemed incompressible, and with thin objects at reasonable angles of attack.

Although both softwares will be used, none of them will actually directly calculate the drag of the hull.

One might get the idea that using xFoil to predict the fluid-dynamic properties of an axisymmetric body with a null angle of attack may not be that illicit. But while it may feel like a clever idea, it can be problematic and can generate varying results, especially when using specific flow transition models. In fact, even when using a 2D CFD method, this will prove to be inadequate[5]. A different approach will have to be taken into consideration for a simplified evaluation of drag.

3.5.1 The Granville Method

Paul S. Granville came up with a method to estimate the parasitic drag of an axisymmetric body and described it in 1953 in his report "The calculation of viscous drag of bodies of revolution"[6]. This method only requires to know beforehand the shape of the mid-section of the body and the 2D pressure coefficient distribution along it, which can be determined with xFoil in less than a second.

The Granville method uses a number of approximations and assumptions made with the aid of experimental data to estimate the momentum area Ω at the boundary layer transition, at the end of the thin turbulent boundary layer, at the tail and at infinity. The total drag is then calculated as:

$$D_{rag} = 2\pi\rho_w U_\infty^2 \Omega_\infty \tag{3.11}$$

The momentum area far at the downstream is defined as

$$\Omega_\infty = \int_0^\infty \frac{u}{U_\infty}(1 - \frac{u}{U_\infty})r\, dr \tag{3.12}$$

Unfortunately, this method, mostly due to the large number of approximations, is not always very reliable, especially when dealing with more unconventional shapes. Nowadays it isn't really used much for drag calculation, but it isn't completely obsolete. The most interesting part about it is the estimation of the location of the boundary layer transition, for which the Granville method has been used to this day with fairly good results.

To quote Granville, "transition in the low-turbulence condition may be considered to be where vanishingly small disturbances are amplified in the boundary layer to the catastrophic point of resulting turbulence within the boundary layer".

This indicates the existence of a neutral stability point, upstream of which all the frequencies of all disturbances are damped out. This point can be found as a function of R_{δ^2} and the pressure gradient parameter $\frac{\vartheta^2}{\nu}\frac{dU_{edge}}{dx}$. R_{δ^2} is defined as the boundary layer Reynolds number:

$$R_{\delta^2} = \frac{\delta^2 U_{edge}}{\nu} \tag{3.13}$$

where δ^2 is the local boundary layer momentum thickness, U_{edge} is the velocity at the edge of the boundary layer and can be determined as a function of the local pressure coefficient:

$$C_p = 1 - (\frac{U_{edge}}{U_\infty})^2 \tag{3.14}$$

Mangler has made a chart, listing $R_{\delta^2,N}$ as a function of the pressure gradient parameter, reported in figure 3.4.

It is then necessary to plot R_{δ^2} along the length of the hull as a function of $\frac{\vartheta^2}{\nu}\frac{dU_{edge}}{dx}$. R_{δ^2} can be computed as a function of $(\frac{l}{L})$ through the following formula:

$$\frac{R_{\delta^2}^2}{R_L} = \frac{4}{9}\frac{1}{(\frac{U_{edge}}{U_\infty})^4(\frac{r}{L})^2}\int_0^{l/L}(\frac{U_{edge}}{U_\infty})^5(\frac{r}{L})^2 sec(\alpha)\, d(\frac{l}{L}) \tag{3.15}$$

The pressure gradient parameter can also be computed as a function of $(\frac{l}{L})$:

$$\frac{\vartheta^2}{\nu}\frac{dU_{edge}}{dx} = \frac{R_{\delta^2}^2}{R_L}\frac{1}{(\frac{U_{edge}}{U_\infty})^2}\frac{d(\frac{U_{edge}}{U_\infty})}{d\frac{l}{L}}cos(\alpha) \tag{3.16}$$

It is then possible to plot R_{δ^2} as a function of $\frac{\vartheta^2}{\nu}\frac{dU_{edge}}{dx}$ and see where it intersects with Mangler's curve, in order to find $(\frac{l}{L})_N$, the point where boundary layer transition occurs. This process was automated with a script on Matlab.

3.5.2 Flat plate analogy method

OpenVSP is a software developed by NASA which can employ a vast number of techniques to evaluate the aerodynamic qualities of a flying system. Among its functionalities is the Parasite Drag tool, which calculates the zero-lift drag of aerospace structures through the analogy of drag to that of a flat plate. It uses relatively simple methods that nonetheless give reasonably accurate results. There are two downsides to its use though: the first is that bodies in OpenVSP are modelled in very different ways compared to the Myring method, making it difficult to reproduce on it the geometries generated with Matlab. In addition, the Parasite Drag tool requires the user to input the percentage of laminar flow

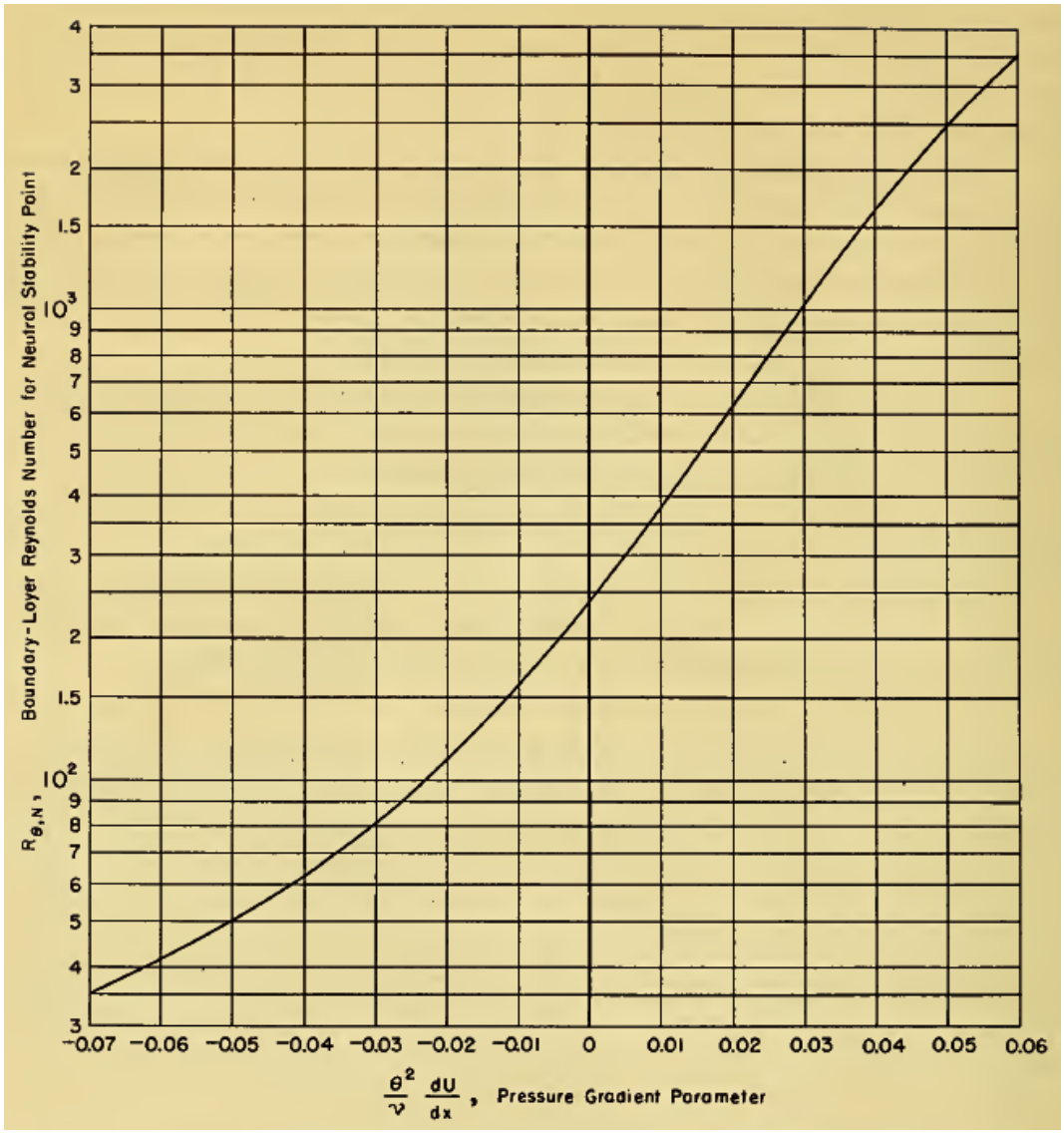

Figure 3.4: Mangler's neutral stability points.

investing the wetted surface. For most applications this is not a problem, since the majority of fuselages have minimal portions of laminar flow which can be reasonably estimated, but this is not the case for the AUG to be designed. Fortunately both these problems can be solved fairly easily: while OpenVSP won't be used per se, its documentation[7] allows to retrieve exactly its method to calculate the parasitic drag, making it possible to replicate it entirely on Matlab. The second issue is solved by using the Granville method to determine the portion of lamiar flow.

In order to estimate the total Drag, OpenVSP uses the following formula:

$$D_{rag} = FF \cdot C_f \cdot Q \cdot S_{wet} \tag{3.17}$$

FF is the form factor and is evaluated as a function of the fineness ratio fr.

There are multiple formulas to evaluate it, based on various experimental results, but in the case of the AUG, the one used will be Hoerner's streamlined body equation:

$$FF = 1 + \frac{1.5}{fr^{1.5}} + \frac{7}{fr^3} \tag{3.18}$$

C_f is the averaged skin friction coefficient and is calculated as

$$C_f = C_{f,Turb} + C_{f,PartLam}\%Lam - C_{f,PartTurb}\%Lam \tag{3.19}$$

where $C_{f,Lam}$ is calculated through the Blasius equation

$$C_{f,Lam} = \frac{1.32824}{\sqrt{R_L}} \tag{3.20}$$

and $C_{f,Turb}$ instead has multiple empirical formulations, among which it was decided to select Prandtl's power law for low Reynolds numbers:

$$C_{f,Turb} = \frac{0.074}{R_L^{1/5}} \tag{3.21}$$

$C_{f,PartTurb}$ and $C_{f,PartLam}$ have the same formula as $C_{f,Turb}$ and $C_{f,Lam}$, but their Reynolds number is multiplied by %Lam.

The factor Q takes into account interference drag, but will be set to 1, at least when solely dealing with the hull. Finally the wetted area S_{wet} can be calculated as the sum of the lateral surfaces of the truncated cones that compose the glider discretized by the Matlab script. It is possible at this point to calculate the drag force acting on any hull configuration.

3.5.3 Form factor correction

The previous method, although fairly simple, is generally quite sound, but it does have a significant shortcoming: its form factor is solely dependent on the fineness ratio. For most applications, while reductive, this is a reasonable simplification, but when trying to determine the optimal nose length, it will not provide accurate end results. By using the formulas described in section 3.5.2, one could obtain minimum drag values with extremely long noses that take up nearly 100% of the length of the hull, since there would be a larger stretch of laminar flow and therefore a lower C_f. The error in that would be not taking into account the fact that by moving the location of the maximum diameter too far downstream, large adverse pressure gradients can be generated, with an increasing risk of severe boundary layer separation and a consequent drastic increase in pressure drag.

In order to take into account the effect of shifting the maximum diameter region

towards the aft, the same formula to determine the form factor was maintained, but a new one to determine a "corrected" fineness ratio was developed. Rather than it being simply the ratio between the total hull length and the maximum diameter, it will be:

$$fr(a,b) = \begin{cases} \dfrac{L}{D}, & \text{if } a + b/2 \leq 0.5L \\ \dfrac{2(L-a-b/2)}{D}, & \text{if } a + b/2 > 0.5L \end{cases} \tag{3.22}$$

In other words, when considering the effective fineness ratio, once the middle of midbody is past half the length of the hull, the fineness ratio will decrease, as shown in the figure below. This correction only applies as long as the corrected fineness ratio is greater than approximately 3.3. Beyond those values, as the maximum radius approaches the trailing edge, the corrected fineness ratio approaches zero and the form factor tends to infinity. This correction is not based on any specific method or data, it is only present to prevent an excessively optimistic drag prediction when the nose of the tail of the hull is very short and hosts strong separation phenomena.

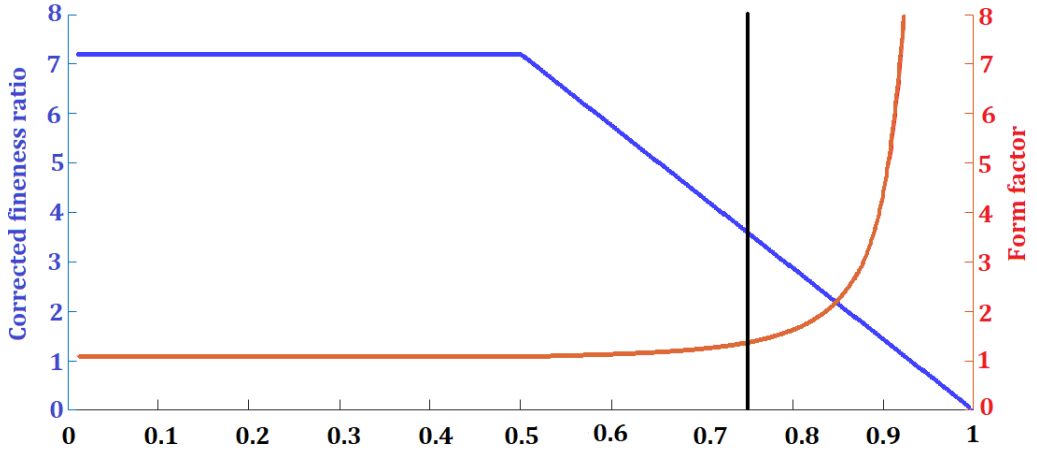

Figure 3.5: Corrected fineness ratio and form factor as a function of the nose length a. In this case b=0, fr=7.2. The black line marks the limit of this model.

3.6 Method validation

The method used, while computationally convenient, seems suspiciously simple. In general, especially when it comes to 3D bodies, CFD simulations are generally required, and even those can be unreliable when dealing with boundary layer transition. Instead, the total drag of the hull, through the method previously described, boils down to a form factor (solely dependent on the fineness ratio and on the location of the maximum diameter), to the total wetted surface, and to a generalized skin friction coefficient (which is dependent only on the Reynolds

number and on the bi-dimensional pressure distribution over the mid-section of the hull). Therefore it is necessary to verify how accurate or inaccurate this model is, by comparing its results with some experimental data.

The data comes from three different sources: the first is Myring's report on drag over axisymmetric bodies, the second is an article from Gao et al on hull shape optimization[8] and the third is Hoerner's book "Fluid-dynamic drag"[9], which contains large amounts of experimental data. The bodies by Myring start from an initial configuration which has the nose length equal to 15% of the total fuselage length, the midbody equal to 55% of the total length, a nose index of 1.25 and a tail angle of 10°. From there, the nose index and the tail angle were changed to see how they would affect the volumetric drag coefficient CD_V. The volumetric drag coefficient uses as a reference surface the volume to the power of 2/3, making the CD_V a more appropriate parameter to consider when designing an aerodynamic component with a constrained volume. In figures 3.6 and 3.7, the effects of n and ϑ are plotted for both Myring's results and the results of the computations from the method of this study. From these figures, it is possible to notice that Myring's data reports a slightly higher drag coefficient, although the difference is in the order of 1%. Both experimental and analytical results have similar trends, in which both n and ϑ have very small effects. The latter is slightly more influential, since the tail takes a larger portion of the length of the hull. It must also be noted that these changes are mostly due to the changes in wetted surface, while neither really has a significant effect on pressure distribution. The nose index parameter though will become a lot more important when the nose becomes longer, not only for its effect on the surface and volume variations, but especially because it will strongly affect the location of the boundary layer transition. Another set of data from Myring is on the effect of the fineness ratio on the portion of friction drag. Figure 3.8 compares it with Matlab's computations. This is possibly the most reductive aspect from the OpenVSP model, since the friction to total drag ratio will simply be the inverse of the form factor. Despite this, the results aren't too far off, although they become less precise for smaller fineness ratios. Finally, the model should be tested at different Reynolds numbers, so it was first compared with the experiments of Gao et al, who manufactured a hull with a nose length of 18.5% the hull, a midbody with a length of 33% the hull, a nose index of 2, a tail angle of 38° and a fineness ratio of 5.4. The total drag was measured at velocities varying from 0.3 to 1.7 m/s, for an equivalent Reynolds number varying from $3.6 \cdot 10^5$ to $2.04 \cdot 10^6$. The results are compared in figure 3.9, in which it can be seen that Granville and the flat plate analogy can produce accurate results for lower velocities, but lose precision with increasing Reynolds number, underestimating the total resistance. The experimental results in the study of Gao have a strange trend

though, possibly caused by unaccounted water tunnel effects, or by an increase in turbulence intensity.

Additionally, a large sample of data is provided at a wide range of Reynolds numbers, fineness ratios and streamlined shapes by Hoerner. These are compared in figure 3.10 with various ellipsoids of varying fineness ratios generated on Matlab, where the colored lines are the ellipsoids tested with the method to be evaluated. It is difficult to assess how different the results are, since the streamlied bodies' shapes are quite different, but it is possible to see that the trends of the various curves are similar nonetheless.

In the light of these results, it is clear that the method adopted is not sufficient to accurately predict the drag of an axisymmetric body, but only to make a first estimate. However, the drag coefficient trends are quite similar for varying n, ϑ, fr and Re. Therefore, the method can be used to search for an optimal geometry, which will then have to be properly analyzed through the use of CFD software and wind tunnel experiments.

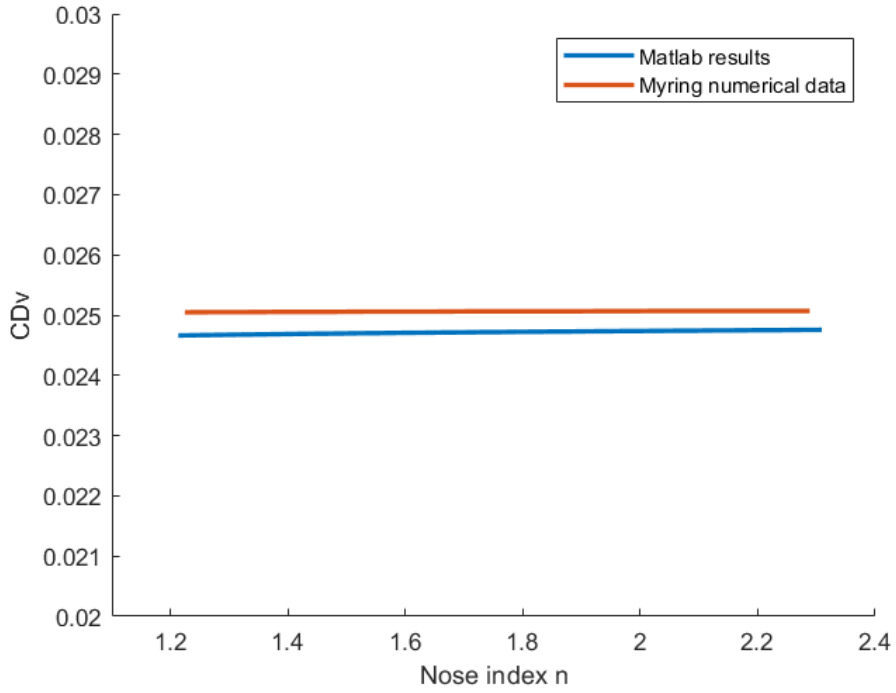

Figure 3.6: Effect of the nose index on volumetric drag coefficient at a Reynolds number of 10E7.

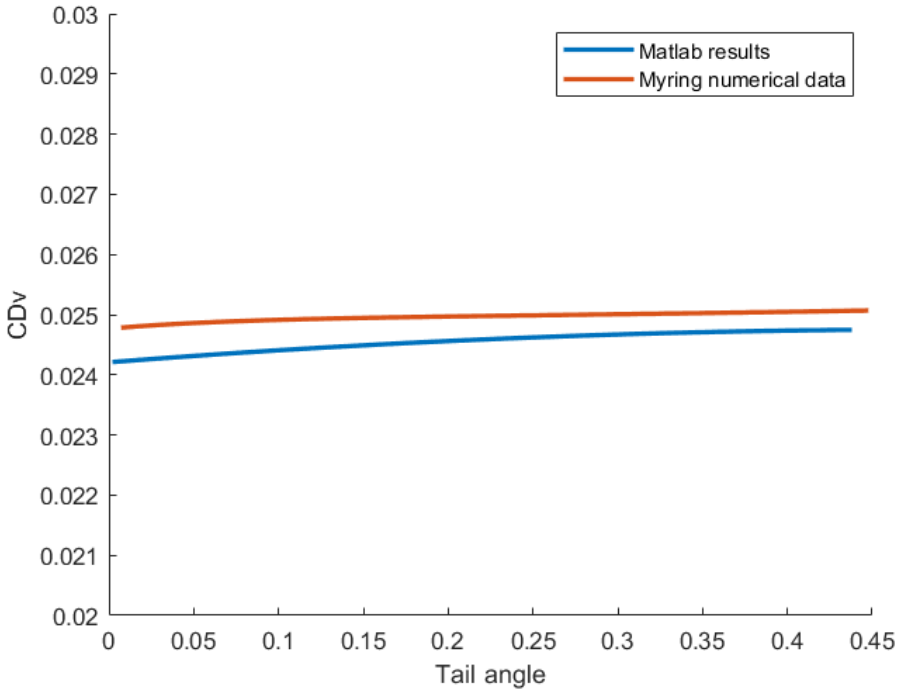

Figure 3.7: Effect of the tail angle on volumetric drag coefficient at a Reynolds number of 10E7.

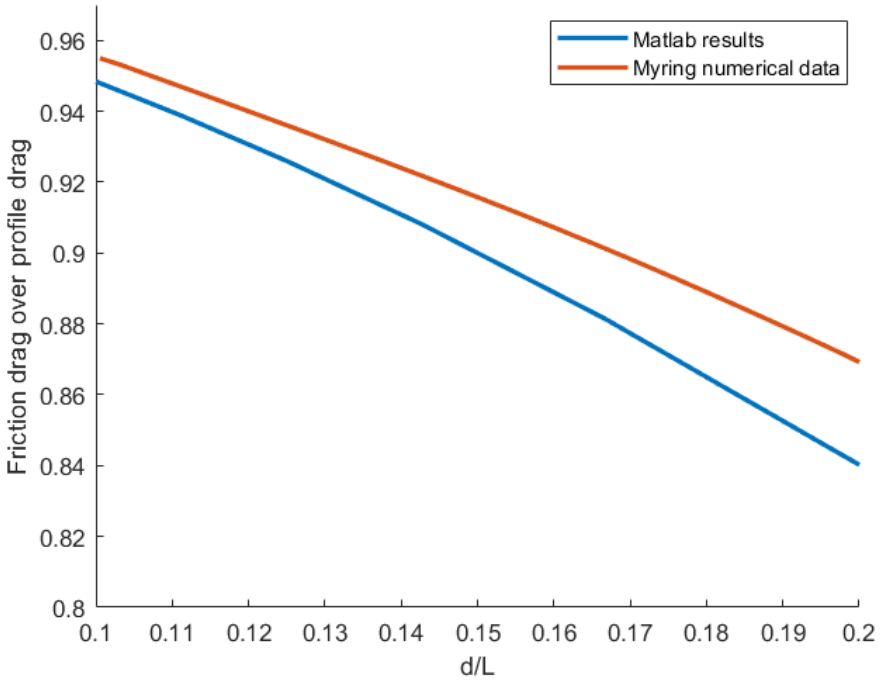

Figure 3.8: Effect of the fineness ratio on volumetric drag coefficient at a Reynolds number of 10E7.

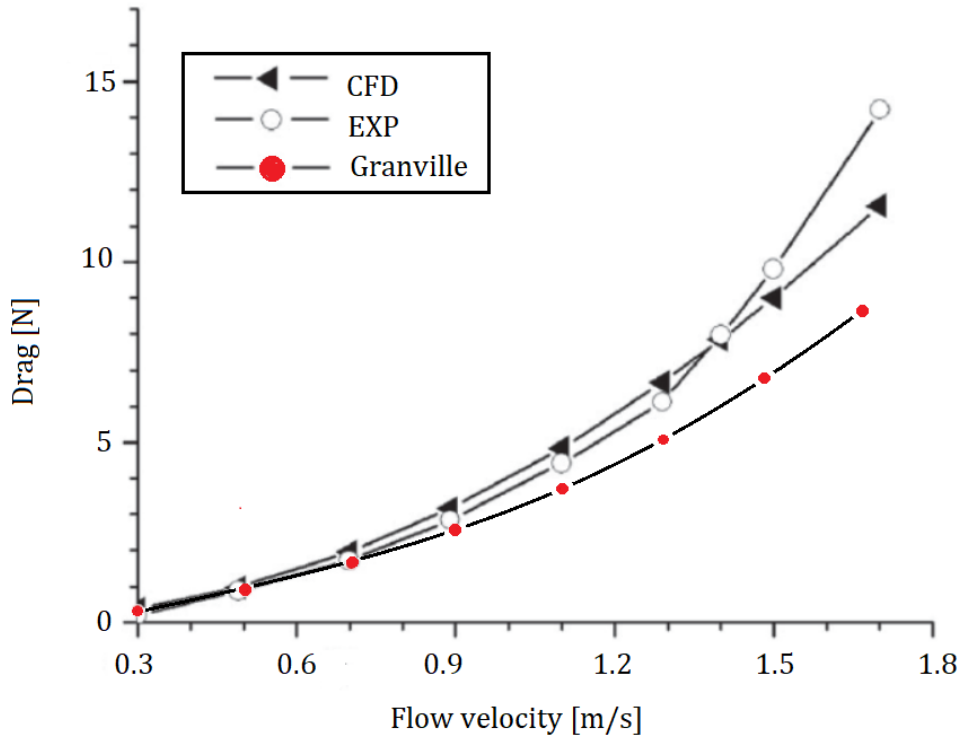

Figure 3.9: Total hydrodynamic resistance as a function of the flow's free-stream velocity.

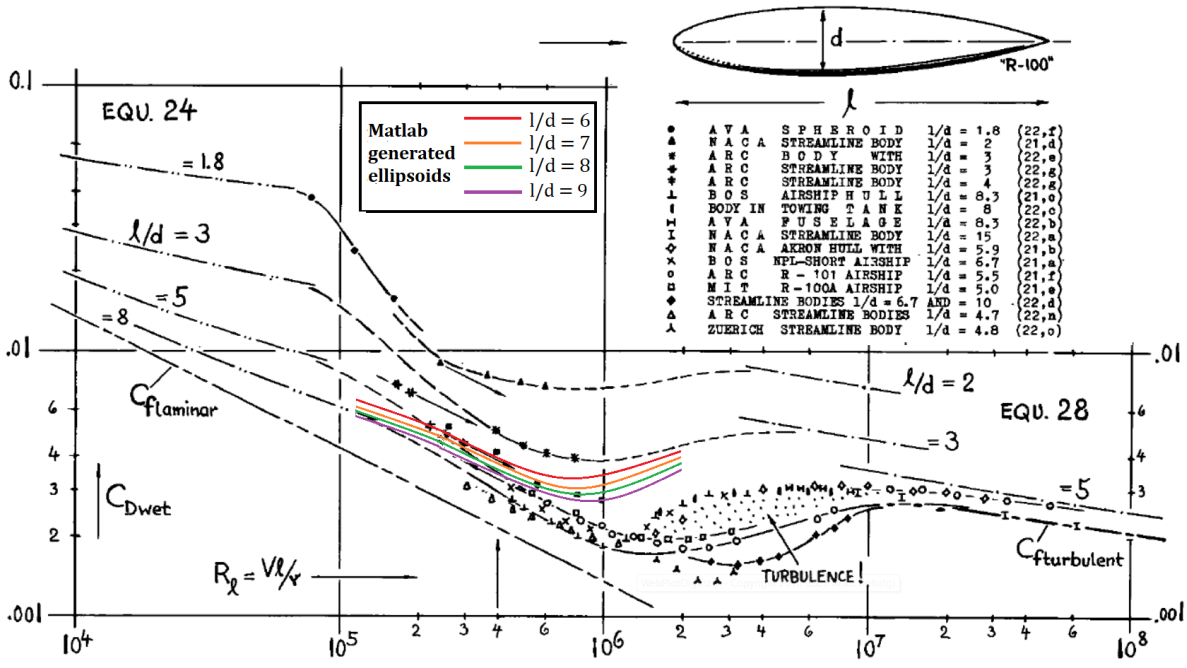

Figure 3.10: Experimental drag coefficient in reference to wetted surface for different streamlined bodies at varying Reynolds and fineness ratio, compared to Matlab results obtained for ellipsoids at varying fr and Re.

3.7 Results and final design

At the end of the design process, about 10000 different configurations were created to have their zero-lift drag estimated when traveling at a velocity of 0.5 m/s in water at a temperature of 283.15 K. While different combinations of fineness ratio and nose length were able to give nearly optimal results, the absence of a midbody and a prismatic coefficient equal to 0.6 always proved to be the better option. The presence of a section with constant diameter can be detrimental most likely because it increases the pressure peak, doesn't favor the development of a laminar boundary layer and requires steeper angles at the tail, increasing the odds of flow separation.

Considering the graphs shown below, the lowest hydrodynamic resistance is encountered with a hull with a fineness ratio of 7.4 and a nose length $a \simeq 0.62L$. The drag tends to decrease with a longer nose, due to the larger portion of laminar flow and therefore lower skin friction coefficient, to increase again once the nose is longer than 65% of the hull. The increase is caused by the flow separation which occurs when the recovery region becomes too small. Additionally, once a certain value of nose length is passed, not only does it increase the pressure drag, but it also diminishes the fraction of laminar flow, as depicted in figures 3.12, 3.14, 3.16 and 3.18.

The fineness ratio has a more complex effect on the total drag. In general, a high fineness ratio will minimize resistance due to pressure, but beyond certain values the differences become irrelevant and other effects come into play. First of all, a higher fineness ratio means a higher surface to volume ratio, meaning that for a fixed volume there is a larger wetted area and therefore more friction drag. In addition, a higher fr also means a longer hull, and consequently a higher Reynolds number, which on one hand lowers the laminar and turbulent C_f, but on the other hand might also anticipate the boundary layer transition. For conventional submarines, generally the best fr is somewhere between 6.0-7.0, depending on the Reynolds number at which they operate, but since the hull in question is meant to delay the flow transition, it is to be expected that even a larger surface may not be as detrimental, and therefore the optimal fr can be higher than that. For much higher fineness ratios though, the surface increases more significantly and somewhat surprisingly, the fraction of laminar flow decreases quite consistently with higher fr, with the exception of when the prismatic coefficient is 0.6. A possible explanation could be that higher fineness ratios mean also smaller favorable pressure gradients, making the flow more prone to go through transition earlier.

Overall, not only did the lack of a midbody and the prismatic coefficient fixed at 0.6 prove to be the most hydrodynamic solution, but it is noticeable that increasing

both consistently increases the total drag, as shown in figure 3.19. Additionally, the drag computations are reported for the case in which the prismatic coefficient is set at 0.625, 0.65, 0.675 and 0.7. It can be noticed that the nose length does not have the same influence in these cases. This is because the midbody, although relatively small (8.6% of the total hull length), tends to anticipate the transition and keep it fixed for a wide range of values of a, where the fraction of laminar flow is more dependent of the fineness ratio.

While the best shape has a null midbody, it should be noted that almost all commercial AUGs have at least a small section in which the diameter remains constant. This could very well be due to space constraints, to fit the battery pack (which also needs some additional space to move in order to control pitch and roll), the buoyancy engine, the payload etc. Therefore, besides the configuration that minimizes drag, an additional design was picked with a prismatic coefficient of 0.65 and a midbody of 8.6% the length of the hull. In table 3.3 are the parameters that define their geometries, which are also shown in figures 3.20 and 3.21. The two hulls will be named respectively CP60 and CP65.

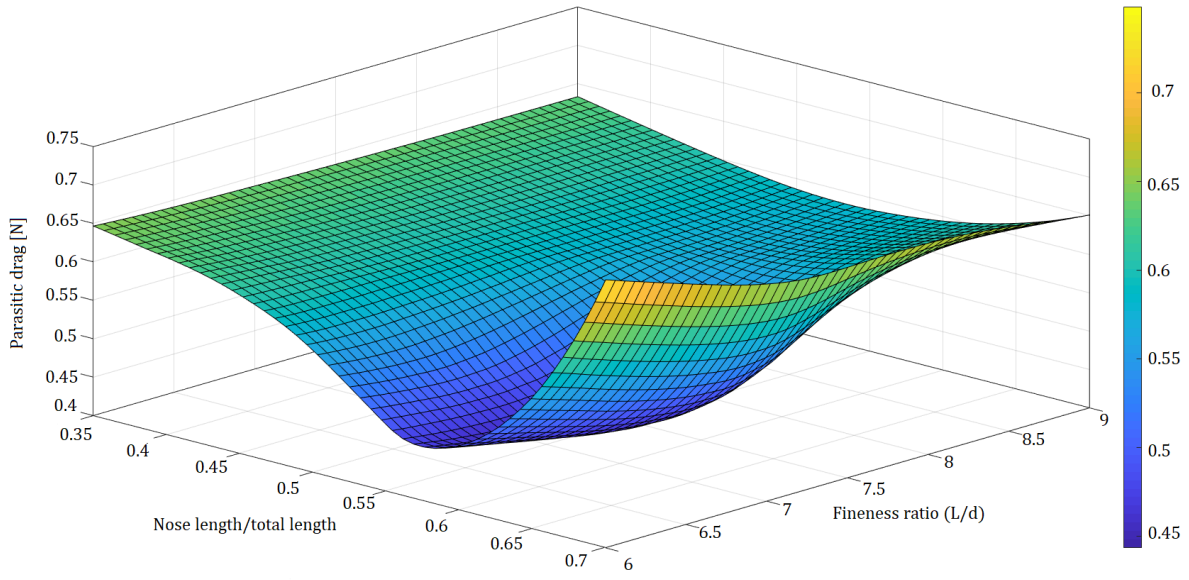

Figure 3.11: Drag force as a function of nose length and fineness ratio for a prismatic coefficient of 0.6.

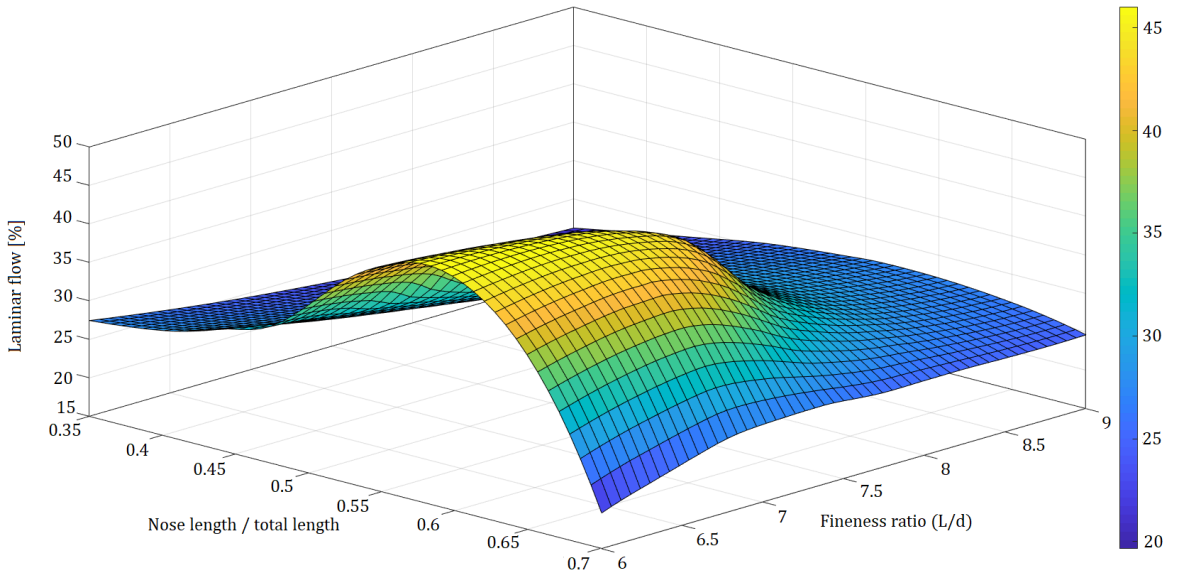

Figure 3.12: Fraction of hull length invested by laminar flow as a function of nose length and fineness ratio for a prismatic coefficient of 0.6 and no midbody.

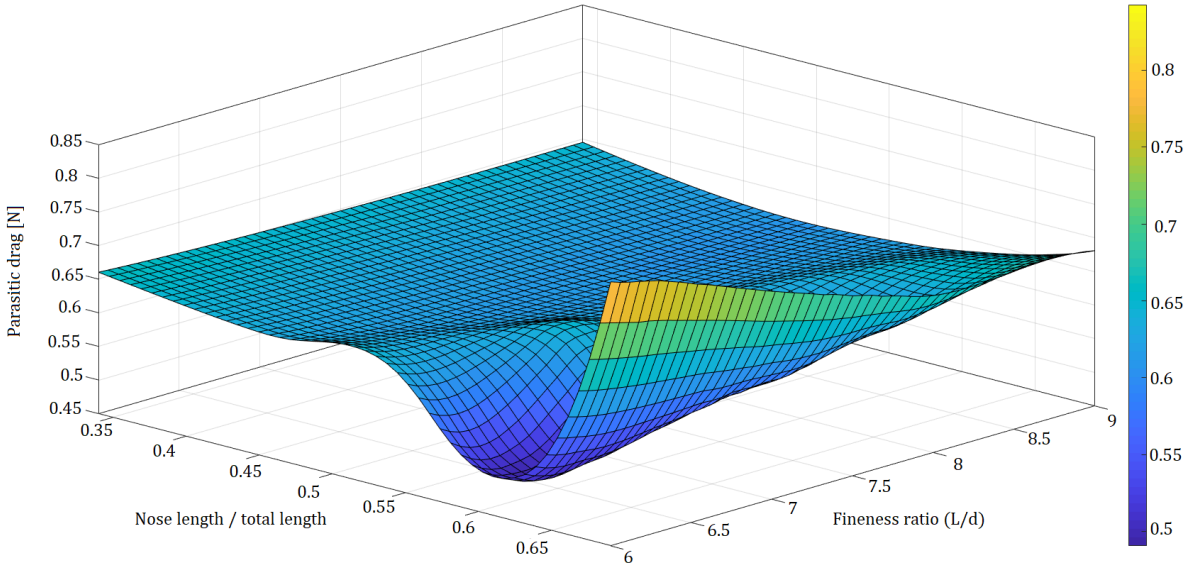

Figure 3.13: Drag force as a function of nose length and fineness ratio for a prismatic coefficient of 0.625.

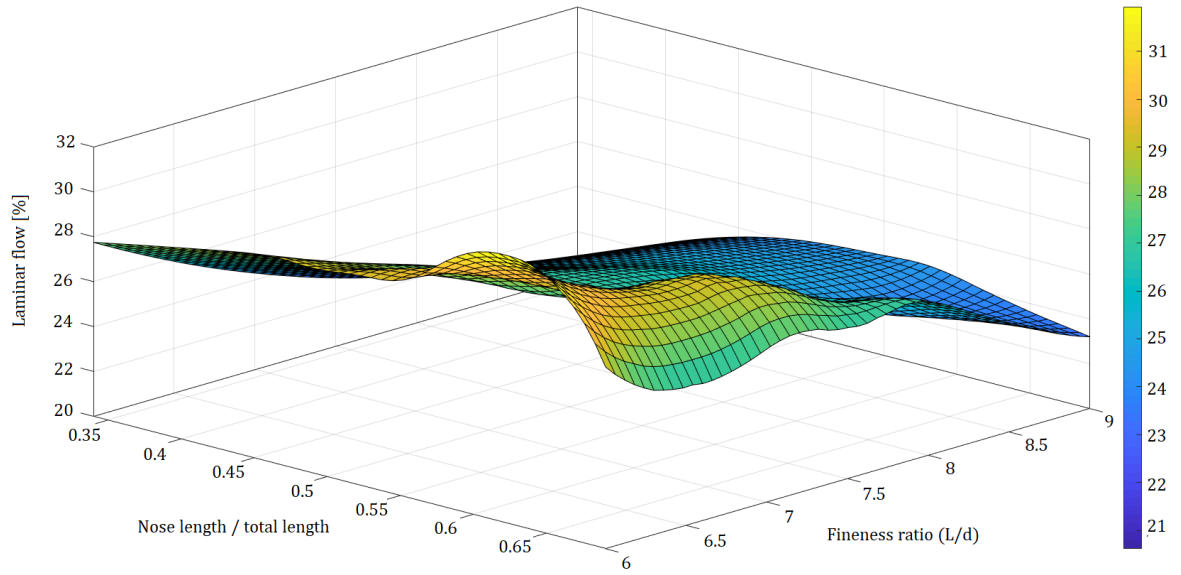

Figure 3.14: Fraction of hull length invested by laminar flow as a function of nose length and fineness ratio for a prismatic coefficient of 0.625 and a midbody b = 0.040 L.

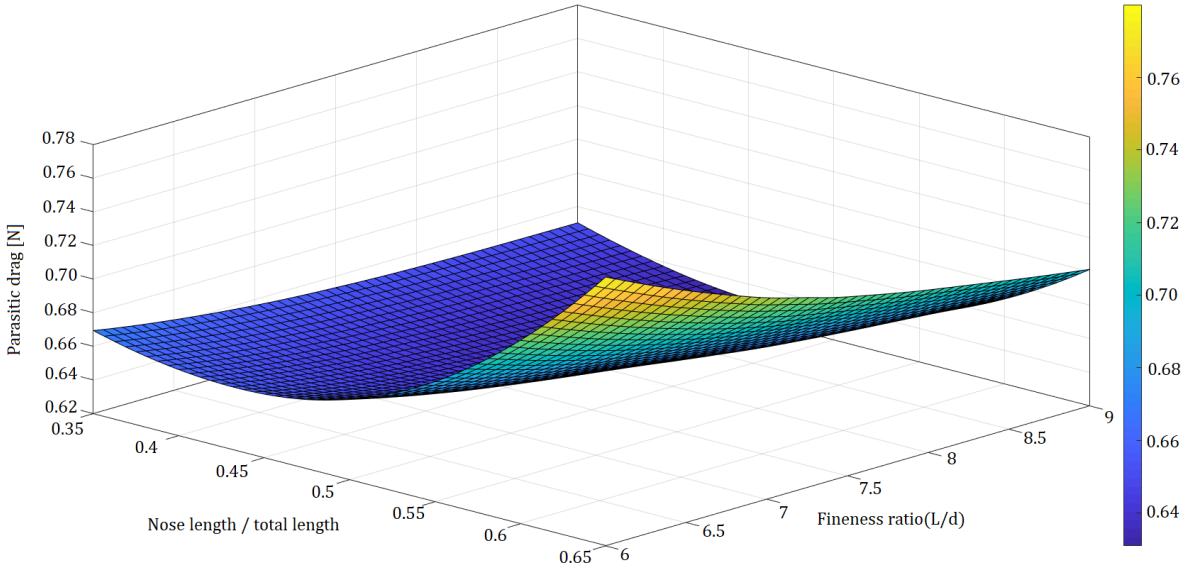

Figure 3.15: Drag force as a function of nose length and fineness ratio for a prismatic coefficient of 0.65.

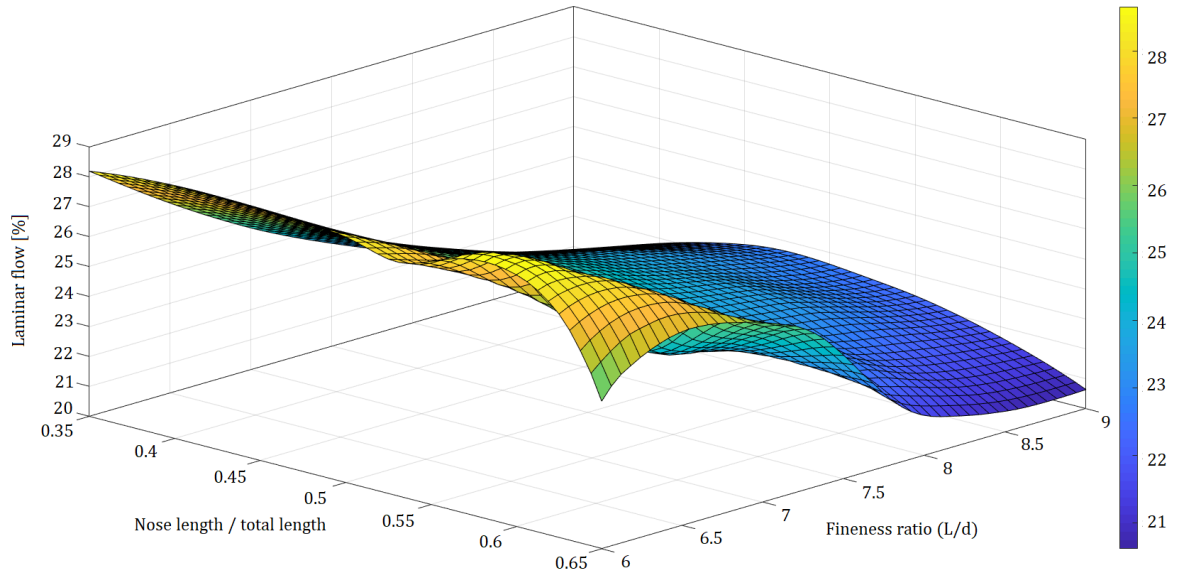

Figure 3.16: Fraction of hull length invested by laminar flow as a function of nose length and fineness ratio for a prismatic coefficient of 0.65 and a midbody b = 0.086 L.

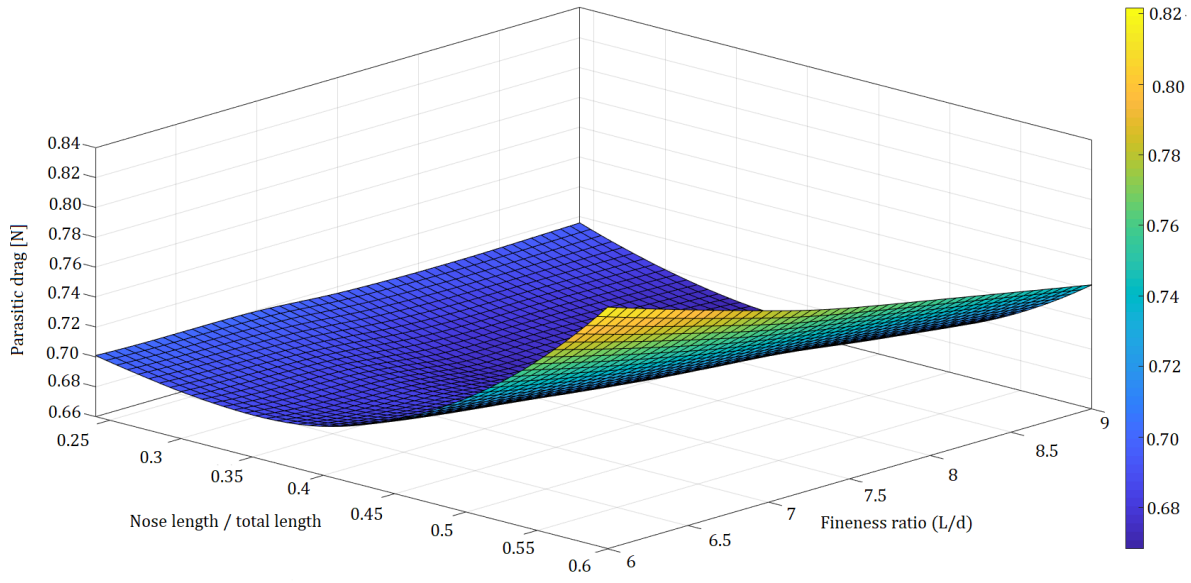

Figure 3.17: Drag force as a function of nose length and fineness ratio for a prismatic coefficient of 0.7.

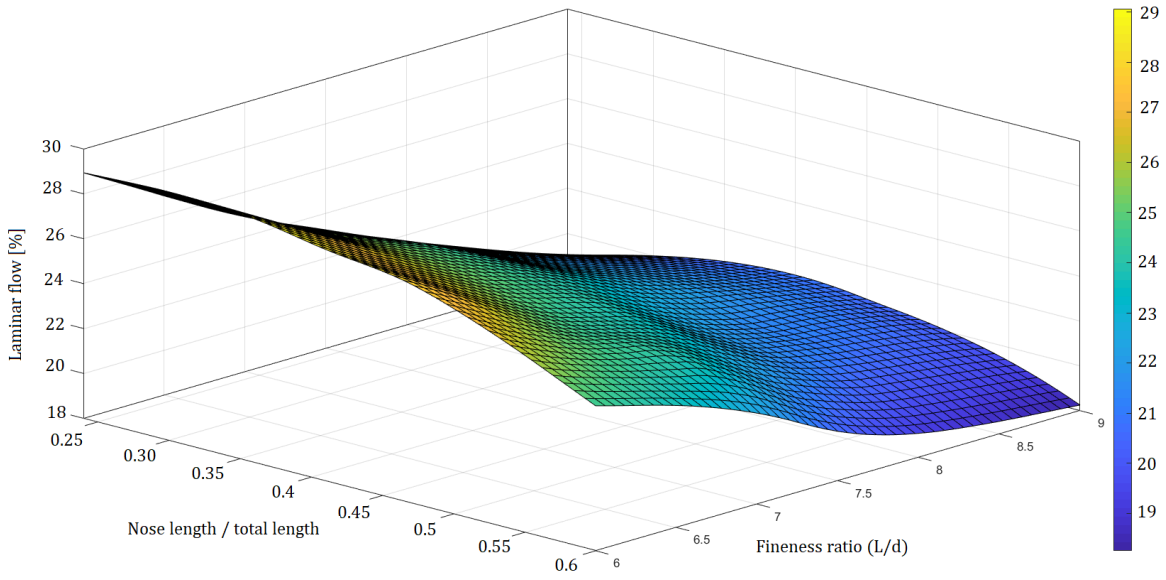

Figure 3.18: Fraction of hull length invested by laminar flow as a function of nose length and fineness ratio for a prismatic coefficient of 0.7 and a midbody b = 0.185 L.

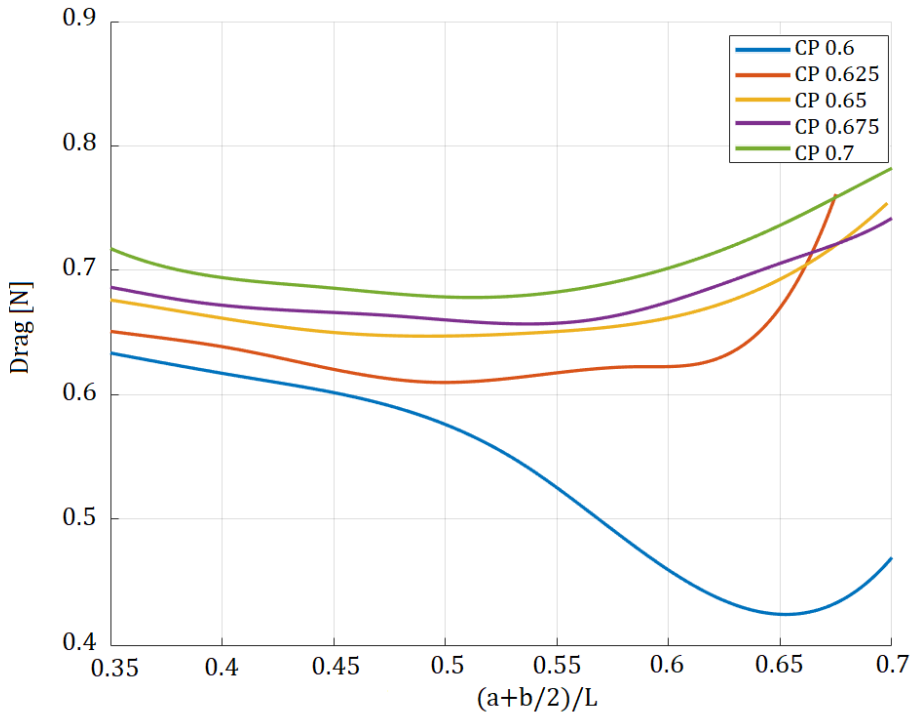

Figure 3.19: Total drag as a function of maximum diameter location and prismatic coefficient at a fineness ratio of 7.4.

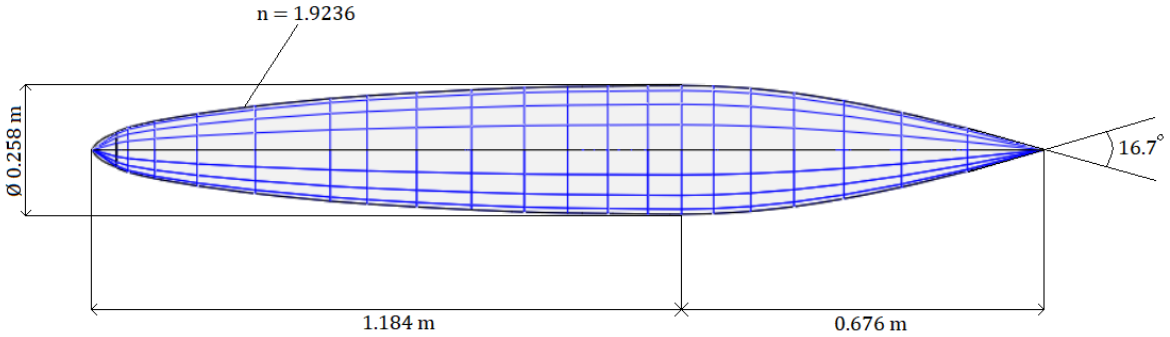

Figure 3.20: Side view of the CP60 design.

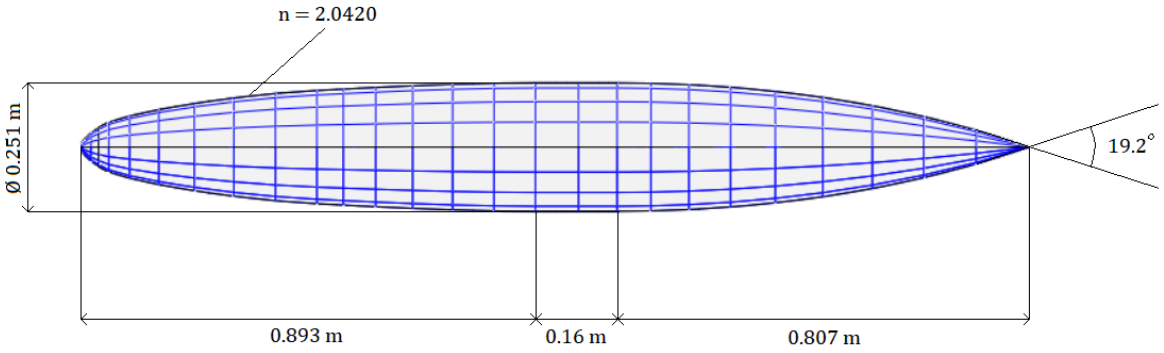

Figure 3.21: Side view of the CP65 design.

Glider geometry		
AUG	**CP60**	**CP65**
Length L	1.91 m	1.86 m
Maximum diameter d	25.8 cm	25.1 cm
Nose length a	1.184 m	0.893 m
Midbody length b	0 m	0.16 m
Tail length c	0.726 m	0.807 m
Nose index n	1.9236	2.0420
Tail angle ϑ	0.2915 rad	0.3351 rad
Prismatic coefficient C^P	0.60	0.65
Fineness ratio fr	7.4	7.4
Wetted surface S	1.134 m^2	1.129 m^2
Volume	0.06 m^3	0.06 m^3

Table 3.3: Selected hull configurations' geometrical parameters.

Chapter Bibliography

[1]Volker Bertram, 2012, *Submarine Hull Design*, from classes at NTNU

[2]E. S. Arentzen, P. Mandel, 1960, *Naval Architectural Aspects of Submarine Design*, SNAME

[3]S. S. Dodbele, C. P. van Dam, 1986, *Design of Fuselage Shapes for Natural Laminar Flow*, NASA Contractor report 3970

[4]D. F. Myring, 1981, *A theoretical study of the effects of body shape and Mach number on the drag of bodies of revolution in subcritical axisymmetric flow*, Royal Aircraft Establishment, Technical report 81005

[5]Erfan Kadivar, Ebrahim Kadivar, Seyed Morteza Javadpour, 2021, *Numerical Prediction of Lamiar to Turbulent Transition Around the Prolate Spheroid*, Journal of Marine Science and Application, DOI: 10.1007/s11804-020-00184-w

[6]Paul S. Granville, 1953, *The calculation of the viscous drag of bodies of revolution*, Navy department, The David Taylor Model Basine, Report 849

[7]http://openvsp.org/wiki/doku.php?id=parasitedrag

[8]Ting Gao, Yaxing Wang, Yongjie Pang, Jian Cao, 2016, *Hull shape optimization for autonomous underwater vehicles using CFD*, Engineering Applications of Computational FluidMechanics, DOI: 10.1080/19942060.2016.1224735

Further readings of interest:

D. Dress, 1989, *Drag Measurements on a Modified Prolate Spheroid Using a Magnetic Suspension and Balance System*, AIAA 89-0648, DOI: 10.2514/3.25314

Falk Gotten, Matthew Marino, 2021, *Improved Form Factor for Drag Estimation of Fuselages with Various Cross Sections*, Journal of Aircraft, Vol. 58, No. 3, DOI: 10.2514/1.C036032

A. Nakayama, V. C. Patel, 1973, *Calculation of the Viscous Resistance of Bodies of Revolution*, IIHR Report No. 151

Sighard F. Hoerner, 1965, *Fluid Dynamic Drag*

Chapter 4

Wing Design

In general the design process of a wing proceeds by treating independently the 2D airfoil and the wing planform. Once those are drafted the design gets into more detail and the two are modelled in a 3D context, generally through the aid of CFD software and/or wind galleries. In the case of AUGs, there are some aspects that make it less than ideal to operate in such manner, as it will be explained in the next paragraphs.

Chapter Symbology

a_0	Lift curve slope
b	Wingspan
c	Airfoil chord length
e	Oswald coefficient
p	Local pressure
q	Dynamic pressure
r_0	Nose radius
M	Pitching moment
AC	Aerodynamic center of a wing or airfoil
AR	Aspect ratio of the wing
TR	Taper ratio
Ma	Mach number
Re	Reynolds number
S	Planform surface
V	Relative velocity between a body and a fluid
CP	Center of pressure of an airfoil
C_D	Drag coefficient
C_L	Lift coefficient

C_m	Pitching moment coefficient
C_p	Pressure coefficient
t	Airfoil thickness
α	Angle of attack
ϑ	Trailing edge angle
ε	Twist angle distribution
ρ	Density of the fluid
μ	Coefficient of dynamic viscosity
ν	Coefficient of kinematic viscosity, $= \mu/\rho$
Λ	Sweep angle of the wing
$_{,l}$	Subscript indicating a property of the lower surface
$_{,u}$	Subscript indicating a property of the upper surface
$_{,ind}$	Subscript indicating an effect induced by lift

4.1 Hydrodynamic concepts for wing design

In the hull design chapter, the parasite drag and its relation to boundary layer phenomenons were discussed. These concepts can also be applied when considering a 2D airfoil. Until now though, hardly any mention has been made on lift, which is the main reason for wings to exist.

-Lift is the component of the aerodynamic force which is perpendicular to the relative velocity between a specific body and fluid in motion. Similarly to drag, its formula is the following:

$$L_{ift} = \frac{1}{2}\rho U^2 S_{ref} C_L \tag{4.1}$$

This force is the one used to counter gravity (or buoyancy in the case of underwater gliders). The lift coefficient C_L is going to be a function of the geometry and of the angle of attack α. In the specific case of wings, α is the angle between the oncoming stream and the chord of the airfoil.

An optimal wing, while fulfilling the targets required by its mission, will have to operate with the highest possible lift to drag ratio, or aerodynamic efficiency. The optimal shape of an airfoil is highly dependent on the flow conditions under which it operates, specifically on the Reynolds number and the angle of attack (and consequent C_L). In the next section, some of the parameters that affect airfoil performance will be described.

In the case of thin airfoils, the lift coefficient increases proportionally to the angle of attack, until it reaches its stall value, after which it starts decreasing. What triggers the stall is the gradual separation of the boundary layer over the top surface that occurs with the increase of α. Related to this is also a dramatic increase in parasite drag. Before stall is reached, the drag of a 2D airfoil will be

roughly proportional to the square of the lift.

The most important aspect that will determine the development of lift and the overall aerodynamic performances over an airfoil is the distribution of the pressure coefficient. In figure 4.1 is an example of how the C_p distribution varies as a function of the angle of attack.

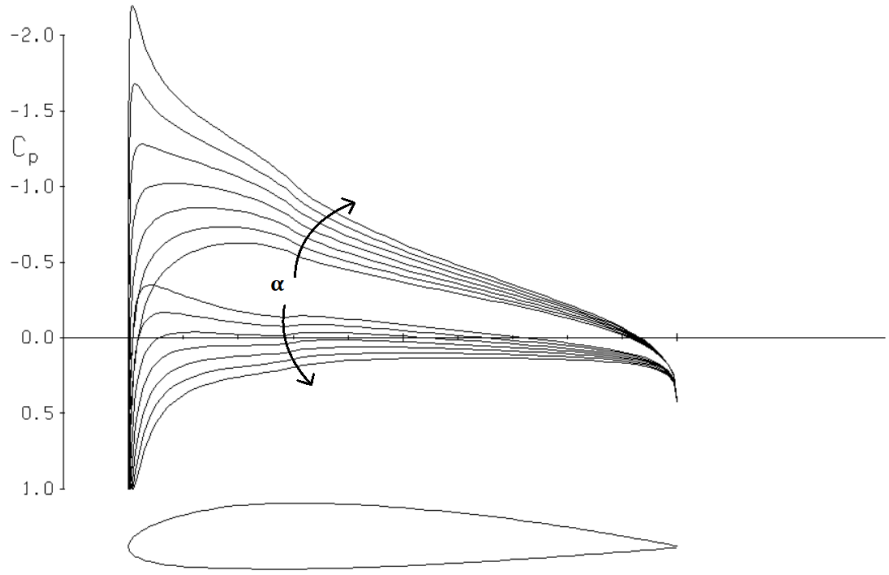

Figure 4.1: Pressure distribution over a generic airfoil at varying angles of attack.

As it can be seen, the C_p of the top surface has a negative peak that increases with the angle of attack. After the peak, there is the so called "recovery region" in which the pressure will increase to the value at the trailing edge. The higher the peak, the more lift can be generated, but at the same time, it will need an increasingly large adverse pressure gradient, which increases the odds of flow separation occurring. The lift coefficient can be calculated as:

$$C_L = \int_0^1 (C_{p,l} - C_{p,u}) d(x/c) \tag{4.2}$$

so it is conceptually the area comprised between the $C_{p,l}$ and $C_{p,u}$ curves. According to Stratford, in order to maximize the performances of an airfoil, the C_p should be designed so that the boundary layer is brought to the verge of separation across the entire length of the chord. While theoretically this is an ideal design, in practice wings designed under this principle tend to be too sensible to flight condition changes. Finally, it should be noted that the generation of lift does not occur through an increase of pressure over the bottom surface, but rather a decrease in pressure over the top surface which sucks the wing upwards.

-Induced drag was already mentioned in the previous chapter, but it wasn't

delved into very deeply, as it is negligible to the design of a hull. However, when dealing with the planform of a wing, it becomes a crucial aspect. It was previously said that it is caused by the trailing vortices generated at the wingtips. These vortices generate a downward vertical velocity component which generates an induced angle of attack α_i. Without indulging in demonstrations, the consequent induced drag coefficient can be calculated as:

$$C_{D,i} = \frac{C_L^2}{\pi\, AR\, e} \tag{4.3}$$

with AR being the aspect ratio and e being the Oswald efficiency number, a correction factor that is equal to 1 for 3D wings with an elliptical lift distribution and that decreases the more a wing deviates from that optimal configuration.

-When considering the tridimensionality of a wing, another aspect that needs to be taken into consideration is the **lift slope reduction**. It was already mentioned that, for a 2D airfoil, the lift coefficient increases linearly with the angle of attack, so $\frac{dC_L}{d\alpha} = a_0$. For a wing with a finite aspect ratio, $\frac{dC_L}{d\alpha}$ will decrease to:

$$\frac{dC_L}{d\alpha} = \frac{a_0}{1 + \frac{a_0}{\pi\, AR\, e}} \tag{4.4}$$

and the effect can be seen in figure 4.2.

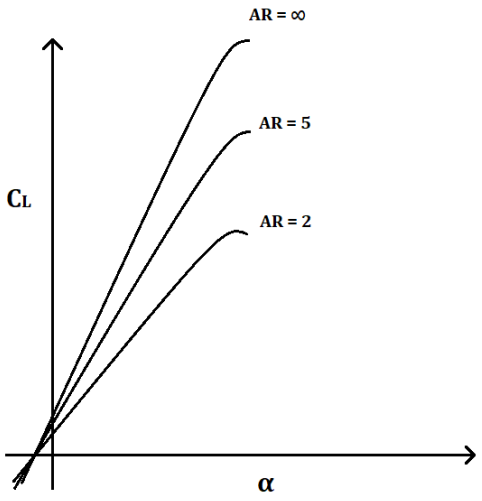

Figure 4.2: Lift slope reduction on a generic airfoil as a function of the wing's aspect ratio.

-The distribution of pressures generated by the aerodynamic phenomena can be substituted by the lift and drag forces acting on the **pressure center CP**. The position of the CP is not fixed and tends to move towards the leading edge with an

increase of α. It can be calculated as:

$$CP = \frac{\int x\, p(x)\, dx}{\int p(x)\, dx} \tag{4.5}$$

-The fact that the center of pressure has a variable position might suggest that for any point of the wing there will be a **pitching moment M**, which will vary with the angle of attack. In general, the pitching moment is adimensionalized through the **moment coefficient** C_m, defined as

$$C_m = \frac{M}{q\, c\, S} \tag{4.6}$$

where q is the dynamic pressure $\frac{1}{2}\rho V^2$. Additionally, the fact that lift increases linearly with the angle of attack but the pressure center moves towards the leading edge can suggest that there could be a point in which the pitching moment remains constant. As a matter of fact this is true and such point is called the **aerodynamic center AC**. It can be proven that for thin airfoils it is located approximately at the quarter chord. In other words, at that point $\frac{dC_m}{dC_L} = 0$. The aerodynamic center is particularly convenient to evaluate the aerodynamic properties of a wing.

4.2 Design parameters

In this paragraph a list of the most notable parameters for wing design will be made, making the distinction between airfoil and planform.

4.2.1 Airfoil

-The first parameter to be taken into consideration is the **chord length c**, which is the distance between the leading edge and the trailing edge. For airfoil evaluation and design softwares, the chord length isn't even taken into consideration, as everything is adimensionalized. In general the chord length is implicit in the definition of the Reynolds number, since for airfoils it will be calculated as:

$$Re = \frac{\rho\, c\, V}{\mu} = \frac{c\, V}{\nu} \tag{4.7}$$

If one is to design a wing by stating its ideal cruise velocity, then the chord will obviously affect the Reynolds number, which in turn will have a profound effect on the optimal shape of the airfoil.

-Another defining measurement for an airfoil is its **thickness t**. The ratio between it and the chord will strongly affect the C_p distribution. A higher t/c

will make it harder to reach high negative pressure peaks without boundary layer separation. However, minimal thickness does not necessarily mean better performances, and in fact most airplanes that fly $Ma > 0.5$ will generally have fairly thick airfoils, which aid with the recompression of supersonic bubbles, which has the effect of diminishing wave drag. Instead, for lower Reynolds numbers, thin airfoils are usually better suited to mitigate the effect of transition bubbles. In other words, the ideal airfoil thickness can vary significantly depending on the Reynolds number and on the Mach number, and this variation will also not be linear. The location of the maximum thickness will also have a significant effect on the development of the pressure coefficient. If it is further aft, the peak will also be further back, requiring a more adverse gradient in the recovery region.

-The **nose radius** can also have a significant impact on aero/hydrodynamic performances. Whitcomb's supercritical airfoils for example were designed with a large nose radius, while in the case of low Reynolds numbers, the nose will tend to be sharper, even though this is not a rule set in stone.

-Another important aspect is **camber**. The camber line is the line going through the points equidistant from the bottom and top surface of the airfoil. In the case of a symmetric airfoil, camber will be zero throughout it. In other words, a cambered airfoil will also be curved and asymmetric. Camber has the effect of increasing lift and a cambered airfoil can produce lift even at a null angle of attack, so its main effect is that of shifting the $C_L - \alpha$ curve upwards. A collateral effect though is the generation of an aerodynamic moment. The distribution of camber can be used to load certain regions more than others, based on specific requirements. For example, supercritical airfoils are designed to be rear loading, therefore having the maximum camber at the aft. In general though, if an airfoil is designed with a specific moment constraint, its peak lift will likely be lower than that of an unconstrained counterpart. As an example, reflexed airfoils can provide a positive pitching moment (meaning that it directs the nose upwards), by having the aft negatively cambered. This way the aft will push down, generating positive C_m, but with a negative impact on lift.

-Another parameter to be taken into consideration is the **trailing edge angle** ϑ. In many cases a minimal trailing edge angle is advised, if not a cuspid. This is to redirect the flow at the bottom and the top surface at the same angle, in order to avoid stagnation points. This is not always feasible, mostly due to construction practicality and structural stability requirements. Alternative designs can have a trailing edge with a finite thickness but with parallel upper and lower surfaces.

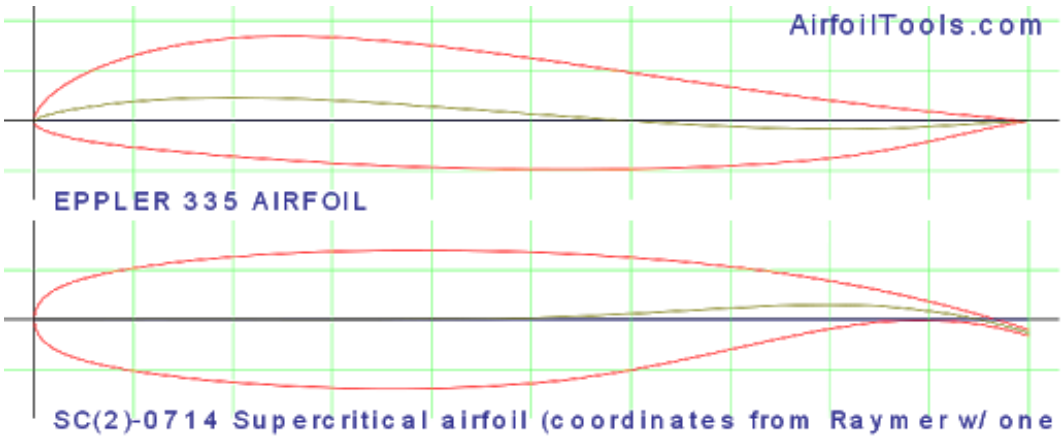

Figure 4.3: Comparison of a reflexed airfoil and a rear loaded supercritical airfoil.

4.2.2 Planform

-For a wing with a fixed surface, the most important geometrical aspect is the **aspect ratio AR**. It is defined as the ratio between the square of the span and the planform's surface:

$$AR = \frac{b^2}{S} \tag{4.8}$$

As previously noted, it is preferable to have the highest aspect ratio possible, as it will minimize induced drag and lift slope reduction. In other words, it is better to have a span as large as possible. In general, the span is limited by the maximum displacement allowed for the wing under bending moments, or by maneuverability constraints.

-The other parameter that affects aerodynamic performances is the **Oswald coefficient e**. It can be proven that the best load distribution to improve wing efficiency is the one provided by an elliptical wing shape. Any deviations from this shape must be taken into account with a correction factor. For example, the Oswald coefficient for a rectangular planform will be circa 0.96, while for a trapezoidal wing it will depend on the **taper ratio TR**, which is the ratio between chord at the root and chord at the tip of the wing. The optimal value is around 0.4, which allows for an Oswald coefficient of nearly 0.99. Double tapered wings can have e values upwards of 0.99. From these numbers it is intuitive that the aspect ratio is a lot more critical for the overall performances of the wing.

-Another aspect to be taken into consideration is the **twist distribution** ε of the wing. This is usually done in order to have the wingtips at a lower angle of attack, to ensure that they will not stall before the wing root. The reason for this is that usually the control surfaces are located towards the tips of the wings, so if partial stall conditions are met, it should still be possible to control the aircraft. In the case of AUGs though, roll and yaw are controlled solely through the internal

ballast and sometimes through the rudder, so wingtip stall is not as catastrophic as in normal airplanes. Nonetheless, a proper tuning of the twist angle can help to optimize the wing's lift distribution and to improve its efficiency, since the chord at the tip is smaller and therefore the local Reynolds number and stall angle are also smaller.

-The planform of the wings can also be defined by their **sweep angle** Λ. In general though, this will only have negative effects on aerodynamic performances, as the lift produced by a swept wing is smaller than an unswept counterpart. On the other hand it can help improve latero-directional stability. Swept wings are most popular among planes that travel at transonic or supersonic speeds, since they allow to delay the formation of shock waves. AUGs though do not have to deal with challenging manoeuvres and do not even come close to moving at transonic speeds, so the presence of a sweep angle will not be taken into consideration for hydrodynamic purposes, but a small Λ can help with avoiding entanglements.

-Lastly, a mention on **winglets** should be made. These are surfaces placed at the tips of the wing which aid the redirection of the flow in order reduce the intensity of the wingtip vortices. They are most useful when due to constraints it isn't possible to have an optimal taper ratio, either for structural stability reasons, which lead the wingtips to be smaller in order to reduce the bending load, or for aerodynamic reasons, which lead the wingtips to have a larger chord in order to avoid stall phenomena. On the other hand, they increase the total parasite drag without giving a contribution to lift, so they are useful only if they can give a concrete contribution in the reduction of induced drag. It is unlikely that winglets will provide a significant improvement to an AUG's performances, but nonetheless, as it will be mentioned in the optimization paragraph, the option will still be evaluated.

4.3 Constraints

Even in the case of wing design there are a number of constraints that pose limitations to an ideal hydrodynamic design. In certain cases constraints can be useful in narrowing down the range of possible solutions.

-The first constraint that should be posed is that of the wingspan. For most aircraft, its length is limited by structural integrity issues: the longer the wing, the greater the bending moment at the constrained root will be, and the higher the vertical displacement of the wingtip will be. In the case of gliders though, the wings are not subjected to high loads, so generally it isn't structural issues that limit the wingspan. Most often what limits it is the minimization of the chances of entanglements of any sort. This can be such a problem that some commercial

gliders might even have a significant sweep angle on their wings, such as the Slocum gliders, or even develop "wingless" designs, such as the SeaExplorer.

-The wing surface is conventionally constrained based on the load that it has to carry. In general it is best to have a weight to surface ratio as low as possible. In the AUG's case, the weight to surface ratio will be very low in any case, so rather than focusing on the surface, the design criteria will be posed on the mean chord, as it will be better explained in the next paragraphs. After all, for a fixed wingspan it is equivalent to define the mean chord or the total wing surface.

-Other parameters which may be constrained by structural issues are generally the air/hydrofoil thickness and the trailing edge angle. As previously stated, contrary to conventional aircraft, shear and bending loads will not be very significant. Airfoil buckling might occur nonetheless due to the high pressures that develop as a function of ocean depth.

-The dynamics of an aircraft can also pose limits to the way it is designed. In general the airfoils are designed to have a limit to their negative moment coefficient, which generally translates in a reduction in camber, and therefore in lift. This is in order to minimize the size of the stabilizers at the tail of the aircraft. AUGs though do not possess stabilizers and the hydrodynamic force acting on them is generally much smaller than that of buoyancy or gravity. Therefore, the moment coefficient of the wing will tend to be almost negligible to the overall equilibrium of the glider. The wing will have to be positioned closer to the tail of the AUG, since an aft positioning of the wings will also help delay the disruption of the laminar boundary layer over the hull.

-A significant constraint that so far all gliders have to satisfy is the symmetricity of the hydrofoils. During the dive, the upper surface of the glider will be the one at a lower pressure, while the lower surface will be at a higher pressure. But the two faces of the wing swap roles when the AUG begins its climb towards the surface. Therefore, while a cambered hydrofoil might favor the dive, it will have catastrophic hydrodynamic effects during the ascent. Additionally, the incidence angle of the wing will necessarily have to be null, and no twist distribution is applicable. The wings will also have to be posed necessarily on the same level as the hull's plane of symmetry xy. The symmetric constraint in particular can be quite detrimental for a series of reasons. First of all, almost every airfoil that has been designed to operate under low Reynolds numbers has a significant camber, suggesting that symmetric airfoils generally have worse performances in the conditions tipically encountered by AUGs. To give an idea at the difference in performances, in figure 4.4 is reported a graph taken from a study by Winslow et al[1]. Additionally, the lack of incidence angle means that the hull will always have a positive angle of attack, and therefore not only will it have an increase in drag induced by the lift it might generate, but

it probably will lose a significant portion of its laminar boundary layer, further increasing friction drag. The lack of flexibility in the positioning of the wing may also hinder the stability of the glider, requiring more work from the control system which, after the buoyancy engine, represents the highest energy expense[2][3]. Finally, even the possibility of winglets must be excluded a priori under these constraints, making it more likely to have a larger induced drag.

In light of all these limitations, the next paragraph will deal with an idea which could allow a designer to bypass the symmetric constraint of the wings.

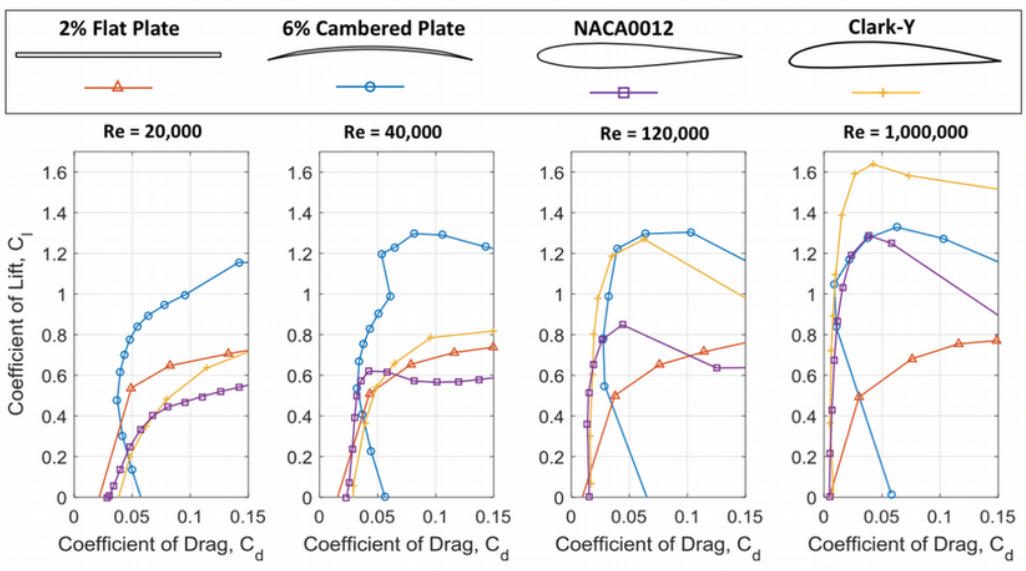

Figure 4.4: CL-CD curves for different airfoils. As can be seen, even a simple cambered plate outperforms the symmetric variants at Reynolds numbers lower than 120.000.

4.4 Removal of the wing symmetry constraint

As mentioned in the previous paragraph, the constraint which poses the largest number of limitations on the design possibilities is that of wing symmetry. However, it can be circumvented. The glider could perform a roll of 180° every time it reaches the surface or the bottom of its dive. By doing so, the roles of the upper and lower surfaces of the wings would not swap and the flight conditions would remain nearly unaltered between the two phases of the dive. On figure 4.5 is a sketch of the difference between the phases of a symmetric wing glider and those of an asymmetric one with roll.

Conveniently, the rolling motion does not require any hydrodynamic conditions, the AUG can perform such manoeuvres simply through a displacement of the battery pack. In general, the battery packs, besides moving longitudinally to

control the pitch of the glider, are also set to have an asymmetric radial distribution around the longitudinal axis of the hull. This way, by rotating it by 180°, the glider will also roll to achieve a condition of static equilibrium.

A glider that does something similar is the Spray[4][5]. Since its antennas are mounted on the wings, when it reaches the surface it rolls by 90° to have one of the wings exit the water to receive its instructions via satellite. However, there is no information available on this idea as of yet from other commercial AUG producers. In the next paragraphs it will be determined if this solution would bring enough of a hydrodynamic improvement to justify the added control complexity and the energy expenditure required to roll the AUG twice per dive. For this reason, the wing design process will be done on two variants: one with the wing symmetry constraint and one without. At the end, the two solutions will be compared to see if there really is a significant difference in performances.

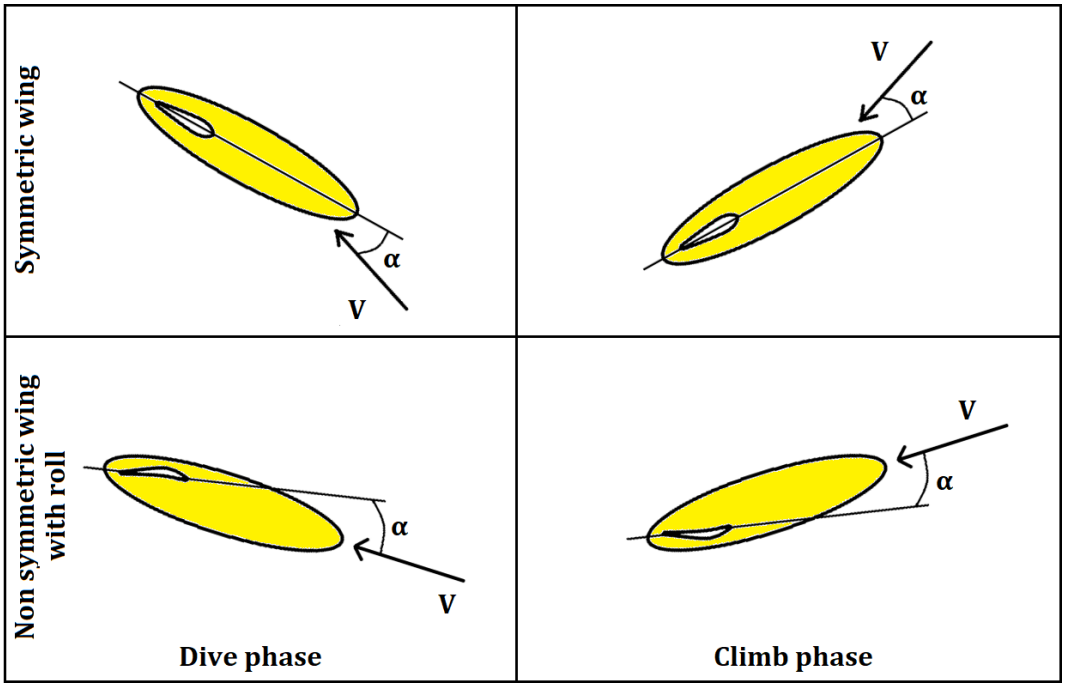

Figure 4.5: Conventional solution vs. roll solution

4.5 Design method

In this case it is not possible to design separately the airfoil and the planform, as the two will be strongly dependent on each other in terms of optimal performances. This is mostly due to the chord, which is a key parameter for both aspects of the wing. As previously mentioned, the Reynolds number is directly proportional to the chord's length, and an airfoil in general performs better at higher Re, especially

when dealing with Reynolds numbers in the range of 20.000-80.000. On the other hand, for the same planform surface, an increase in chord length means a reduction in the wings' aspect ratio, and therefore an increase in induced drag. Also, an airfoil cannot generally be proclaimed to be objectively better than an other, as different airfoils will be more or less optimal at specific Reynolds and Mach numbers, under specific loads etc. Therefore, a first design methodology must be developed just to define the optimal airfoil, chord length, wingspan and buoyant mass for a specific flight condition or mission.

The first step is to define a range of acceptable chord lengths, wingspans and buoyant masses. Looking at commercial underwater gliders, wings generally have chords ranging between 8-20 cm. To give some extra leeway, the range for experimentation will be widened to 4-30 cm, since the computational cost of the method to be described is not very high. Since the loads on the wings will generally be low, The wingspan does not need to be limited by structural constraints, but in general it will need to be bound by a more practical aspect, i.e. the minimization of the probability of entanglements. Most gliders have wingspans of 0.2-1.2 m, so those limits were set even for this project. Finally, the buoyant masses are at most equal to those of 500 cc of salt water, so this will also be the limit adopted for this project.

The next step is to make a selection of airfoil candidates to be used on the AUG. Most of the ones tested come from Selig's handbook[6], which lists the qualities of airfoils designed to operate at low Reynolds numbers. Some additional ones were found through research on airfoiltools.com[7] and through the studies of Anyoji and Hamada[8]. Among all of these, only one is symmetrical, the SD8020. Figure 4.6 makes a visual report of the selection.

At this point, for each airfoil, the polar curves are calculated with xFoil from their zero-lift to stall angles of attack with increments of 0.1° for a range of Reynolds numbers spanning from $16 - 118 \cdot 10^3$. These Re are calculated assuming an ideal glider velocity of 0.5 m/s and an average water temperature of 10°, while the chord is increased from 4 to 30 cm through increments of 2 cm. For each combination of airfoil, angle of attack and Reynolds (i.e. mean chord), through an iterative method, the wingspan which satisfies equations 4.9 to 4.11 will be calculated:

$$mg = qS(C_L\, cos(\delta) + C_D\, sin(\delta)) \tag{4.9}$$

$$L = \frac{1}{2}\,\rho\, V^2\, S_{wing}\, C_L/(1 + \frac{2}{AR\, e}) \tag{4.10}$$

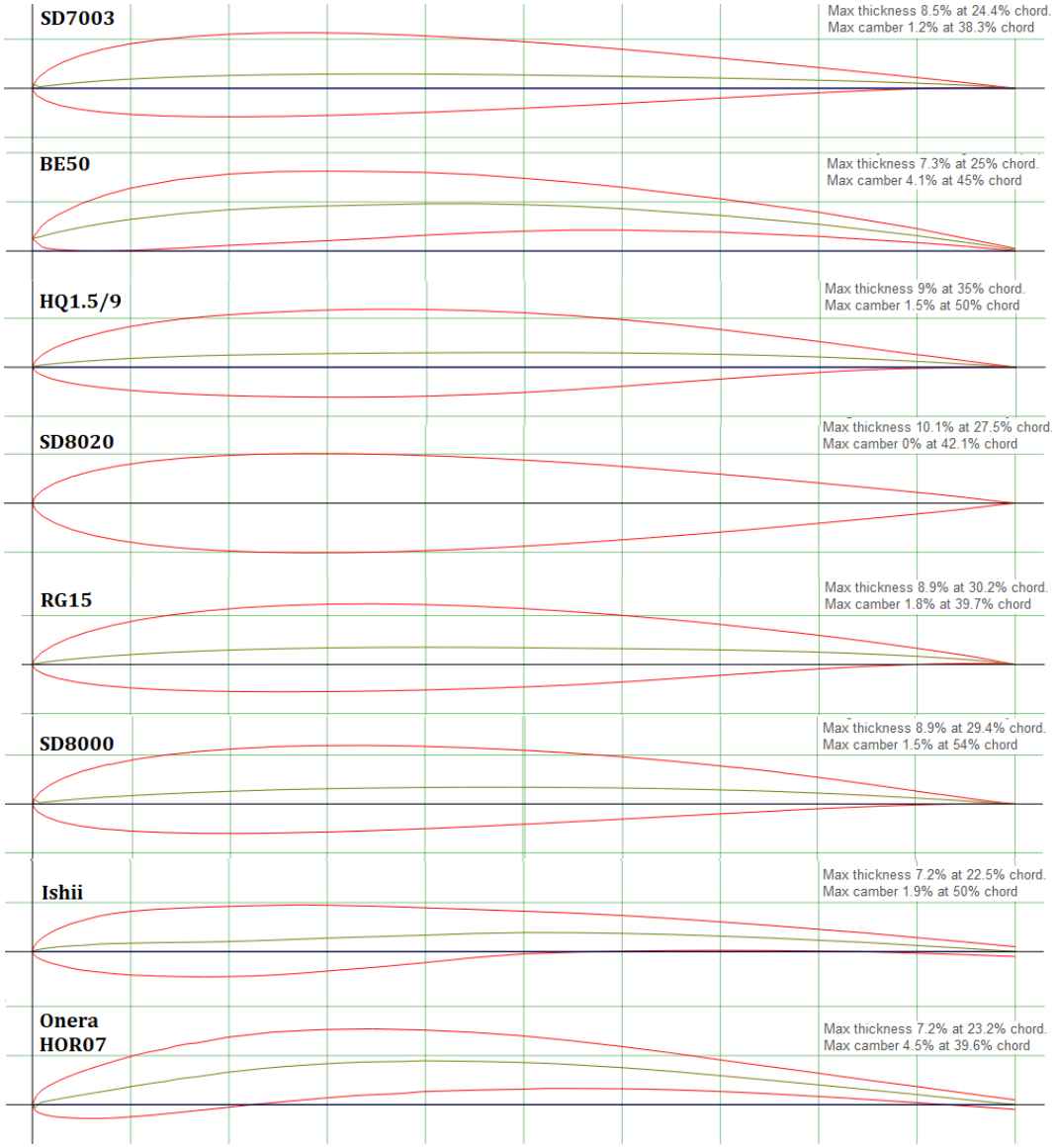

Figure 4.6: List of tested airfoils.

$$D_{rag} = \frac{1}{2}\,\rho\,V^2\,S_{wing}\,(C_D + \frac{C_L^2}{\pi\,AR\,e} + \frac{D_{rag,hull}}{0.5\,\rho\,V^2\,S_{wing}}) \tag{4.11}$$

where δ is the arctangent of the drag coefficient over the lift coefficient.

First, equation 4.9 is solved without considering induced drag and lift slope reduction in order to find a first estimate of b. This value is then inserted in equations 4.10 and 4.11 to estimate the real lift to drag ratio. These numbers are then substituted again in the first equation to find a new value of b and so on, until the difference between the wingspan in two consecutive iterations is smaller than a thousandth of its value.

The iterative process is actually solved very quickly by any commercial computer, the most computationally demanding part is the calculation of the airfoil polars,

but even that takes less than five minutes with xFoil for a conventional PC, so even when dealing with tens of airfoils, the whole process will last a few hours at most.

For each of the possible configurations, two values are defined: the hydrodynamic efficiency $E = L/D$, and the fuel efficiency $F_E = E/m$. The hydrodynamic efficiency of course indicates how much distance the glider will travel longitudinally at each dive, so in a way it can give an indication of how energy efficient the glider will be. However, for increasing velocities, higher glide ratios will be achieved through larger buoyant masses. Since most of the energy consumed by the glider is to fuel the buoyancy pump, and since it is directly proportional to the mass of displaced fluid, F_E is a better indicator of how energy efficient the glider will be. So which of the two parameters should be optimized? To reach a conclusion, an example will be made.

Consider the airfoil HQ1.5/9. Applying to it the previously described method, depending on which of the two parameters will be chosen to be optimized, the following results will be obtained:

Wing configurations		
-	**Optimized hydrodynamic efficiency**	**Optimized energy efficiency**
Max E	6.512	2.038
Max F_E	13.024	16.307
Optimal mass	500 cc	125 cc
Optimal wingspan	1.017 m	0.497 m
Optimal chord	0.08 m	0.06 m
Optimal C_L	0.750	0.778

Table 4.2: Wing design parameters as a function of the chosen optimization criteria.

In order to achieve maximum hydrodynamic efficiency, the largest possible buoyant mass must be used (the equivalent of 500 cc of water in this case), so a larger wing surface will be needed for similar lift coefficients. In general the trend, which applies to every one of the airfoils that were considered, is to have a larger buoyant mass and wingspan when optimizing E. So in the case in which F_E is optimized, the glider will be more energy efficient and will have a smaller wingspan, which can be particularly advantageous in specific situations (see the SeaExplorer glider). At the same time though, it will also have a much smaller longitudinal

velocity and its maximum glide ratio will be significantly smaller. To show this even better, the velocity polars for the two possible optimizations will be shown in figure 4.7.

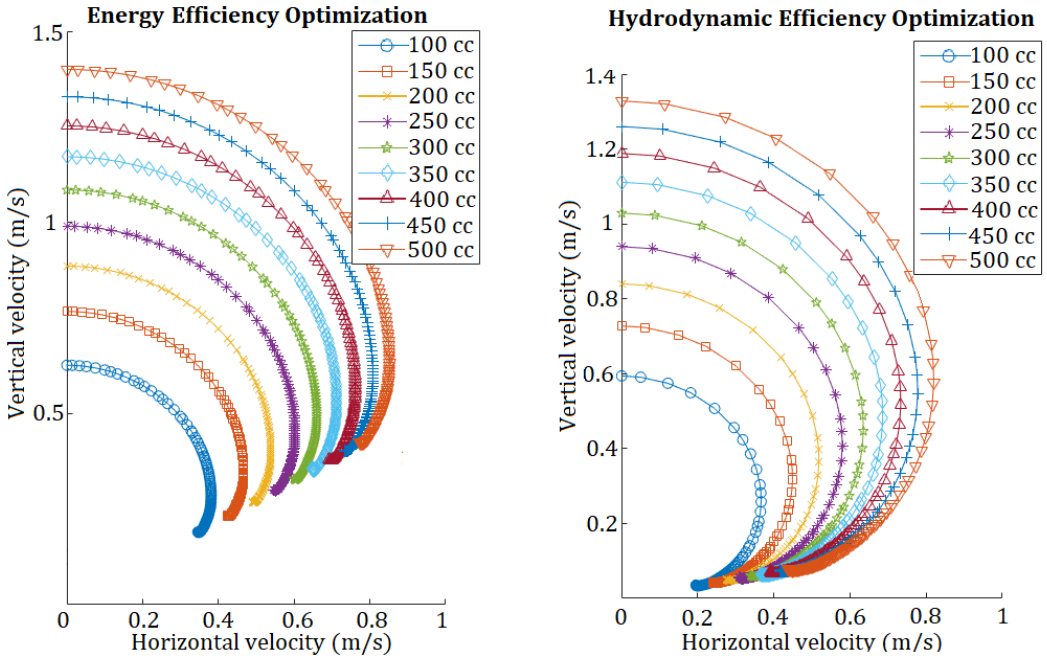

Figure 4.7: Differences between velocity polars for gliders with optimized hydrodynamic efficiency (left) and gliders with optimized energetic efficiency (right).

So if the designer is solely interested in energy efficiency and perhaps operates in less than clear waters, F_E might be the best parameter to optimize. But if the designer is also interested in versatility of the glider, optimizing E might be the better option, since the energy efficiency will not be excessively hindered. For this project, the optimization will be focused on attaining the maximum hydrodynamic efficiency.

Table 4.3 reports all the optimal wing designs for each of the airfoils tested. All of them reach their optimal hydrodynamic efficiency with a buoyant mass of 0.5 kg, equivalent to nearly 500 cc of water.

The best performing airfoil is the Ishii, which has a 7% improvement in hydrodynamic efficiency even over the second best airfoil. It should be noted that the SD8020 also has surprisingly good numbers, despite its symmetricity. This is because it reaches its peak efficiency at a low C_L. In fact, operating at high C_L may not be ideal in this case, since the wing load can be very small. Therefore, airfoils which are specifically designed to reach a high lift coefficient at low Reynolds numbers may not necessarily be the best solution. A big problem of the SD8020 though is that its 2D efficiency can strongly decrease from its maximum for very low variations in the angle of attack, making it harder to control the glide angle.

Wing configurations					
Airfoil	**Chord**	**Wingspan**	**CL**	**E**	F_E
SD7003	0.14 m	0.958 m	0.5235	6.197	12.394
BE50	0.12 m	0.783 m	0.8232	5.926	11.852
HQ1.5/9	0.08 m	0.958 m	0.8206	6.200	12.400
SD8020	0.12 m	1.035 m	0.5222	6.193	12.386
RG15	0.10 m	0.831 m	0.8565	6.015	12.030
SD8000	0.10 m	0.905 m	0.7452	6.174	12.348
Ishii	0.10 m	1.009 m	0.5640	6.642	13.284
Onera HOR07	0.18 m	0.905 m	0.4787	5.925	11.850

Table 4.3: Wing design parameters as a function of the chosen optimization criteria.

A possible idea that was thought of in order to counter the lack of control was to use the use a rougher surface (Ncrit = 5), since it would make the slope less steep, but this did not help enough, as shown in figures 4.8 and 4.9, although it did slightly increase the hydrodynamic efficiency. Figure 4.9 is a prediction of the velocity components of the glider as a function of water displacement and angle of attack.

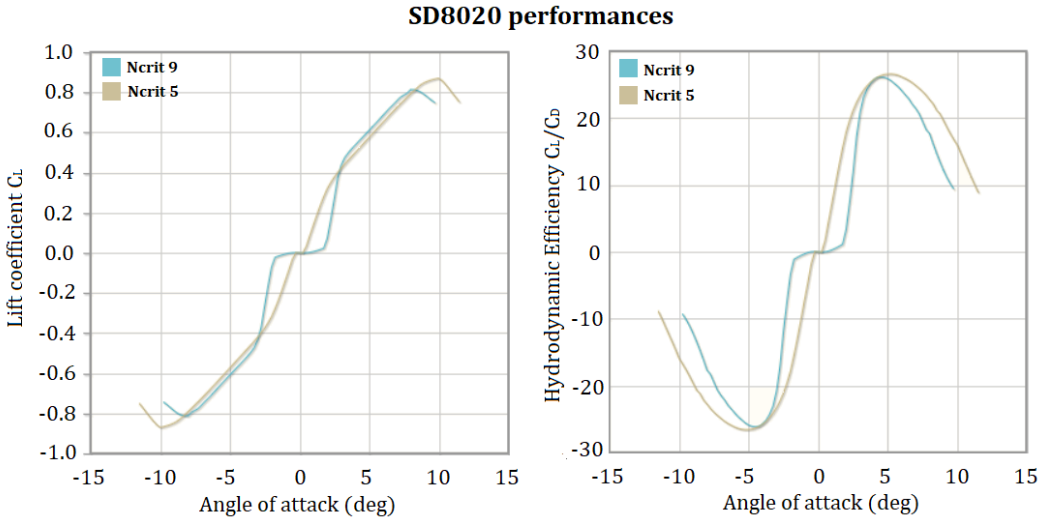

Figure 4.8: CL vs α and CL/CD vs α for and SD8020 airfoil at Ncrit 5 and 9.

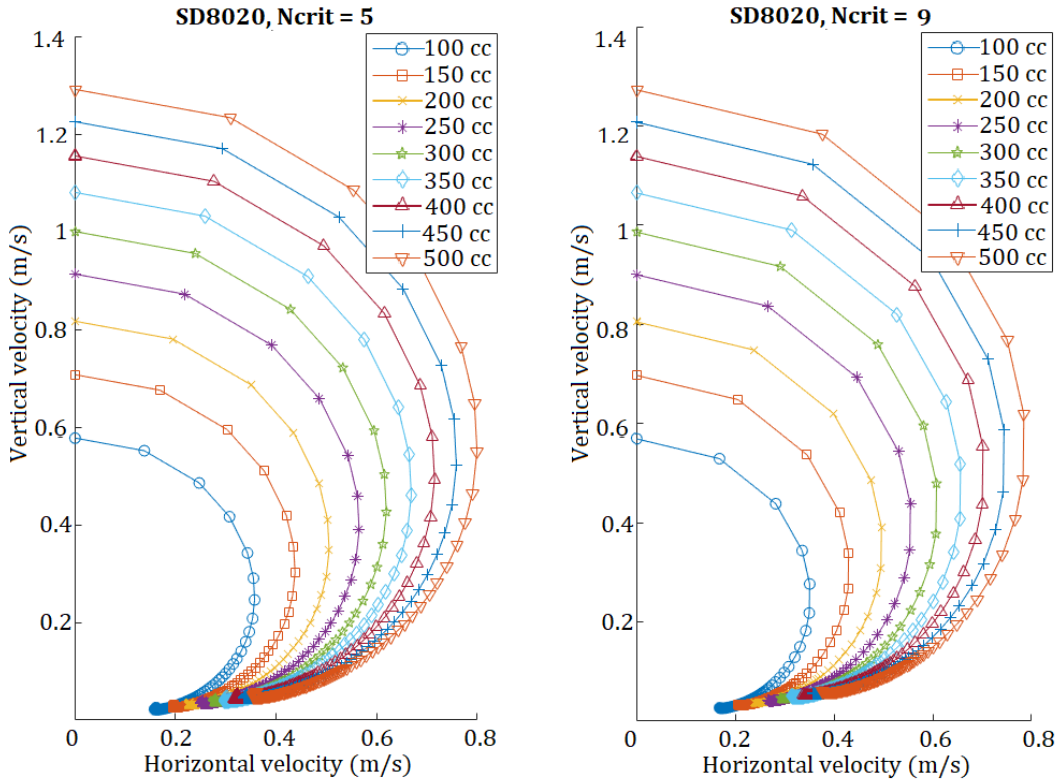

Figure 4.9: Differences between velocity polars for the SD8020 at Ncrit 5 (left) and Ncrit 9 (right). Each marked point of the curves notes an increase in angle of attack of 0.1°.

Ultimately, the Ishii airfoil was picked, also at a higher roughness (Ncrit = 5).

In the next paragraph, the optimization process will be done on the Ishii and SD8020 wings, to see how an asymmetric and a symmetric solution compare in performances. It must also be noted that besides the fact that the model is relatively simple, some additional approximations have been made. First of all, the induced lift slope reduction makes the assumption that the 2D $CL - \alpha$ slope is equal to 2π, although this is particularly inaccurate at low Reynolds numbers. Secondly, the Oswald coefficient was assumed to be 0.9, since the planform was not yet designed in detail. At the end of the design process these aspects will be reevaluated to see if they significantly change the final results. Also, the total wing surface was calculated without including the portion taken by the hull and without considering the increase in lift near the wing root caused by its presence. So while at least the ideal airfoil will be found, the planform is still far from being defined after these first very approximated calculations.

4.6 Airfoil optimization

The optimization of the airfoils will be done through XOptFoil. This software works in parallel to xFoil and is fairly straightforward to use. All it requires is to compile a configuration file which contains all the details on desired optimization methods, fitness function, operation points, geometrical and moment constraints. Once this is done, XOptFoil just needs to be run through the command line, and after a pre-defined number of iterations it will save the coordinates of the airfoil with the best fitness function. Following, the main aspects of the configuration file will be discussed in order to understand an ideal optimization for each of the airfoils considered.

-**Search type:** two main categories are distinguished: a global search and a local search. The global search looks for solutions which might be quite different from the original airfoil through methods such as particle swarm or the genetic algorithm. These methods are generally more expensive but also more likely to find a better solution, although they are not guaranteed to find the "best" one. Local methods, such as gradient methods, only try to improve the current airfoil without looking for solutions particularly different from it. They can be particularly useful if somehow the designer knows that his airfoil is close to being the best possible. In general, for both the SD8020 and the Ishii airfoils, a global and local search will be made, in which the gradient method will only be used at the end to further optimize the solution found by either the particle swarm or the genetic algorithm.

-**Global search:** both the genetic algorithm and the particle swarm are valid methods, both capable of achieving a perfect optimization in very large domains, but according to several studies[9][10[11] the particle swarm is slightly more efficient and has a higher likelihood of reaching the absolute optimal solution, so this will be the method of choice.

-**Local search:** the only local method at disposal of XOptFoil is the Simplex method and therefore will be the one of choice.

-**Shape functions:** in general, when designing a new airfoil, it is useful to have some parametrization criteria. But when a seed airfoil is already provided, its geometry can be modified with the Hicks-Henne bump functions. When the x-y coordinates of the original airfoil are provided, the coordinates of the new one can be changed in

$$y_{new} = y_{OG} + \sum_{i=0}^{n} a_i \, \varphi_i(x) \tag{4.12}$$

where

$$\varphi_i(x) = sin^{ti}(\pi \, x^{m_i)} \tag{4.13}$$

and

$$m_i = \frac{log(0.5)}{log(x_{Mi})} \tag{4.14}$$

x_{Mi} being the location in which the modification is most prominent. In total, 6 Hicks-Henne bump functions will be used for the top and the bottom of the airfoils.

-**Operating points:** These define the flight conditions at which the optimization takes place. It is possible to specify the lift coefficient or the angle of attack (in this case it will be the former, since it was already determined in the previous paragraph), the goal of the optimization, such as minimizing drag, maximizing glide, minimizing the sink rate, delaying the boundary layer transition or maximizing the lift slope. For the purposes of this project, the first three will be equivalent when the lift coefficient is specified, and the maximization of glide will be selected. The Reynolds and Mach numbers are also specified for each point. Finally, in case multiple operating points are defined, a relative weight on the fitness function can be attributed to each one. For both airfoils, an optimization will be made at the same C_L but at different Reynolds numbers, to take into consideration the varying temperatures of the ocean as a function of depth. Some additional points will also be added at other lift coefficients to avoid an excessively specialized and therefore not versatile airfoil. This is going to be particularly important for the SD8020.

-**Geometrical constraints:** The most important ones revolve around airfoil thickness and trailing edge angles. While a maximum is usually not required, a minimum is usually set for structural reasons. In this case, since the loads are very small, no minimum values will be set initially. Another number to fix is the maximum number of curve reversals on each surface of the airfoil. Initially, two will be allowed for the top and bottom surfaces. Not posing this constraint may give benefits to the fitness function, but might also generate "bizarre" geometries which may be excessively specialized, with odd behaviors or that might exploit minor bugs is xFoil's code. Of course, in the case of the the SD8020, a symmetric constraint will also be imposed. Also, no moment constraint will be set to neither of the airfoils, since in this case it will have a very small effect on the longitudinal stability of the glider.

-**Initialization:** For global searches, initially a population of airfoils will be generated. If some of the generated airfoils violate the constraints, they will be given an objective function penalty which surpasses the feasibility limit (by default the penalty is of 10^6, while the feasibility limit is of 50.000). If a design is not feasible, it will be modified for a number of times to make it so. The number of attempts is normally set at 1000, and usually needs to be increased only if there are tight design constraints.

-**Particle swarm:** It is useful to describe the particle swarm optimization

(PSO) before defining its main parameters. It is a metaheuristic method that is apt to find a solution in particularly large and continuous search spaces, and was originally inspired by the movement of insect and bird swarms. In this method, a set of possible solutions, referred to as particles, are initially randomly distributed in the search space and given an assigned position $x_{i,0}$ and velocity $v_{i,0}$. They will all have an assigned value of the fitness function dependent on their position. At every iteration they will move and their new position will be

$$x_{i,t+1} = x_{i,t} + v_{i,t}\Delta t \tag{4.15}$$

with

$$v_{i,t} = r_1\, v_{i,t-1} + r_2\frac{(P_g - x_{i,t})}{\Delta t} + r_3\frac{(P_a - x_{i,t})}{\Delta t} \tag{4.16}$$

where r_1, r_2, r_3 are random coefficients comprised between 0 and 1, Δt is the fictitious time step between each iteration, P_g is the position of the best particle in the previous iteration, and P_a is the best overall particle. On XOptFoil it is possible to select the desired number of particles, the radius of the search space in which all of the particles must be in order to trigger a stop condition, the maximum number of iterations and the "exhaustive" or "quick" searches. The number of particles will be proportional to the computational cost, but a higher number will have better odds of reaching the optimal solution. For the airfoil problem, in general a good number is 50 particles. The minimum radius will generally not be too relevant, since in the exhaustive search (the one used in these experiments) the stop condition will almost always be triggered by reaching the maximum number of iterations (by default set at 700, value after which it will be hard for the solution to improve significantly).

For both the SD8020 and the Ishii airfoils, 700 iterations were more than enough to find what can be assumed to be an optimal solution. In figures 4.10 and 4.11 are portrayed the profiles of the new optimized airfoils. The optimized SD8020 airfoil has a maximum thickness of 9.6% at 25.9% of the chord and null camber, while the optimized Ishii airfoil has a maximum thickness of 4.4% at 16.9% of the chord and a maximum camber of 2.9% at 46% of the chord. Of course there is no certainty that the optimization actually converged, but no improvements were found after the 148th iteration for the SD8020 and after the 453rd iteration for the Ishii, leading to the conclusion that if there can be further improvements, these will be minimal most likely. An improvement of 8.54% to the fitness function was attained for the symmetrical airfoil and one of 18.38% was attained for the Ishii. The Lift/Drag coefficient curves will be portrayed in figures 4.12 and 4.13. Additionally, even if it is not taken into consideration for the hydrodynamic design of the glider, the moment coefficient is plotted in figure 4.14 as a function of the angle of attack.

This is because it will be necessary for an eventual control design, even though this topic will not be treated in this work.

Even at the end of the optimization process, the performances of the Ishii airfoil are noticeably superior to those of the SD8020, and therefore from now on the design of the wing will continue without taking into consideration any symmetry constraints, as it will be noticed throughout the planform optimization process.

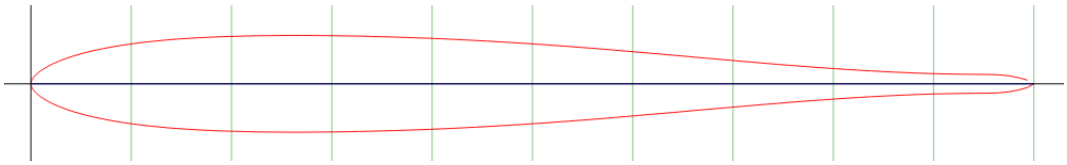

Figure 4.10: Profile of the optimized SD8020 airfoil.

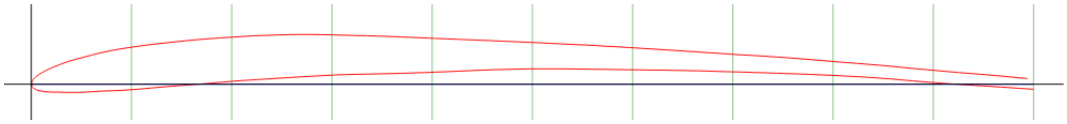

Figure 4.11: Profile of the optimized Ishii airfoil.

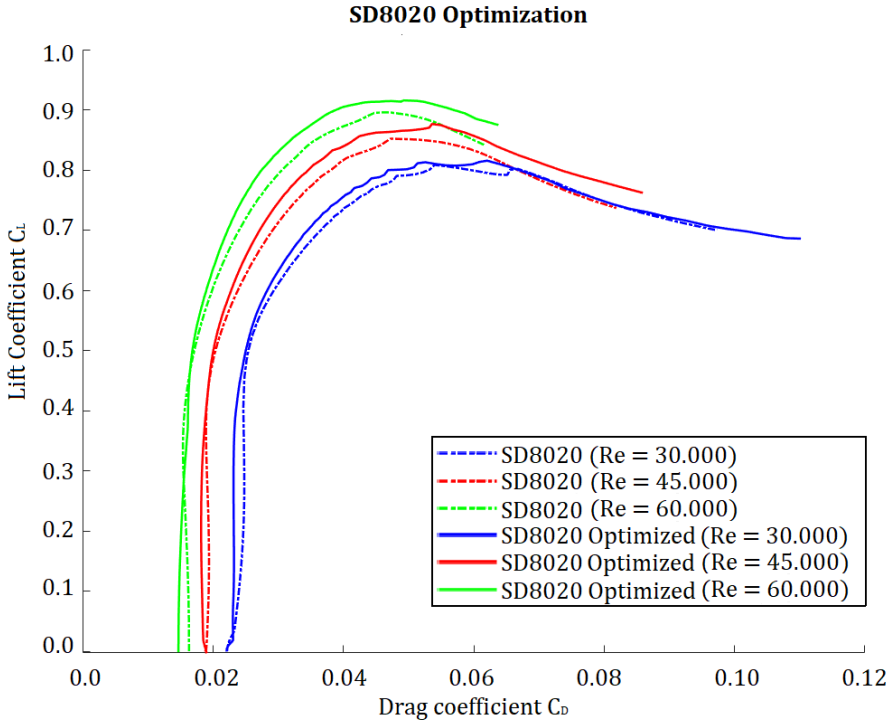

Figure 4.12: Lift and drag coefficient curves for the SD8020 and its optimized version at Reynolds numbers of 30.000, 45.000, 65.000.

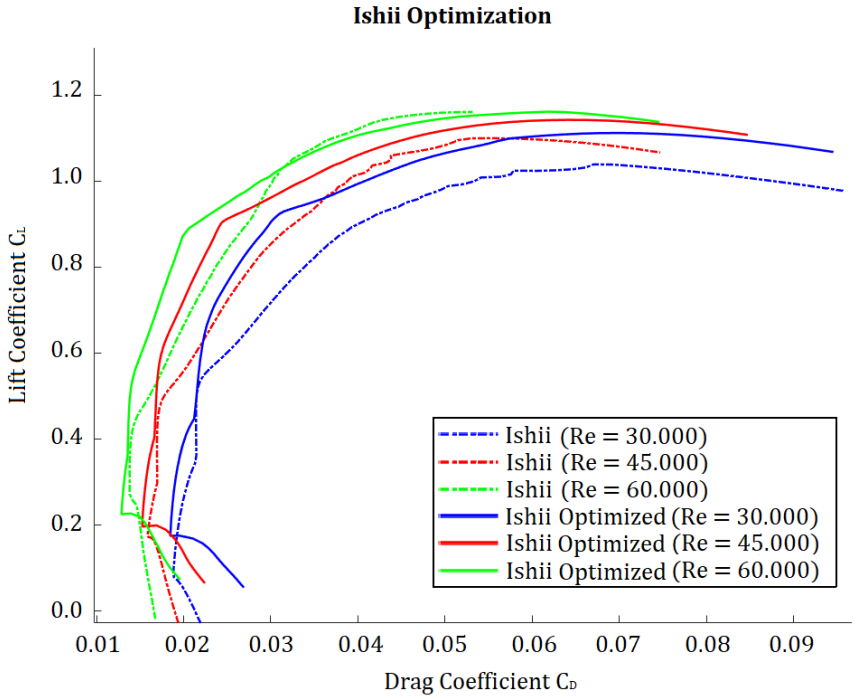

Figure 4.13: Lift and drag coefficient curves for the Ishii and its optimized version at Reynolds numbers of 30.000, 45.000, 65.000.

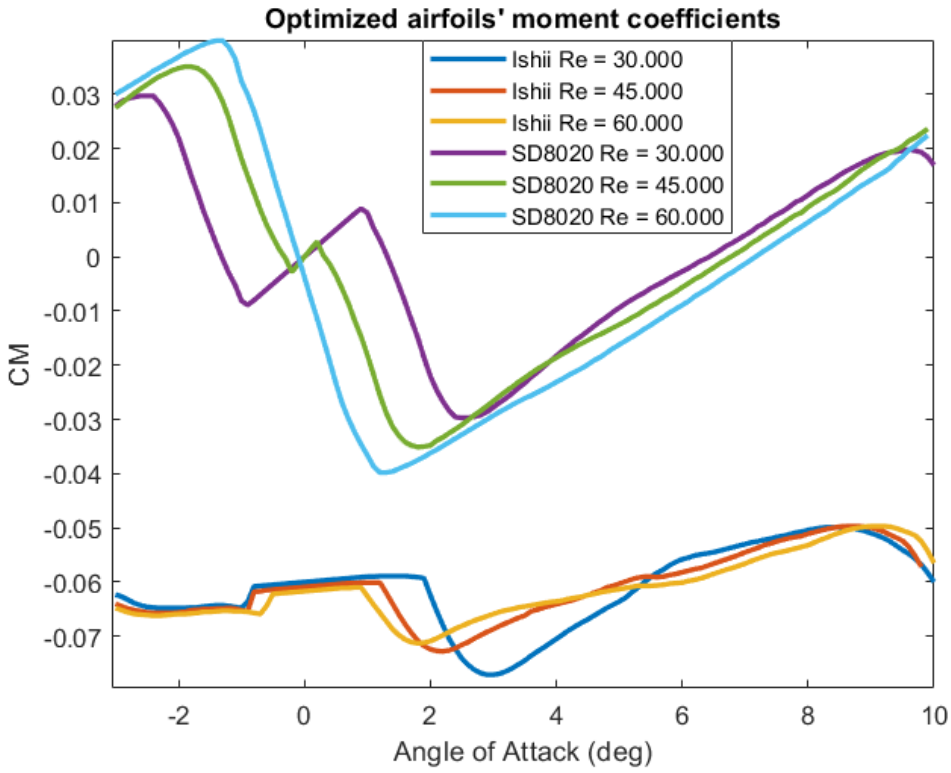

Figure 4.14: Moment coefficient curves for the optimized SD8020 and Ishii airfoils at Reynolds numbers of 30.000, 45.000, 65.000.

4.7 Planform optimization

4.7.1 Athena Vortex Lattice

To design the planform, the software AVL (Athena Vortex Lattice) was used. Its code was originally written by Harold Youngren and later modified by Mark Drela. As the name suggests, it uses a vortex lattice method, a type of panel method which is essentially an extension of Prandtl's lifting line theory, but where the wing, instead of being modelled as a line with an infinite number of horseshoe vortices, is discretized in a finite number of 2D elements, or panels, each being assigned a vortex and a control point, on which the perturbation velocity is calculated as a sum of the contributions of all the other vortices. AVL, being a panel method, is limited in scope, as it is only applicable in the case of incompressible flows, steady or quasi-steady flows and configurations which consist of mainly thin lifting surfaces at small angles of attack and sideslip. In the case of an AUG though, none of these limitations are significant, making a panel method a more convenient tool than CFD, at least in the first design phases, as it requires an exponentially lower computational effort.

A wing geometry can be described on AVL by writing on a specific format in a basic text file. A series of points belonging to the leading edge must be defined, by specifying their coordinates. For each point, the length of the chord and twist angle are defined. The rest of the geometry is defined through linear interpolation between the defined points, so the more of these are defined, the smoother the wing's lines will be. Once the geometry file is written, it is possible to study the performances of the lifting surface. The interface of AVL is quite similar to that of xFoil. In the case of the project at hand, the main interest is to evaluate the planform's effect on induced drag. Another aspect that is often of interest is the evaluation of the static margin and its overall effect on the longitudinal stability of the aero/hydrodynamic body at hand. In the case of an AUG though, it is possible to neglect it, since the hydrodynamic lift of the wing will be less than 1% of the weight and buoyancy forces, so even its moment will have a very minor effect on the overall stability of the glider, which will mostly be affected by the position of its gravitational center.

4.7.2 Initial wing setup and optimization

It is necessary to define an initial wing shape to start off the optimization process. In order to do so, five points were defined along the wingspan. One at the root, one at the tip and three more in between, concentrated more towards the tip, where the largest geometrical gradients are normally present. For each of

these points, it was allowed to change the chord length, the incidence angle, and the x and z coordinates in order to modify the planform. The wingspan was made to be equal to 1.01 m in length, which was previously estimated to be an optimal value. It is important to constrain this value, since AVL doesn't take into account the effect of the Reynolds number on the 2D performances of the airfoil, so the optimization code, which only aims at minimizing induced drag, would therefore tend to make extremely wide wingspans. The wing is tapered between each section in order to have a pseudo-elliptical load distribution, with a sweep angle of 14° at the leading edge and a null sweep at the trailing edge, dictated mostly by the observations on the SeaGlider's design. In the initial configuration, no dihedral angle and no twist angles are present in any area of the wing. In figure 4.15 is a visual representation of the initial configuration.

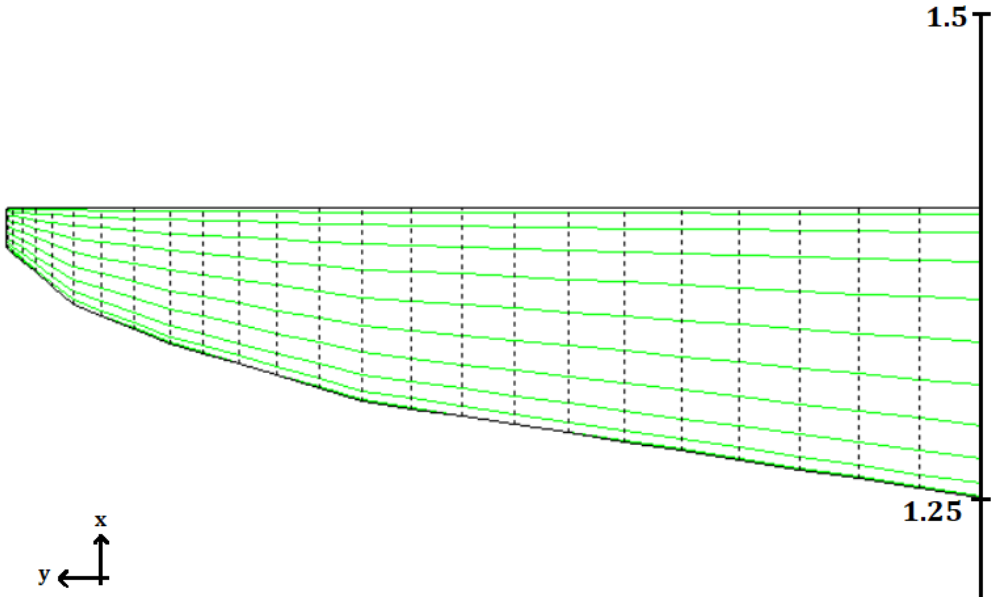

Figure 4.15: View from above of the initial wing configuration modeled on AVL.

A source of doubt was the approach to adopt when defining the root of the wing. To calculate induced drag on AVL (or any other vortex lattice software), even if there is a fuselage, the two wings of any aircraft or watercraft must be connected, otherwise the software will calculate vortices even at the roots of the wings. In general this means that there will be an extra strip of surface in place of the fuselage, which will provide an increment in lift, which is not present in reality. This is usually not a big problem, because in reality, the presence of a fuselage generates a flow acceleration near the wing root, which mostly compensates the lack of lift generated by the fuselage. But most aircraft have a fuselage diameter which is much smaller than the wingspan, while in the case of the AUG to be designed the hull's diameter is 25% of the total wingspan, so replacing the hull with extra

wing surface might generate excessively inaccurate results. AVL though allows to also create slender bodies of revolution such as fuselages and models them with sources and doublets. According to AVL's documentation, the resulting dynamics are consistent with slender body theory, but there is limited experience with such models, and therefore this functionality should be used with caution. Therefore, the optimization process was done with and without the fuselage modeling on AVL, to see if any significant differences in results would occur. In figure 4.16 the same wing of figure 4.15 is shown, but with the hull modeled in. The leading edge of the root of the wing is located at the point of maximum diameter of the hull. This decision wasn't really dependent on hydrodynamic stability, but rather on the need to minimize chances of disruption of the hull's laminar flow.

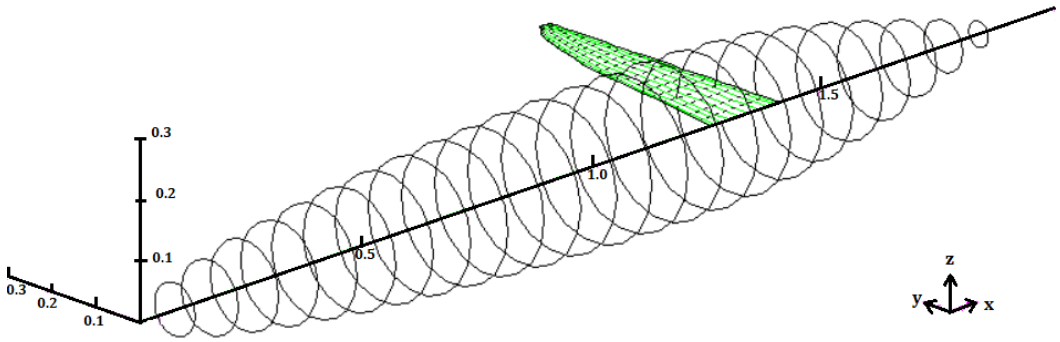

Figure 4.16: Wing and hull as modeled on AVL.

The optimization process was achieved with a series of Python scripts. One script is to control the interface of AVL and automatize it, one is to define the optimization constraints, which blocked the planform surface, and made it so that the chord and the incidence angle at the tip are smaller than those at the root of the wing, besides posing an upper and lower limit to all of the optimization variables. Another script was to define the fitness function and calculate it along with its Jacobian matrix. The fitness function is simply the induced drag evaluated with Trefftz's method, at three different lift coefficients: 0.3, 0.55 and 0.7, with the second having twice the weight on the fitness function as the other two. Finally, in the main script, the type of optimization is defined and executed. The one chosen is that of differential evolution. This, just like particle swarm, is a metaheuristic method. It is based on natural evolution, where a series of initial designs is selected and then "procreates". For each generation only the configurations with the best fitness function will keep procreating, simulating the phenomenon of survival of the fittest. This method was chosen over particle swarm because of its easier implementation on Python. Specific parameters for this method are:

- **Strategy**: in this case it is the so called "best1bin", meaning that the

mutations come from only the current best vector of variables and have a uniform crossover (bin stands for binomial distribution).

- **Iterations**: This defines the maximum number of iterations before the algorithm automatically stops. In this case it was posed at 500.

- **Population size multiplier**: This is a multiplier to set the total number of individuals in the population, which will multiply the number of optimization variables. This number was set at 15.

- **Tolerance**: This is the relative tolerance for convergence, which stops the optimization process once it is reached.

- **Mutation**: This value specifies how much each generation can change. In the SciPy documentation it is advised to keep it between 0 and 2, and its main effect is on the convergence velocity and on the stability of the optimization process. In this case it was set at 0.5.

- **Recombination**: Set between 0 and 1, this represents the crossover probability from each generation. Just as the mutation parameter, it mainly affects the convergence speed and evolution stability. Its value was set at 0.7.

At the end of each iteration, the best individual is "polished" with a local optimization.

4.7.3 Planform optimization results

As previously mentioned, two optimization cycles were executed, one for the configuration with the hull and one for the configuration without the hull. Although different, the two wings obtained had some similarities. In the hull-lacking configuration, when viewed from the top, there is a shape more similar to a crescent moon, while the other has a straighter swept wing. Both have winglets of similar dimensions. A small difference is in the twist angle at the tip, which is a little more pronounced in the hull lacking configuration. In table 4.4 The main wing characteristics are displayed. The wings' planforms are shown in figures 4.17 and 4.18. The crescent-moon shaped wing is not surprising, despite it not being very common, as there are studies[12] which show that such a shape can help with reducing induced drag, making it even lower than a classical unswept wing with elliptical load distribution. In order to choose one of the planforms, their overall performances must be observed. Since the presence of the hull can alter the final results, both configurations are analyzed with and without the addition of the hull in AVL. The graph in figure 4.19 shows that the overall differences in induced drag are nearly negligible. It can be noticed though, as one would expect, that the crescent wing has slightly better performances than the swept wing when the hull isn't considered, while the opposite is true when the hull is included in

the calculations. This can suggest that the optimization process was conducted properly. Additionally, it can be of interest to notice that including the hull in AVL's calculations leads to more pessimistic predictions at low lift coefficients, but more optimistic predictions at higher lift coefficients. In a practical scenario, such small differences in performance would not be the determining factor in the choice of the best wing planform, ultimately it would most likely come down to which one is more structurally stable and is easier to build. Additionally though, it should be reminded again that the Reynolds number has a significant effect on the airfoil performances, so it would be best to pick a wing with chords that do not become too small at the tip. For this reason the crescent wing will be the one of choice, besides having more of a negative twist angle, meaning that it will be harder for the wing tips to stall. In fact, it must be noted that AVL is not taking into account the airfoil's characteristics and simply considers them thin airfoils, allowing to set only a constant ratio between their lift coefficient and angle of attack. Therefore it is completely unaware of any stall phenomena which might occur, which can be a particularly critical aspect even because the Ishii airfoils, as most low Reynolds airfoils, have a fairly low lift coefficient peak.

Planform geometry		
Configuration	**Swept wing**	**Crescent wing**
Surface	0.11 m^2	1.86 m^2
Wingspan	1.01 m	1.01 m
Chord root	0.130 m	0.135 m
Chord tip	0.053 m	0.068 m
Sweep angle LE	15.7°	13.5°
Sweep angle TE	10.8°	4.7° m
Dihedral angle	0.0°	0.0°
Twist angle	−4.1°	−5.2°
Winglet height	0.065 m	0.069 m

Table 4.4: Wing planform characteristics with and without consideration of the hull during the optimization process.

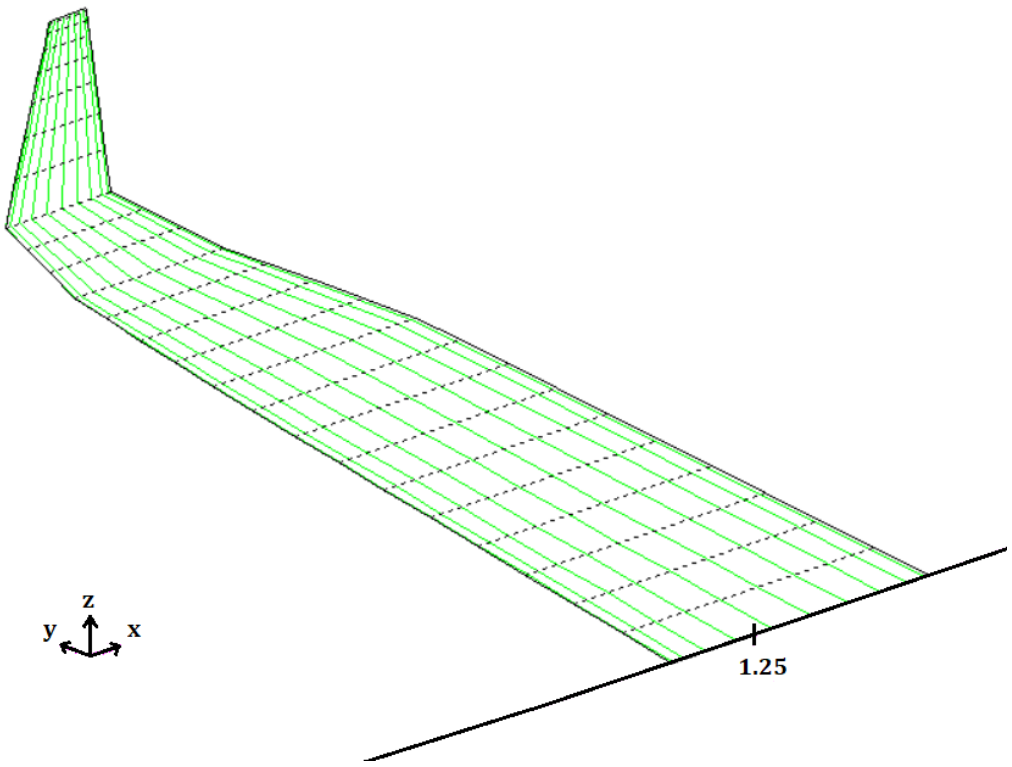

Figure 4.17: Isometric projection of the swept wing variant.

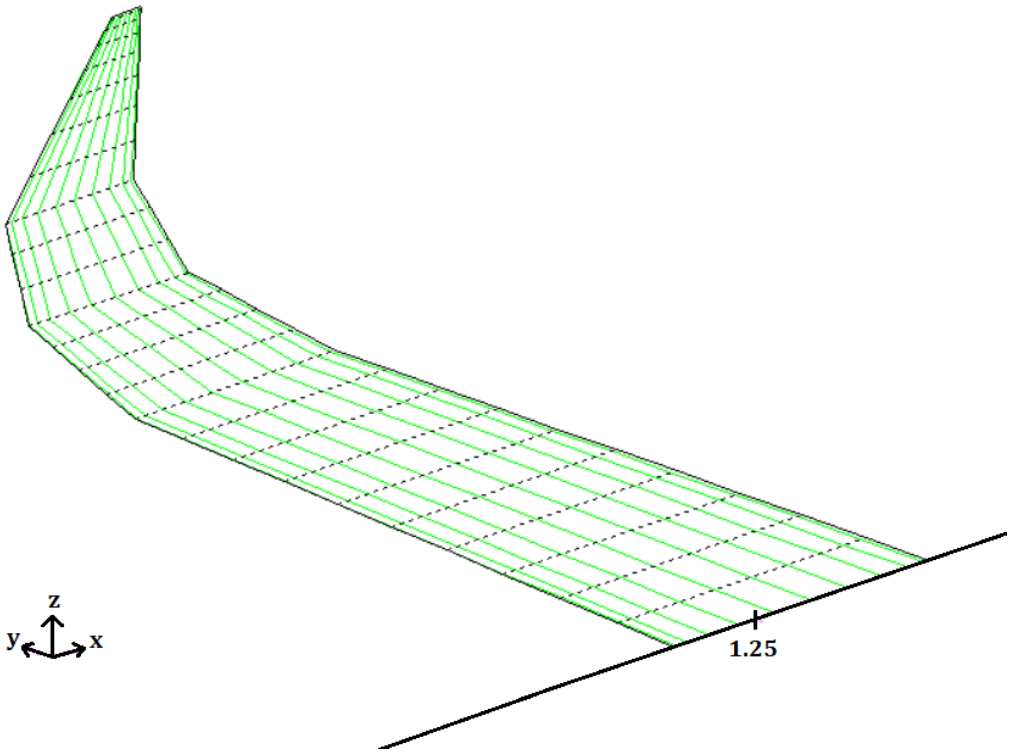

Figure 4.18: Isometric projection of the crescent wing variant.

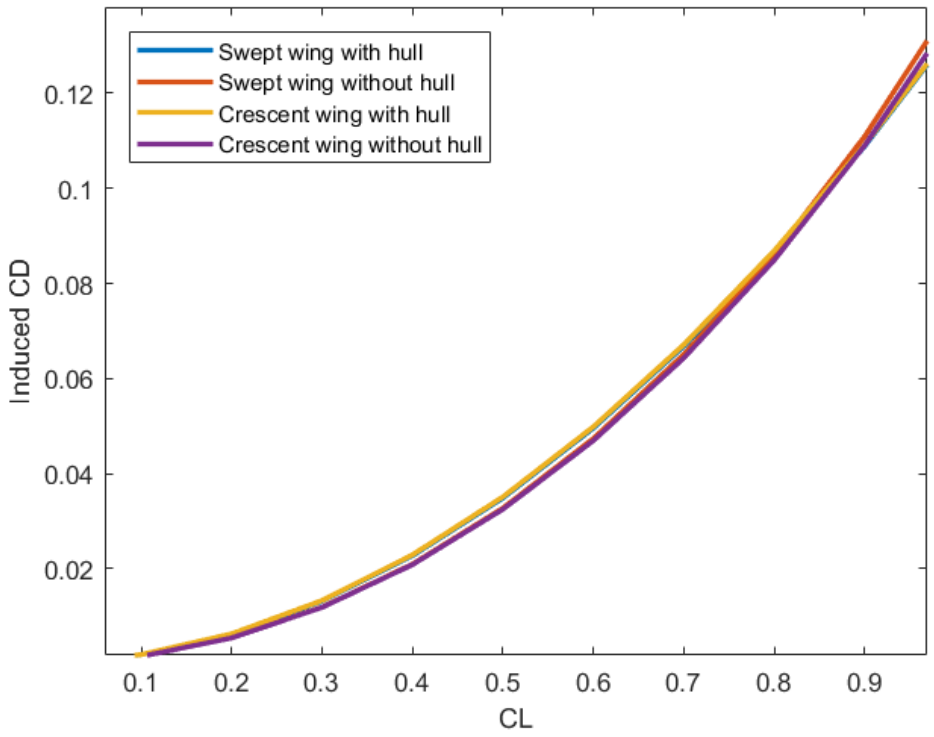

Figure 4.19: Induced drag coefficient comparison as a function of lift coefficient.

4.8 Final design and results

To have a good idea of the overall wing performances, as mentioned before, a 3D CFD simulation would be ideal. Besides the high computational cost though, another problem is brought by the difficulty of designing a 3D structured mesh for a wing with variable sweep and twist angles and a winglet. So in this case the performances of the wing will be estimated by evaluating profile drag and induced drag as a function of CL and summing them. Of course this does not take into account the more complex interactions that occur when considering a three-dimensional flow, but it will still provide a good idea of the wing's performances. So the total drag coefficient will be calculated as

$$C_D(C_L) = C_{D_{2D}}(C_L) + C_{D_{ind}}(C_L) \tag{4.17}$$

In Figures 4.20 and 4.21 are graphs reporting the wing's total drag coefficient and efficiency against its lift coefficient. Although the data might seem too optimistic, it is necessary to remember that this doesn't factor the hull's drag, estimated in the previous chapter at a null angle of attack, and eventual interference drag, which can only be computed through CFD and wind tunnel experiments.

It is not surprising that for lower Reynolds numbers the wing has worse per-

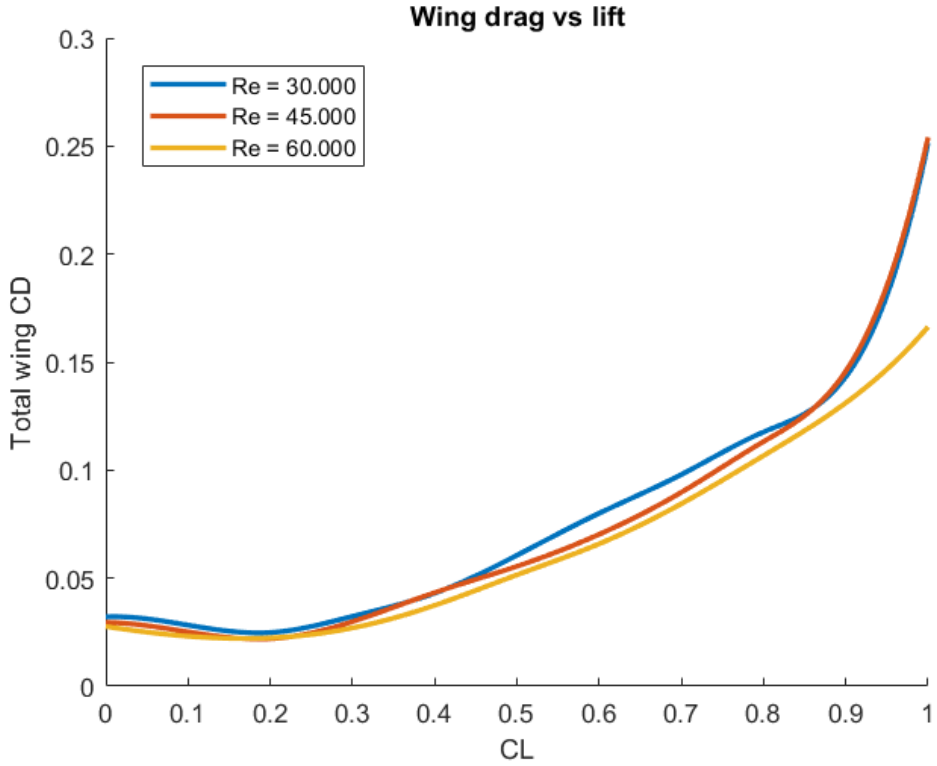

Figure 4.20: Wing's estimated total drag coefficient plotted against the lift coefficient.

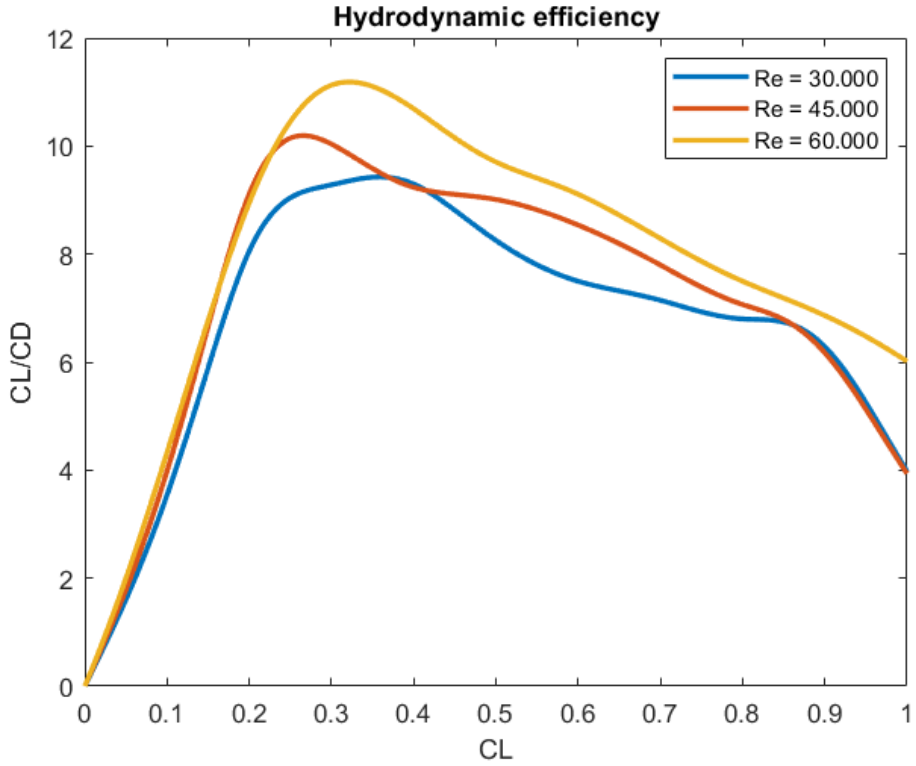

Figure 4.21: Wing's estimated efficiency plotted against the lift coefficient.

formances, but it is notable that these do not drop dramatically. The only spot where there are significant drops in performances are for lift coefficients above 0.8, where at Reynolds of 45.000 and lower the airfoil is close to stalling. The peaks in performances also vary as a function of Re but are at lift coefficients between 0.27 and 0.4.

In figure 4.22 is a 3D representation of the wings, mounted on the hull. As a summary of the overall performances of the glider, figure 4.23 shows the estimated velocity curves of the final hull concept, in similar fashion to figure 4.9. The velocity components give an indication of the hydrodynamic efficiency of the model.

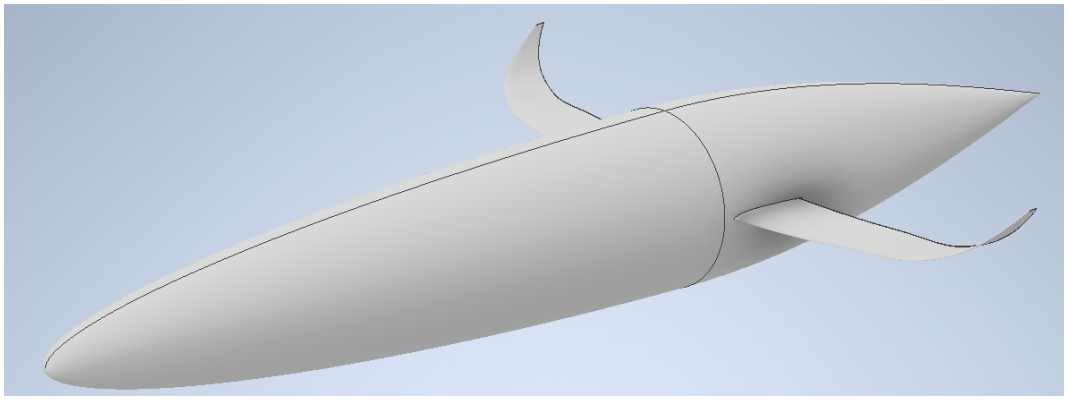

Figure 4.22: 3D representation of the wing-hull assembly.

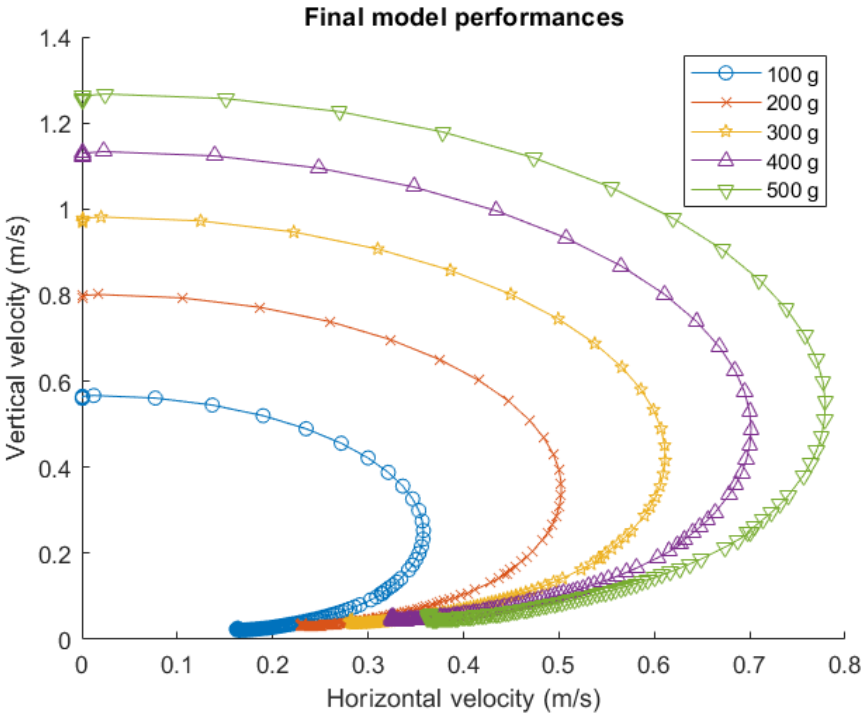

Figure 4.23: 3D representation of the wing-hull assembly.

Chapter Bibliography

[1]Justin Winslow, Hikaru Otsuka, Bharath Govindarajan, Inderjit Chopra, 2018, *Basic Understanding of Airfoil Characteristics at Low Reynolds Numbers*, Journal of Aircraft, Vol.55, No.3, DOI: 10.2514/1.C034415

[2] Christopher James Hockley, 2018, *Improving Seaglider Efficiency: An Analysis of Wing Shapes, Hull Morphologies, and Propulsion Methods*, Thesis at Embry Riddle Aeronautical University.

[3] Lucas Merckelbach, Gwyn Griffiths, David Smeed, 2010, *Vertical Water Velocities from Underwater Gliders*, Journal of Atmospheric and Oceanic Technology, DOI: 10.1175/2009JTECHO710.1

[4] Joshua Grady Graver, 2005, *Underwater gliders: Dynamics, Control and Design*, pag. 31, Thesis at Princeton University.

[5] William P. Barker, 2012, *An Analysis of Undersea Glider Architectures and an Assessment of Undersea Glider Integration into Undersea Applications*, Thesis at Naval Postgraduate School of Monterey.

[6] Michael S. Selig, James J. Guglielmo, Andy P. Broeren, Philippe Griguère, 1995, *Summary of Low-Speed Airfoil Data*, ISBN 0-9646747-1-8

[7] http://airfoiltools.com/airfoil/details?airfoil=hq159-il

http://airfoiltools.com/airfoil/details?airfoil=hor07-il

[8] Masayuki Anyoji, Daiki Hamada, 2019, *High-performance airfoil with low reynolds-number dependence on aerodynamic characteristics*, Flow Mechanics Research International Journal, Vol. 3, Issue 2, DOI: 10.15406/fmrij.2019.03.00055

[9] F. D. Wihartiko1, H. Wijayanti, F. Virgantari, 2018, *Performance comparison of genetic algorithms and particle swarm optimization for model integer programming bus timetabling problem*, IOP Conference Series: Materials Science and Engineering 332 012020, DOI:10.1088/1757-899X/332/1/012020

[10] Shahid Shabir, Ruchi Singla, 2016, *A Comparative Study of Genetic Algorithm and the Particle Swarm Optimization*, International Journal of Electrical Engineering, ISSN 0974-2158 Vol. 9, No. 2, DOI: 10.1109/CEC48606.2020.9185497

[11] Sidhartha Panda Narayana, Prasad Padhy, 2008, *Comparison of particle swarm optimization and genetic algorithm for FACTS-based controller design*, Applied Soft Computing, Vol. 8, Issue 4, DOI: 10.1016/j.asoc.2007.10.009

[12] C.P. van Dam, 1987, *Induced-Drag Characteristics of Crescent Moon Shaped Wings*, Journal of Aircraft, Vol. 24, No. 2, DOI: 10.2514/3.45427

Chapter 5

CFD: Simulations and Results

In the previous chapters a concept model of the hydrodynamic surfaces was developed, but this is generally not the final step in the design of any hydrodynamic or aerodynamic surface. Some type of simulation must be done in order to understand the accuracy of the predictions of the model's performances. In general there are two possible paths to do so: computational fluid dynamics and experimental fluid dynamics. Both of these methods have their advantages and disadvantages, and whether one of them is better than the other is still a highly contended dispute. Computational fluid dynamics only require computers to solve problems that involve fluid flows, along with any CFD software. Whether the software is free of charge or for sale, the codes used by the solvers are nearly identical, with the main difference being the difficulty of their use. Experimental fluid dynamics simulations are done in a wind tunnel. These can replicate accurately the flow conditions but require a model to be built and access to a wind tunnel, along with specialized technicians. Additionally, this method may also be subject to errors or inaccuracies during the assembly of the system, such as inexact angles of attack. For this project, CFD will be employed, through the software SU2, as it requires less instruments and provides extensive data of the whole flow's domain with just one simulation. This does not mean that wind tunnel experiments are superfluous and in fact they should always be performed when possible.

The least demanding simulations and the ones that need the most monitoring will be performed on a simple laptop with an Intel Core i7 processor, a CPU at 2 GHz and a RAM memory of 16 GB. More demanding computations, such as the ones on the 3D hull geometries, will be performed on Politecnico di Milano's HPC cluster, a system in which up to thousands of computers can work in parallel in order to solve larger problems[1], although in this case no more than 20 cores at a time will be used.

Chapter Symbology

a	Constant used in Spalart-Allmaras turbulence model
f	Body force
k	Turbulent energy
p	Pressure
u	Local velocity
x	Position vector
y	Physical distance from the wall
y^+	Adimensionalized distance from the wall
AoA	Angle of attack
C_μ	Constant used in the $k-\omega$ SST and Spalart-Allmaras model to relate ω and ε
C_f	Skin friction coefficient
C_D	Drag coefficient
C_L	Lift coefficient
C_p	Pressure coefficient
F_1	Blending function used in the $k-\omega$ SST model
I	Turbulence intensity
P_k	Production term due to mean velocity shear in k transport equation
Re	Reynolds number
U	Free-stream velocity
β	Constant used in $k-\omega$ SST turbulence model
γ	Constant used in $k-\omega$ SST turbulence model
δ_{ij}	Kronecker's delta
ε	Turbulent energy dissipation rate
μ	Dynamic viscosity coefficient
μ_t	Fictitious dynamic viscosity coefficient due to turbulence
ν_t	Eddy viscosity
ρ	Density
$\sigma_{\omega 2}$	Constant used in the $k-\omega$ SST model
τ_w	Shear stress at the wall
ω	Specific rate of turbulence dissipation
i, j, x, y, z	Subscripts to indicate the direction of the vectors
$\bar{}$	Symbol to indicate the mean value of a variable in a Reynolds averaged flow
$'$	Symbol to indicate the fluctuations from from the mean value of a variable in a Reynolds averaged flow

5.1 Brief parenthesis on turbulence modeling

Before describing the simulations and their results, it is best to describe in very broad terms how turbulence is embedded in CFD codes and how it is resolved, as having an awareness of it is fundamental to understand what turbulence model is best to use and what kind of results can be expected. For this project, the prediction of flow transition is especially important, as it will have sizeable effects on the hull's drag and the wings' efficiency at varying Reynolds numbers.

The unfortunate aspect of turbulence is that it is an extremely difficult phenomenon to predict, being almost a completely random process subject to chaos and extremely variable for even slightly different boundary conditions. Simulating all the eddies that form in a flow is unthinkable for normal CFD codes and would require extremely fine meshes. Although there are currently developments with DNS (Direct Numerical Simulation), for practical uses and designs this would not be an option.

To get around this problem, in general, CFD codes resolve the RANS equations (Reynolds Averaged Navier Stokes), by dividing the velocity terms into their average plus their fluctuations in time, i.e.

$$u(x,t) = \bar{u}(x) + u'(x,t)$$

which leads to a new formulation of the Navier Stokes momentum equations:

$$\rho\bar{u_j}\frac{\partial\bar{u_i}}{\partial x_j} = \rho\bar{f_i} + \frac{\partial}{\partial x_j}\left[-\bar{p}\delta_{ij} + \mu\left(\frac{\partial\bar{u_i}}{\partial x_j} + \frac{\partial\bar{u_j}}{\partial x_i}\right) - \rho\overline{u_i'u_j'}\right] \tag{5.1}$$

The last term, $-\rho\overline{u_i'u_j'}$, is the so called Reynolds stress tensor, which presents six unknown terms, as the velocity fluctuations aren't prescribed and depend on turbulence. Therefore, in order to close the problem, there are several turbulence models which try to consider some of its effects, but without a proper physical description of the phenomenon. Some turbulence models may not use any transport differential equations, and only make use of algebraic relations, but these generally produce inaccurate solutions, as they don't take into consideration convection or diffusion of turbulence, making it a static phenomenon.

A widely used hypothesis is the one by Boussinesq, which expresses the Reynolds stresses with a linear dependency to a fictional turbulent viscosity, as in:

$$-\rho\overline{u_i'u_j'} = \mu_t\left(\frac{\partial u_i}{\partial x_j} + \frac{\partial u_j}{\partial x_i} - \frac{2}{3}\frac{\partial u_k}{\partial x_k}\delta_{ij}\right) - \frac{2}{3}k\delta_{ij} \tag{5.2}$$

which by itself isn't enough to close the RANS equations, as μ_t and k are also un-

known and variable. Therefore at least two more equations, algebraic or differential, must be elaborated.

The most common model used for CFD codes nowadays is the $k-\omega$ SST, which uses two transport equations, one for the turbulent energy k and one for the specific rate of turbulence dissipation ω, which is algebraically related to ε, the rate of turbulence dissipation.

$$\frac{\partial}{\partial t}(\rho k) + \frac{\partial}{\partial x_i}(\rho k u_i) = \frac{\partial}{\partial x_j}\left[\left(\mu + \frac{\mu_t}{\sigma_k}\right)\frac{\partial k}{\partial x_j}\right] + P_k - \rho\varepsilon \tag{5.3}$$

$$\frac{\partial}{\partial t}(\rho\omega)+\frac{\partial}{\partial x_i}(\rho\omega u_i) = \frac{\partial}{\partial x_j}\left[\left(\mu + \frac{\mu_t}{\sigma_\varepsilon}\right)\frac{\partial \omega}{\partial x_j}\right]+\frac{\gamma}{\nu_t}P_k-\beta\rho\omega^2+2(1-F_1)\frac{\rho\sigma_{\omega 2}}{\omega}\frac{\partial k}{\partial x_i}\frac{\partial \omega}{\partial x_i} \tag{5.4}$$

$$\omega = \frac{\varepsilon}{C_\mu k} \tag{5.5}$$

This model was born as an improvement over the $k-\varepsilon$ and the $k-\omega$ models, since the first one had severe accuracy problems in flows with negative pressure gradients and the second was too sensitive to freestream conditions. $k-\omega$ SST essentially uses the first model when far away from a wall and the second near a wall[3], in order to bypass their flaws.

Another widely known model is the one proposed by P. R. Spalart and S. R. Allmaras. This model makes use of another variable, the so called turbulent eddy viscosity, defined as

$$\nu_t = \frac{C_\mu k^2}{\varepsilon} \tag{5.6}$$

with C_μ being a constant. Its material derivative will then be

$$\frac{D}{Dt}(\rho\tilde{\nu}) = \bigtriangledown\cdot(\rho D_{\tilde{\nu}}\tilde{\nu})+\frac{C_{b2}}{\sigma_{\nu_t}}\rho\tilde{\nu}^2+C_{b1}\rho\tilde{S}\tilde{\nu}\,(1-f_{t2})-\left(C_{w1}f_w-\frac{C_{b1}}{\kappa^2}f_{t2}\right)\rho\frac{\tilde{\nu}^2}{\tilde{d}^2}+S_{\tilde{\nu}} \tag{5.7}$$

where

$$\nu_t = \tilde{\nu}\frac{\chi^3}{\chi^3+C_{v1}^3} \tag{5.8}$$

and

$$\chi = \frac{\tilde{\nu}}{\nu} \tag{5.9}$$

and the other undefined parameters are coefficients tuned with empirical data. At this point, there are two more equations to establish in order to close the system. One is equation (5.6), and the other replaces the Boussinesq hypothesis and is

$$-\overline{u_i'u_j'} = \nu_t\left|\frac{du}{dy}\right| = ak \tag{5.10}$$

where a is a constant. For practicality, ν_t is transformed into $\tilde{\nu}$, which remains linear even when it is very close to the wall, which as a consequence allows accurate simulations near the wall without using an excessive number of cells[4].

It is intuitive that a model that uses more transport equations will also require less hypotheses and approximations, leading to an overall more accurate solution of the flow. The reason why Spalart-Allmaras is still considered a valid alternative to k-ω SST is that in general it is much less demanding in terms of computational effort, memory and stability, having fewer problems even when poorer meshes are used. Because of this, it will also be used in the simulations to be described in this project, as it is also indicated for aerodynamic flows, giving a level of accuracy which is comparable to that of k-ω SST in many instances.

A significant issue is that the Spalart-Allmaras model tends to generate turbulence as soon as a wall is encountered. This is not an issue when dealing with high Reynolds numbers, as the portion of laminar flow will be very small in reality. When dealing with lower Reynolds numbers though, a large part of the flow over the walls may remain laminar before a transition occurs. Not taking this into consideration may lead to completely wrong estimations of the characteristics of the flow and of the skin friction coefficient, making the whole simulation pointless. Therefore a transition model must also be defined. In SU2 it is possible to implement with Spalart-Allmaras the Bas-Cakmakcioglu algebraic transition model[5]. This model does not require any additional transport equations, but only an intermittency function, which is multiplied by the turbulence production term, damping it and delaying its insurgence until certain requirements are met. An additional parameter must be considered in this case, which is the free-stream turbulence intensity, defined as

$$I = \frac{u'}{U} = \sqrt{\frac{1}{3}(u_x'^2 + u_y'^2 + u_z'^2)} = \sqrt{\frac{2}{3}k} \tag{5.11}$$

5.2 Problem definition and background

5.2.1 Ishii airfoil

The first numerical simulation will be performed on the Ishii airfoil. It is to be kept in mind that the airfoil used for the AUG is a modified version, but with these simulations, the intent is in assessing the quality of the solutions provided by CFD with a Spalart-Allmaras turbulence model paired with a Bas-Cakmakcioglu transition model, or a k-ω SST turbulence model. Already in 2D, XFoil should have provided an accurate result, as the flow is very slow, and therefore incompressible, and the airfoil is thin. Additionally, a wide range of experimental data provided by Anyoji and Hamada[2] is available, making it possible to make comparisons to

assess the quality of the CFD solution. First are provided xFoil and experimental data on the polar curves for lift and drag coefficients at multiple Reynolds numbers. Additionally, pictures of the flow around the airfoil from wind tunnel experiments are provided, along with the pressure coefficient distribution obtained on xFoil at a null angle of attack and a Reynolds number of 23.000.

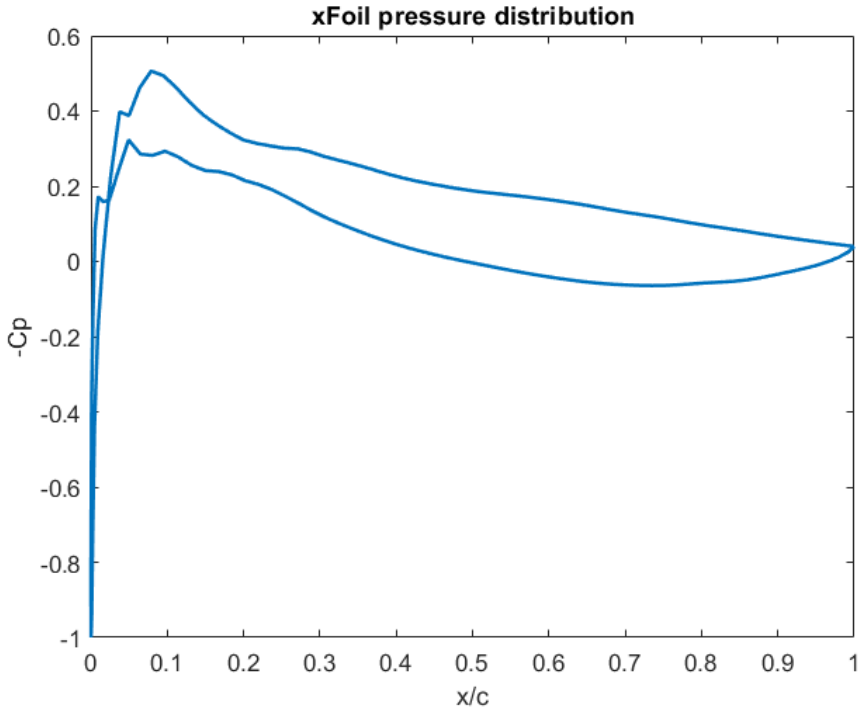

Figure 5.1: Pressure distribution calculated by xFoil over an Ishii airfoil at a null angle of attack and a Reynolds number of 23.000.

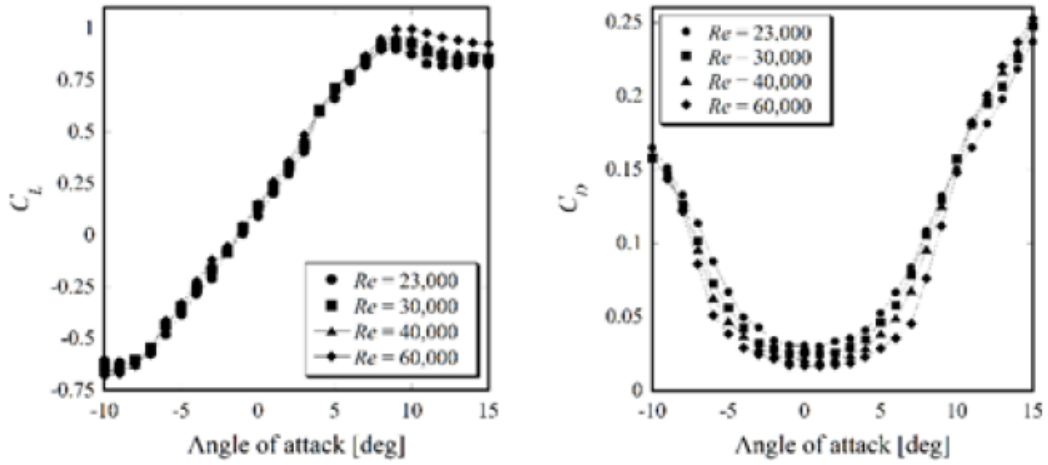

Figure 5.2: Lift and drag data observed through wind tunnel experiments by Anyoji and Hamada on an Ishii airfoil at a Reynolds number of 23.000.

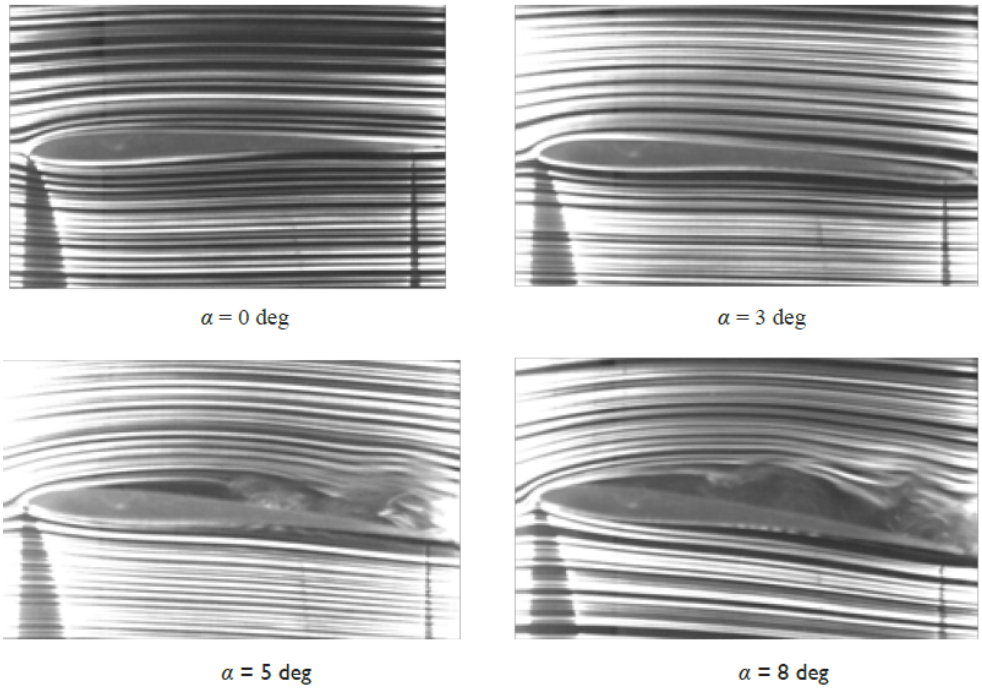

Figure 5.3: Flowfield over an Ishii airfoil at a Reynolds number of 23.000.

5.2.2 2D profiles of the hulls

A study on the 2D profile is also made to understand the differences in turbulence development on a 2D profile and on the solid obtained from its rotation about the longitudinal axis. In this case, the results should be the same as a 3D geometry, since no angle of attack is present and the profile is that of an axisymmetric body, but certain transition models may actually provide different solutions between a 2D and a 3D geometry. No experimental data is available for this model, having it been developed only in this project. The only data available is the pressure distribution calculated with xFoil. The simulations are always performed at null angles of attack, and the main points of interest this time will be the skin friction coefficient, which also provides indications on flow transitions and separations, and drag coefficient.

5.2.3 3D geometries of the hulls

The final objective of the simulations is to evaluate the accuracy of the method used to design the hull. No actual data is available to see how accurate the CFD simulations are in this case, they will be compared with the predictions that were made in chapter 3, specifically on the total drag over the hull's surface at various speeds, and where flow transition occurs. Ideally, the results will be the same as those obtained by the 2D simulations.

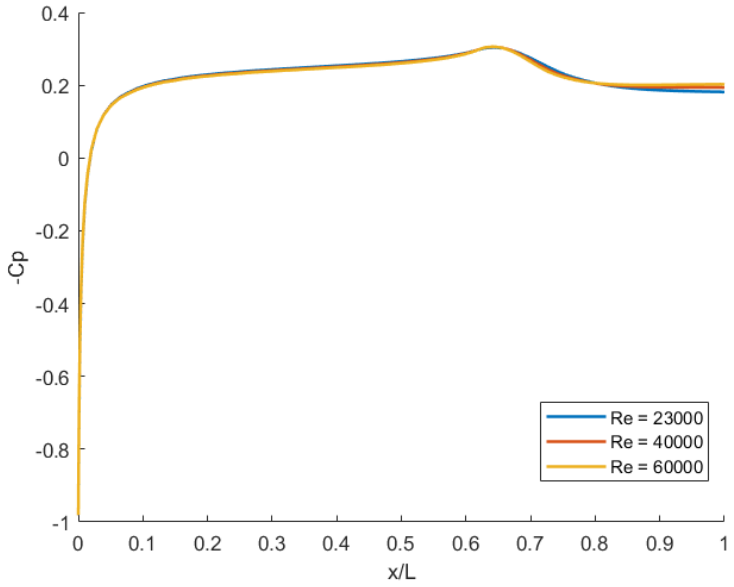

Figure 5.4: Pressure distribution calculated by xFoil over the hull profile at a null angle of attack and various Reynolds numbers.

5.3 Design of experiments

The ultimate objective of these CFD simulations is to make an assessment on the quality of the predictions of the total hydrodynamic resistance to which the hull is subject. Because of how critical flow transition is in this case, it is necessary to verify whether the turbulence models adopted are adequate. Because of this, a series of experiments were done on the Ishii airfoils, since experimental data is already available in this case, making it possible to asses the quality of the solutions for low Reynolds external flows. In this case, the two main features to observe will be the force coefficients, which will be evaluated at angles of attack in the ranges of -2^o to 8^o and Reynolds numbers 23000, 40000 and 60000, and the streamlines that form the flowfield, to see how closely they match figure 5.3. After that, the geometry of the hull will be examined. In this case, only drag will be observed, since lift should not be present on a symmetric geometry with no angle of attack. Particular attention will be on skin friction coefficient and turbulence kinetic energy. In all simulations, being drag the most important aspect, a grid capable of properly capturing the wake must be employed, so the most indicated type is the C-grid, which will be described in detail in the next paragraph.

5.4 Mesh generation and description

5.4.1 Ishii airfoil

To generate the meshes, the open source software Gmsh was used, which allows to create su2 format grids, making it compatible with the software SU2. The downside is that it is not very intuitive as a software and requires considerable programming from the user, although it allows more freedom, for better or worse.

As previously mentioned, for all geometries a C-grid was designed. These are types of grids which are fully structured, as opposed to an O-grid, which generally only has a structured area covering the boundary layer and then becomes unstructured after a prescribed distance from the walls. In general, while fully structured grids are harder to design and to run simulations to convergence with, they also have better predictions of drag forces, since they capture the wake more efficiently than a hybrid mesh, which will have greater numerical dissipation outside the boundary layer.

C-grids have a curved farfield at the side of the leading edge, which straightens at the opposite end. The volume around an airfoil or any 2D profile in these instances is divided in five areas: one that covers the leading edge, one that covers the pressure side, one that covers the suction side and two symmetrical areas that split the domain in two at the end of the trailing edge. In certain cases it is possible to divide the domain in three areas by unifying the ones covering leading edge, pressure and suction side, but this may prove to be problematic for airfoils with curvature changes on either side, such as the Ishii. For this last one in fact, an additional area had to be drawn for the trailing edge, since it has a non negligible thickness, instead of the more common finite angle. The division in blocks and the overall mesh are more clearly shown in figures 5.5 to 5.7.

Sizing the elements can be a very delicate process. First of all, the grid must be fine enough to reach grid convergence, which will be further elaborated in later paragraphs. Away from the walls and closer to the farfield, where the flow gradients are smaller, the elements of the mesh can become larger, in order to avoid futile computational demands. Near the wall instead, elements must be thin enough to properly capture the viscous sublayer of the flow, which generally extends to a y^+ of 5, y^+ being an adimensionalized distance from the wall, defined as

$$y^+ = \frac{y}{\nu}\sqrt{\frac{\tau_w}{\rho}} \tag{5.12}$$

where y is the distance from the wall, ν is the kinematic viscosity, τ_w is the wall shear stress, and ρ is the density of the flow. The two terms under the square root

are also known as friction velocity. In general, the elements adjacent to the wall must have a y^+ no larger than 1. It is possible to estimate the size of the thickness of the cells, but since τ_w is an unknown it may require multiple simulations to fine-tune its peak value. It is also necessary to make sure that the width of the cells does not change too drastically. A good rule of thumb in the CFD community is not to have the widths of two adjacent cells differ by more than 20%, which makes it easier for the solution to reach convergence. This may be impossible at the border of the leading edge block, and in such cases it is necessary at least to make sure that such condition stands near the walls of the airfoil.

Overall, the radius of the leading edge block is 50 times the size of the airfoil's chord, and the trailing edge block is 60 times wider. The width of the cells in the pressure and suction blocks varied with a bump progression, making the elements at the leading and trailing edges 25 times smaller than the larger ones in the middle of each side. The leading edge was divided in 70 segments and the trailing edge had cells widening with a progression function of 1.07, while all rows increased in thickness with a progression function of 1.17. The wake block had an angle of 10° and used the same width progression as the two trailing edge blocks, but the thickness of the cells varied with a bump function, with the smaller elements also being 25 times thinner than the larger ones. These were the parameters at which grid convergence was reached and consistently reached a small enough residual, requiring a total of 53331 elements and 53900 nodes. Beyond this number of elements, no visible differences were found in the solution when using finer meshes.

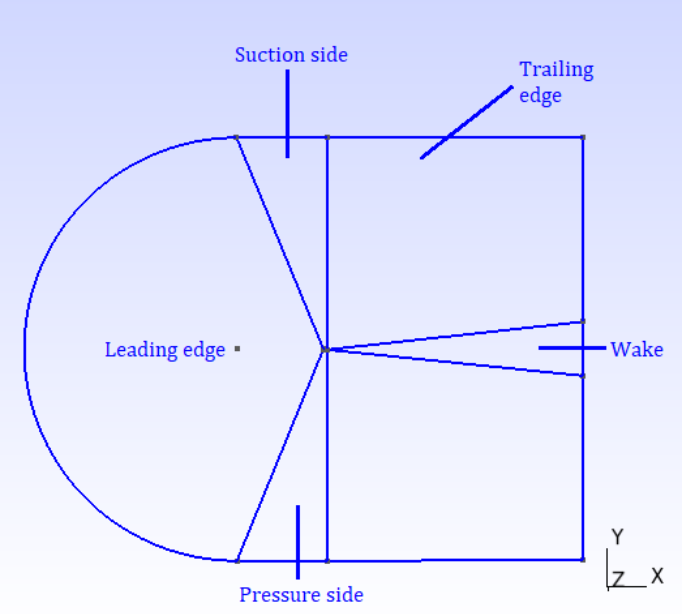

Figure 5.5: Block subdivision of the Ishii C-grid.

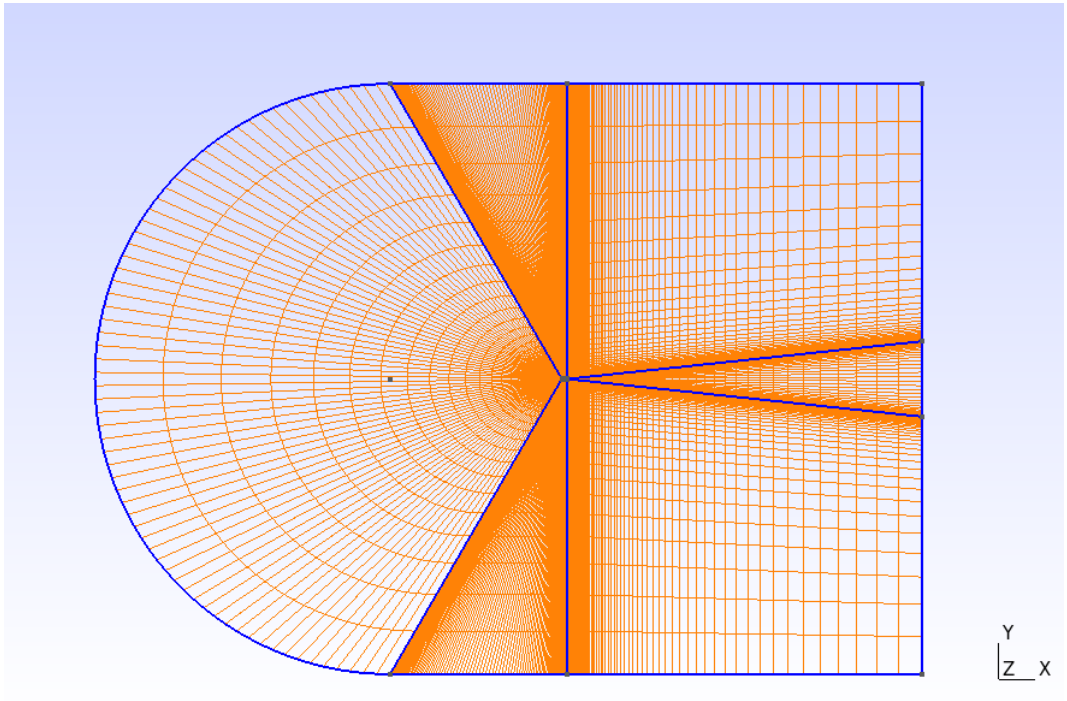

Figure 5.6: Complete view of the Ishii grid.

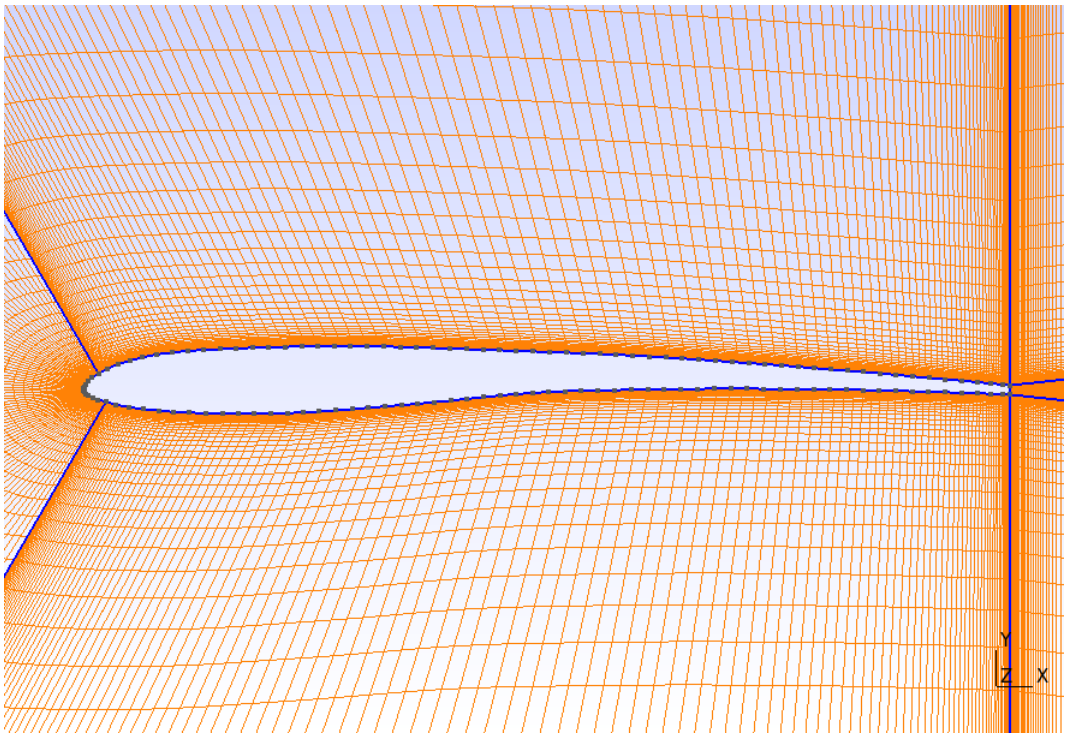

Figure 5.7: Zoomed view of the Ishii grid on the airfoil.

5.4.2 Hull profiles

The 2D hull profiles of both the CP60 and the CP65 have the same mesh structure as the airfoil, with the difference that they do not have a wake region. Once grid convergence was reached, the width of the cells in the pressure and suction blocks varied with a bump progression, making the elements at the leading and trailing edges 25 times smaller than the larger ones in the middle of each side. The leading edge was divided in 70 segments and the trailing edge had cells widening with a progression function of 1.075, while all rows increased in thickness with a progression function of 1.181. Due to the similarity in the geometry of the two hulls, the same grid parameters were used t design both grids and satisfactory grid convergence was attained for both cases with a total number of 46620 elements and 47135 nodes

In the figures below the C-grid for the hull profiles are shown.

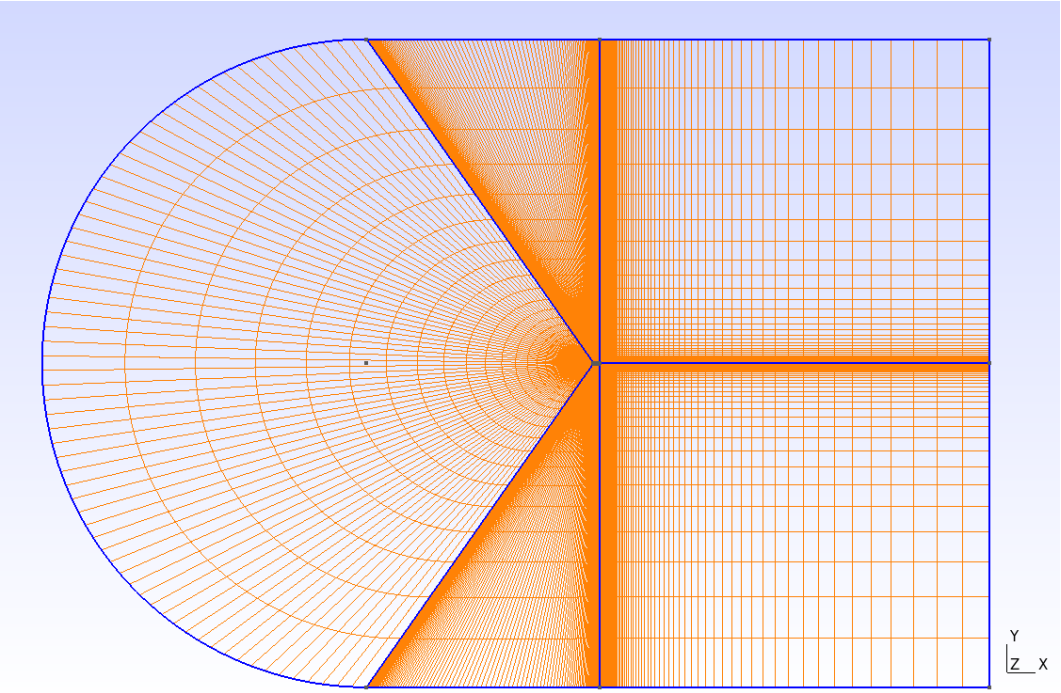

Figure 5.8: Complete view of the 2D profile grids.

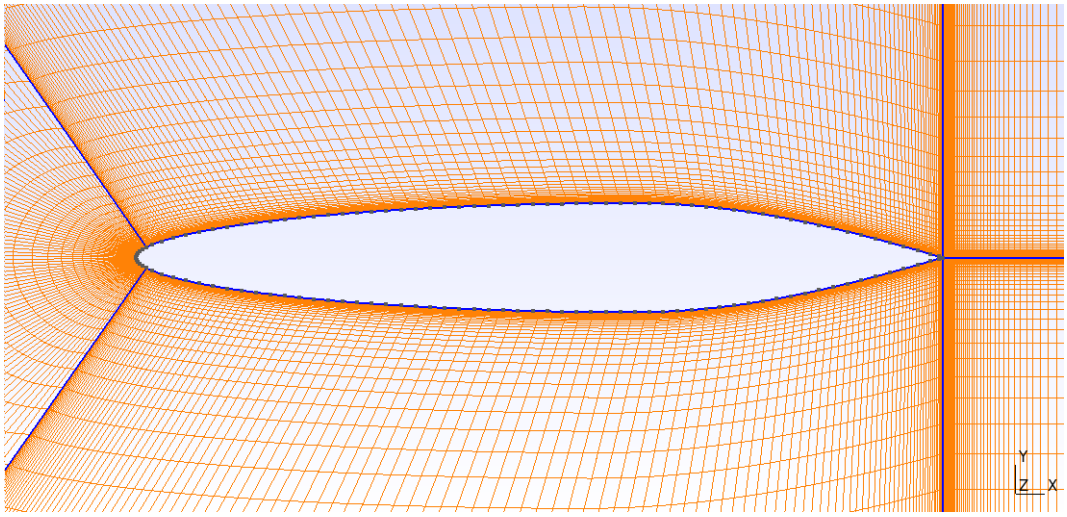

Figure 5.9: Zoomed view of the 2D CP60 grid.

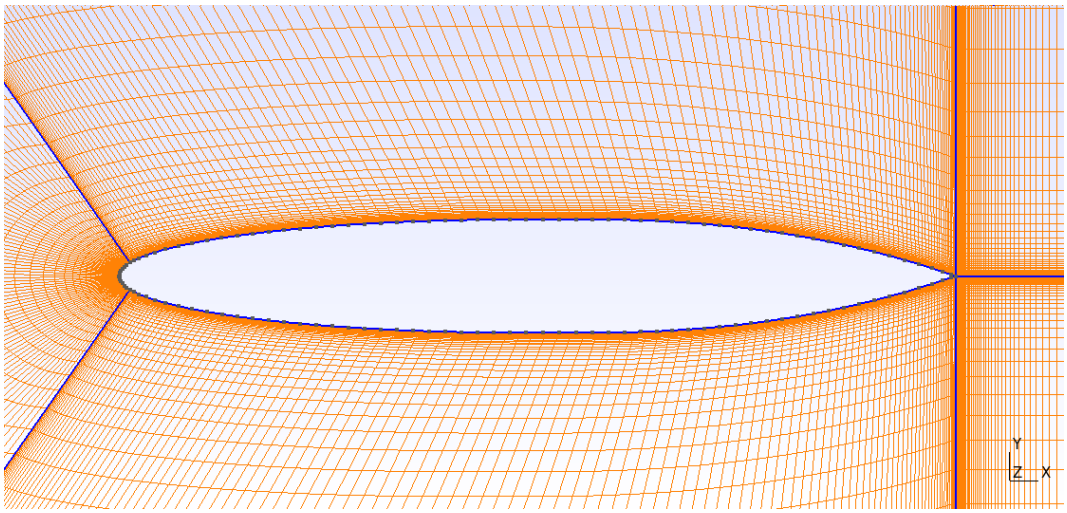

Figure 5.10: Zoomed view of the 2D CP65 grid.

5.4.3 3D geometries of the hulls

In order to generate the meshes in 3D, half of the 2D profile mesh was used to apply an extruded rotation of 90°. Therefore, the mesh is only a quarter of the whole geometry. There are two reasons to proceed this way. The first is that Gmsh only allows for extruded rotations strictly smaller than 180° and even using multiple extruded rotations often leads to unpredictable results. The second reason is that using a quarter of the whole mesh allows to use a quarter of the elements without any loss in the quality of the solution, since it is possible to simply apply symmetry conditions over two faces of the boundary. The end result is therefore a quarter of a revolved C-grid. Even when considering the meshing of the 2D profile,

the distribution of the number of elements had to be changed, since some of them would otherwise have excessive aspect ratios. In such occurrences, SU2 would still be able to run, but would struggle to reach satisfyingly low residuals. So on the 2D profile, once grid convergence was reached, the width of the cells at the wall of the pressure/suction block varied with a bump progression, making the elements at the leading and trailing edges 25 times smaller than the larger ones in the middle of each side. Half of the leading edge was divided in 35 segments and the trailing edge had cells widening with a progression function of 1.075, while all rows increased in thickness with a progression function of 1,181. The revolution of this 2D profile would have 40 layers over a 90° angle. In figure 5.11 this is better shown. Because of the similarities between the geometries of the two hulls, no significant changes had to be made to the mesh programming and both reached satisfying grid convergence with the same number of elements. In total, the number of elements was 814380 and the number of nodes was 850680.

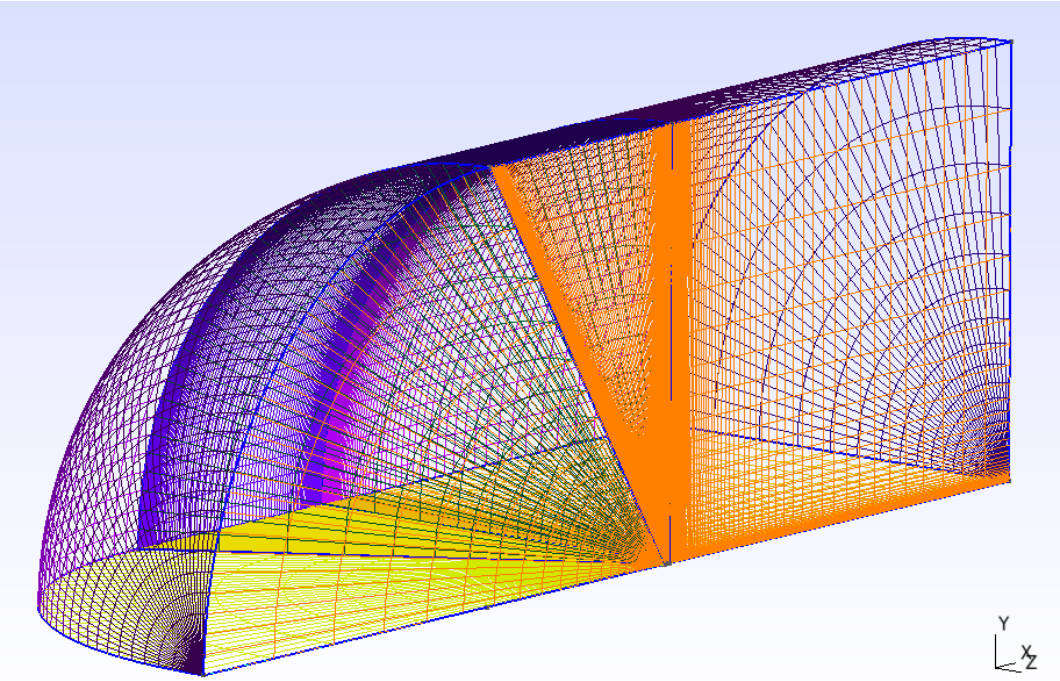

Figure 5.11: Extruded 3D grid of the CP60 model.

5.5 Numerical schemes

5.5.1 Ishii airfoil

Given that the fluid in which the AUG moves is water and being this motion far from being transonic, it is safe to assume that the flow will be incompressible.

Therefore, in order to lighten the computational load, an incompressible RANS solver was used. As turbulence models, first an SST model without an added transitional correction was used, and then a Spalart-Allmaras turbulence model with a Bas-Cakmakcioglu transition model. The experiments done by Anyoji and Hamada specified that there was a free-stream turbulence intensity of 0.3%. Although this is a small enough value for a wind tunnel experiment, a more realistic value would be even lower than that when dealing with objects moving through a still flow. But since the Ishii airfoil CFD experiments have the purpose of evaluating the quality of these models, the higher turbulence intensity value was used.

A constant kinematic viscosity of 0.00151 $kg/m \cdot s$ was set, along with a constant density of 1027 kg/m^3. The velocity was then tuned in order to obtain the Reynolds numbers of the aforementioned experiments, specifically of 23.000, 40.000 and 60.000. Green-Gauss was used as the numerical method to calculate spatial gradients, along with and an adaptive Courant-Friedrichs-Lewy number (CFL), which started the simulation at 20 and had a down factor of 0.1 and an up factor of 1.2. Obviously an Euler-implicit time discretization occurs, otherwise the maximum CFL number would need to always be lower than 1, or it would violate the Courant-Friedrichs-Lewy condition.

A biconjugate gradient stabilized linear solver was used, along with an ILU preconditioner. The flux-difference splitting (FDS) convective method was used. This is an upwind scheme, which is only first order accurate. In general, the procedure was to first compute a first order solution, which has less difficulties to converge, and then use it to start a second order solution, still with the FDS scheme, which would obviously be more accurate. At times a second order convective scheme would also be used for turbulence, but since it didn't produce significant differences in the final solution and often brought difficulties in achieving lower residuals, it was ultimately discarded in favor of a first order turbulence scheme. Conditions for the simulations to halt would be reaching a pressure root mean square (RMS) error of $1E-12$. If this was achieved, the simulation would be deemed successful, otherwise it would halt after 30.000 iterations, and the acceptable pressure RMS residual would be slightly increased. Especially for the cases of high angles of attack, pressure RMS residuals of $1E-10$ were accepted.

5.5.2 2D and 3D hull geometries

The configuration file used for the 2D hull profiles' simulations was very similar to the one used to study the Ishii airfoil. The main differences were in the free-stream turbulence intensity, which was decreased to 0.18% and the free-stream velocity. Even though throughout the course of a dive the density and kinematic

viscosity of seawater vary, an average value was considered for them, the same as the Ishii airfoil. The free-stream velocity though changed in order to have Reynolds numbers ranging between 650.000 and 1.300.000, which would correspond to velocities between 0.5 and 1.0 m/s. The configuration file for the 3D geometries of the hulls was virtually unchanged from the 2D case.

5.6 Results

5.6.1 Ishii airfoil

First of all, the pressure coefficient distribution of the Ishii airfoil is shown in figure 5.12.

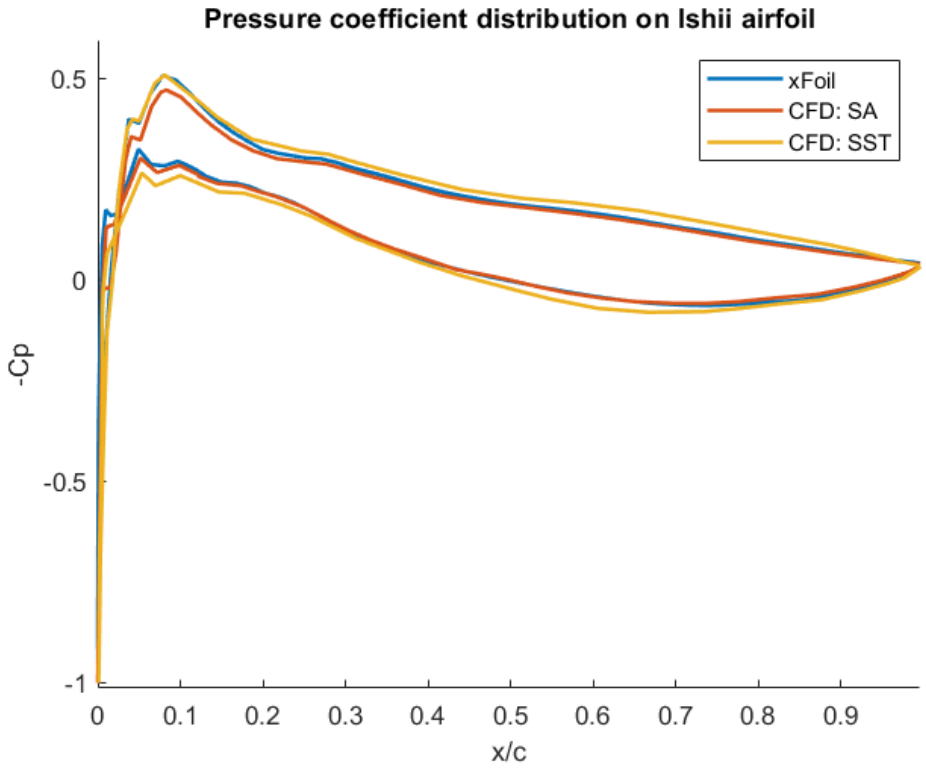

Figure 5.12: Pressure distribution over an Ishii airfoil at a null angle of attack and a Reynolds number of 23.000, evaluated with xFoil, a transitional Spalart-Allmaras turbulence model and an SST turbulence model.

When comparing the numerical solutions obtained with xFoil and the CFD models, the first thing that is possible to notice is that all the curves have similar developments, with local peaks at the same regions of the airfoil. Considering the xFoil solution the reference one, it is possible to see that the $k-\omega$ SST model seems better at capturing the peak at the leading edge on the upper surface, but then tends to overestimate it in the central part of the airfoil. The pressure coefficient's

absolute value tends to be underestimated throughout the lower surface. Of course as a consequence, the lift coefficient can be expected to be larger in the SST turbulence model, as it will in fact be shown even for other angles of attack. The transitional Spalart-Allmaras model seems to replicate xFoil's curve more faithfully, with the exception of the upper surface of the leading edge, where the absolute value of the pressure distribution is underestimated at the peak.

In figures 5.13 to 5.18 the polars for the Ishii airfoil at multiple Reynolds numbers are shown. Looking at the lift coefficient curves, all numerical methods have a tendency to overestimate lift, especially for angles of attack larger than 2°. It is interesting to notice also that these curves tend to be much more linear according to experimental data. Among the numerical methods, the transitional Spalart-Allmaras turbulence model seems to be the closest to the experimental results, although the differences between the curves are still quite noticeable. The most significant differences though can be seen in the drag polars. In these, the numerical data seems to significantly underestimate hydro/aerodynamic resistance compared to experimental data, especially around the zero-lift point. Once again, the Spalart-Allmaras model seems to provide the closest results, having significant overlap with the xFoil curve at lower angles of attack and approaching the experimental data for higher ones. The discrepancy in the case of the Reynolds number at 60.000 for larger angles of attack is most likely due to poor residual convergence, which only managed to reach 9.8 E-10.

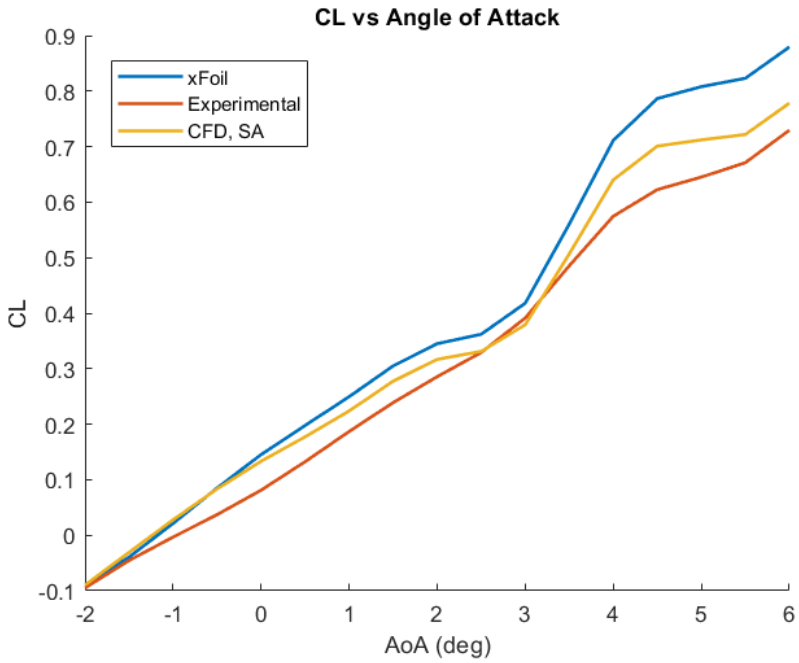

Figure 5.13: Lift coefficient plotted against angle of attack at a Reynolds number of 23.000.

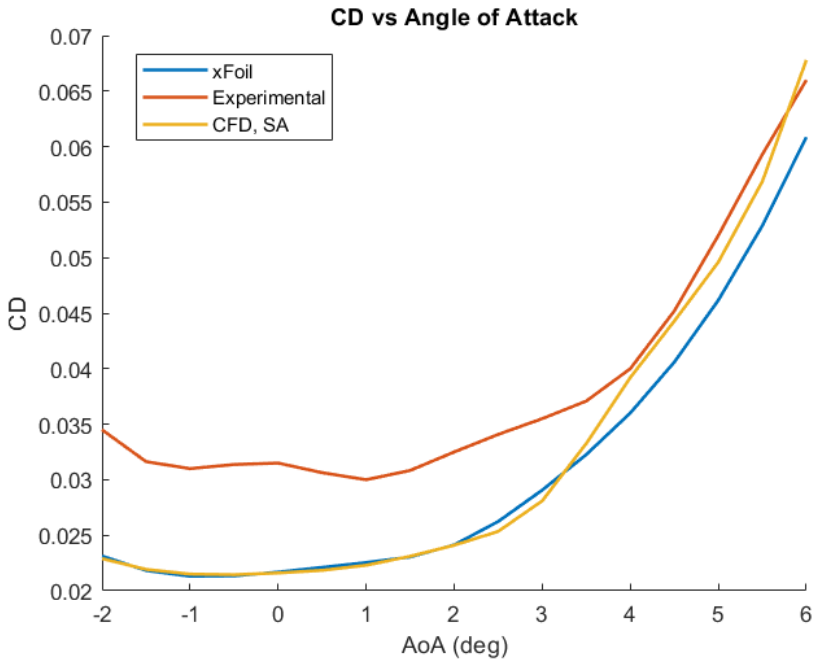

Figure 5.14: Drag coefficient plotted against angle of attack at a Reynolds number of 23.000.

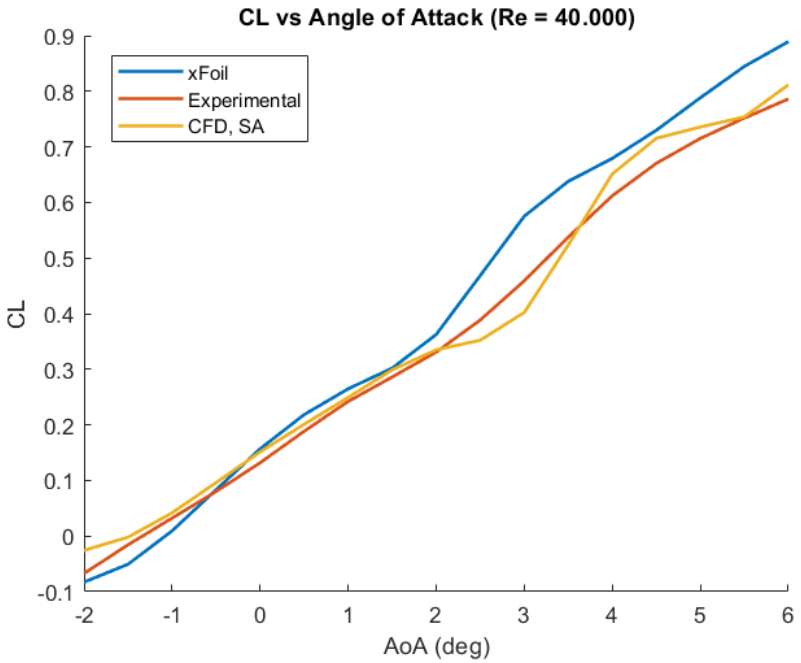

Figure 5.15: Lift coefficient plotted against angle of attack at a Reynolds number of 40.000.

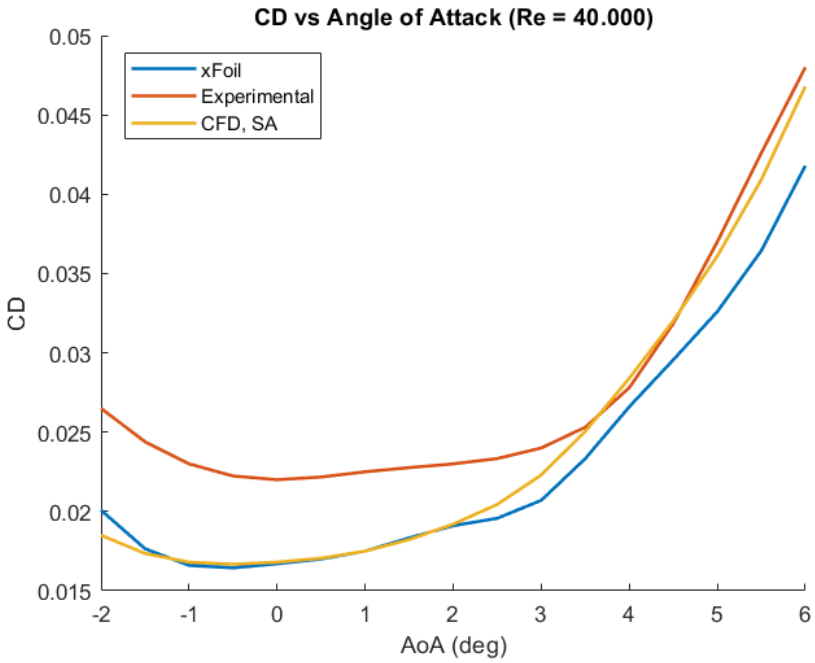

Figure 5.16: Drag coefficient plotted against angle of attack at a Reynolds number of 40.000.

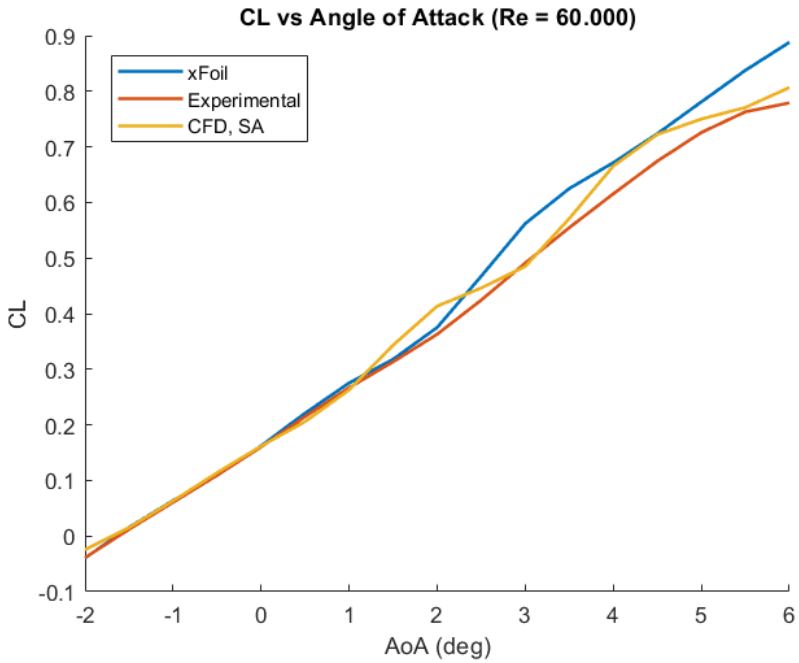

Figure 5.17: Lift coefficient plotted against angle of attack at a Reynolds number of 60.000.

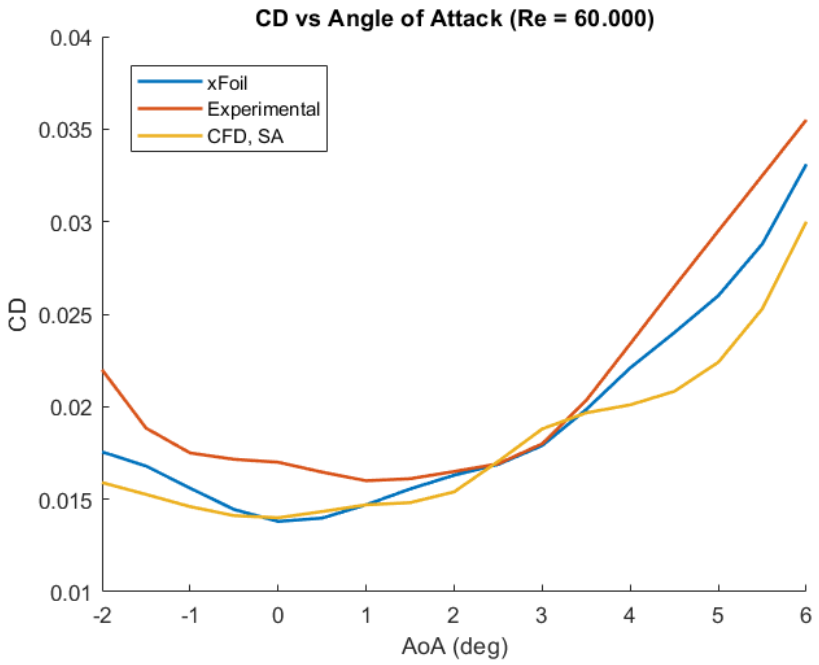

Figure 5.18: Drag coefficient plotted against angle of attack at a Reynolds number of 60.000.

Finally, a comparison of the actual flows is made in figures 5.19 to 5.21, this time only for the case of a Reynolds number of 23.000. At a null angle of attack, the Spalart-Allmaras simulation has a fully laminar flow, with no separation occurring, while the SST model starts developing a turbulent boundary layer at halfway of the airfoil. As a consequence, another difference between the two models is that in the SST case the boundary layer at the trailing edge is slightly smaller, which is in accordance with the fact that drag is also smaller than the Spalart-Allmaras case. At an angle of attack of 3° the Spalart-Allmaras case shows a fully laminar flow once again, but with a laminar separation occurring at 60% of the chord. No such thing happens in the SST case, which instead has a turbulent transition beginning to develop at 30% of the airfoil. At an angle of attack of 5° the Spalart-Allmaras model exhibits a laminar separation occurring much nearer to the leading edge, followed by a turbulent transition, while in the SST model, no separation occurs, but there is a flow transition starting at 15% of the airfoil. In general, while separation and flow transition may sometimes occur at slightly different points of the airfoil, the main takeaway is that the transitional Spalart-Allmaras produced physically much more accurate results than the SST model, which did not predict any flow separations and instead anticipated flow transition by a large margin. From here on it can be assumed that the transitional Spalart-Allmaras will provide the most accurate predictions on the next cases.

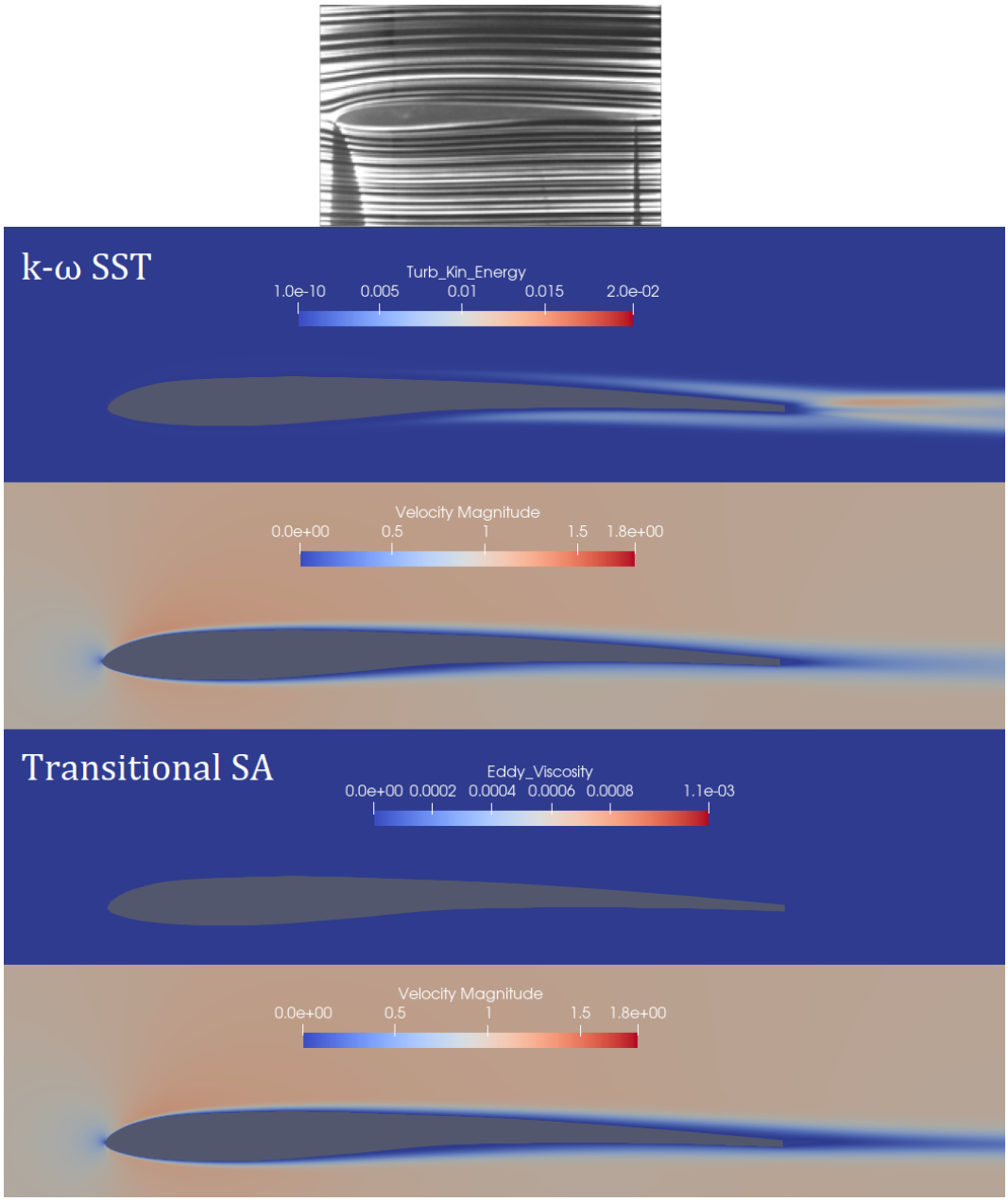

Figure 5.19: Wind tunnel experiment streamlines compared to turbulence and velocity over the Ishii airfoil at a null angle of attack and Re = 23.000 for $k-\omega$ SST and transitional Spalart-Allmaras turbulence models.

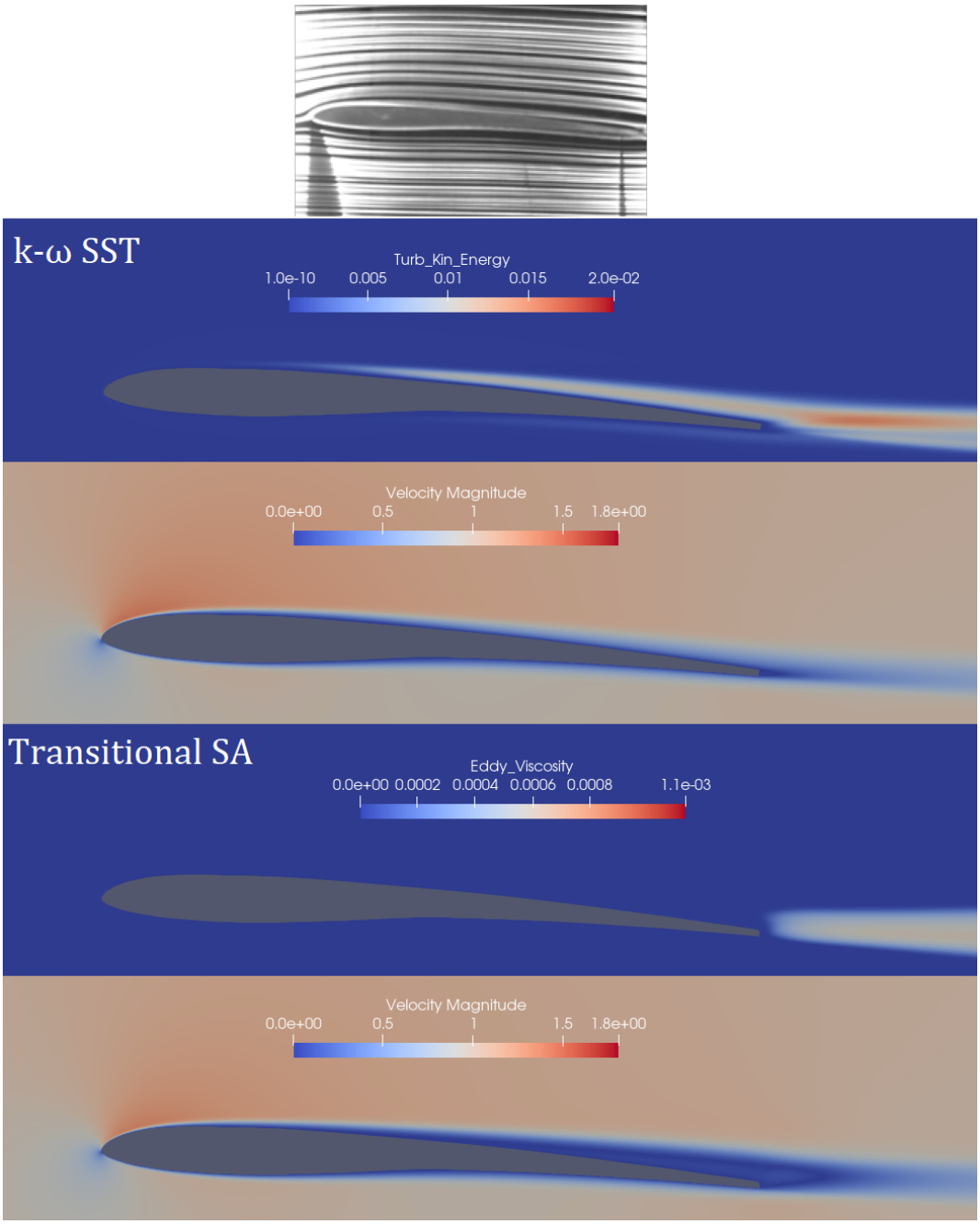

Figure 5.20: Wind tunnel experiment streamlines compared to turbulence and velocity over the Ishii airfoil at a 3° angle of attack and Re = 23.000 for $k-\omega$ SST and transitional Spalart-Allmaras turbulence models.

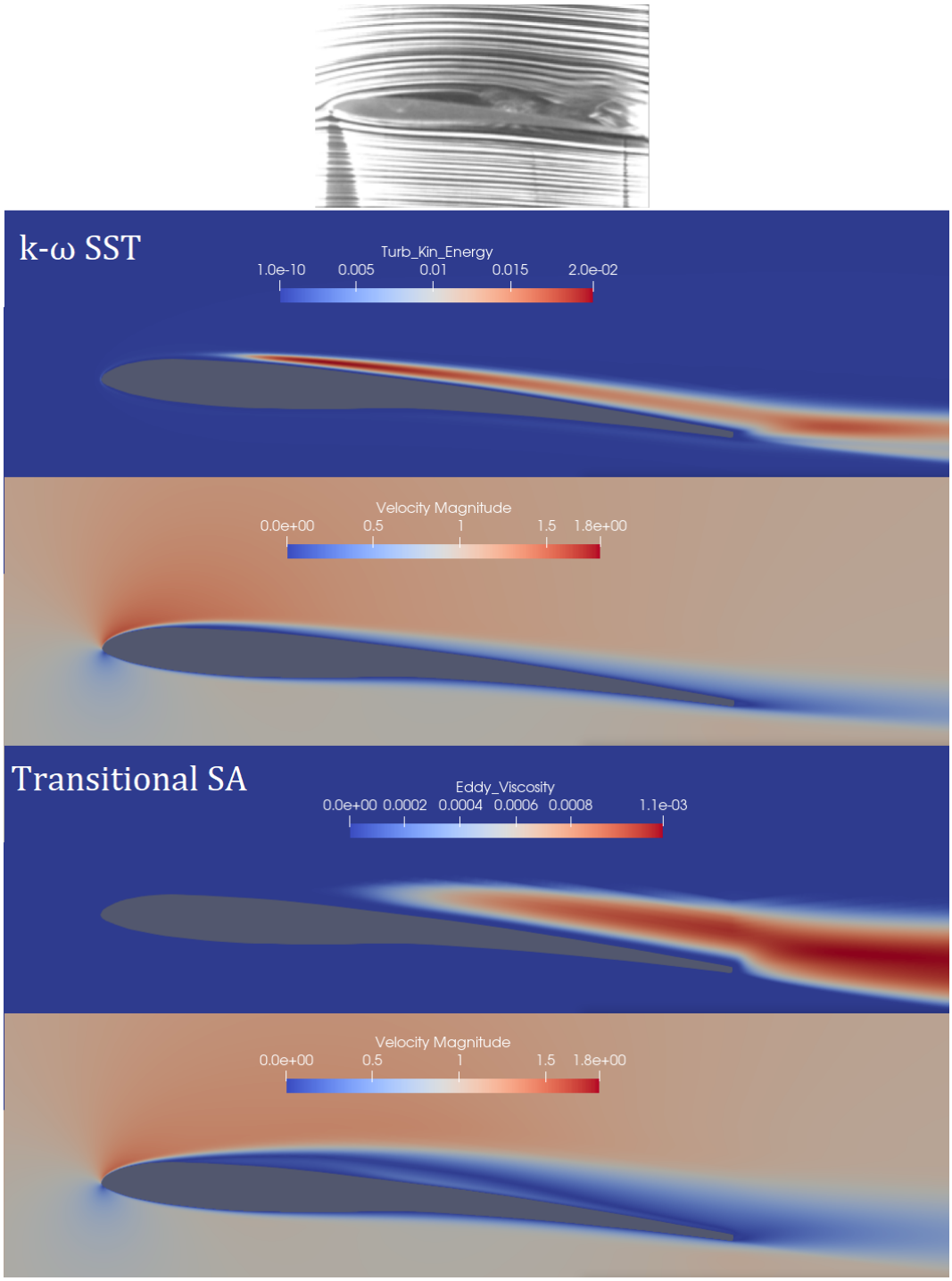

Figure 5.21: Wind tunnel experiment streamlines compared to turbulence and velocity over the Ishii airfoil at a 5° angle of attack and Re = 23.000 for $k-\omega$ SST and transitional Spalart-Allmaras turbulence models.

5.6.2 2D hull profiles and 3D geometries

In figures 5.22 to 5.29 are provided the skin friction coefficient plots along the wall and eddy viscosity and velocity renders for both the CP60 and the CP65 hull profiles at Reynolds numbers of 650.000 and 1.300.000, corresponding roughly to a velocity of $0.5m/s$ and $1.0m/s$ at a water temperature of $7°C$. The simulations are done with the transitional Spalart-Allmaras turbulence model, while the simple $k-\omega$ SST model was discarded, in light of the poor results of the previous experiments.

The first thing that can be noticed is that flow transition always occurs past the midbody, at $75-80\%$ of the whole length of the hull. Even when doubling the Reynolds number, the flow transition point does not seem to be affected significantly. By analyzing the skin friction coefficient though, it is possible to see that the flow will still be affected. At Reynolds 650.000 there are multiple small flow separations and reattachments, which are also visible when zooming on the velocity renders. Also, even though the curves look similar in the nose and midbody regions, at higher Reynolds, as expected, the skin friction coefficient values are smaller.

Regarding the 3D mesh, it did exhibit some differences from the 2D case, visible in figures 5.30 and 5.31, which show the differences between the 2D and 3D mesh results for the CP60 at a Reynolds number of 650.000. First of all, the skin friction coefficient is slightly higher in the 3D simulation until about half of the hull's length, but then it becomes lower towards the transition region. Both cases then have flow separation, with the presence of a recirculation bubble, but after that the boundary layer has another attachment-detachment cycle in the 2D case, while it becomes somewhat stable in the 3D case. Looking at the velocity renders, two main differences can be seen: outside the boundary layer the hull exhibits much steeper gradients in the 2D case, while the 3D case seems almost flat, besides the stagnation point at the nose tip. The second difference is in the boundary layer at the tail, which is visibly thicker in the 3D case. This might be due to the lower velocity upstream, which might be unfavorable to separation. The result is that the boundary layer at the tail in the 3D case is thicker and transition and separation occurs slightly sooner. As a consequence, the drag coefficient is slightly higher, although only by a small percentage, about 2% on average, depending on the Reynolds number. The differences can be attributed to the fact that the 2D case does not represent the profile of an axisymmetric body, but rather a profile extruded to infinity in the direction normal to its plane. So these two shapes are actually quite different, but the results are comparable because both are symmetric and at a null angle of attack.

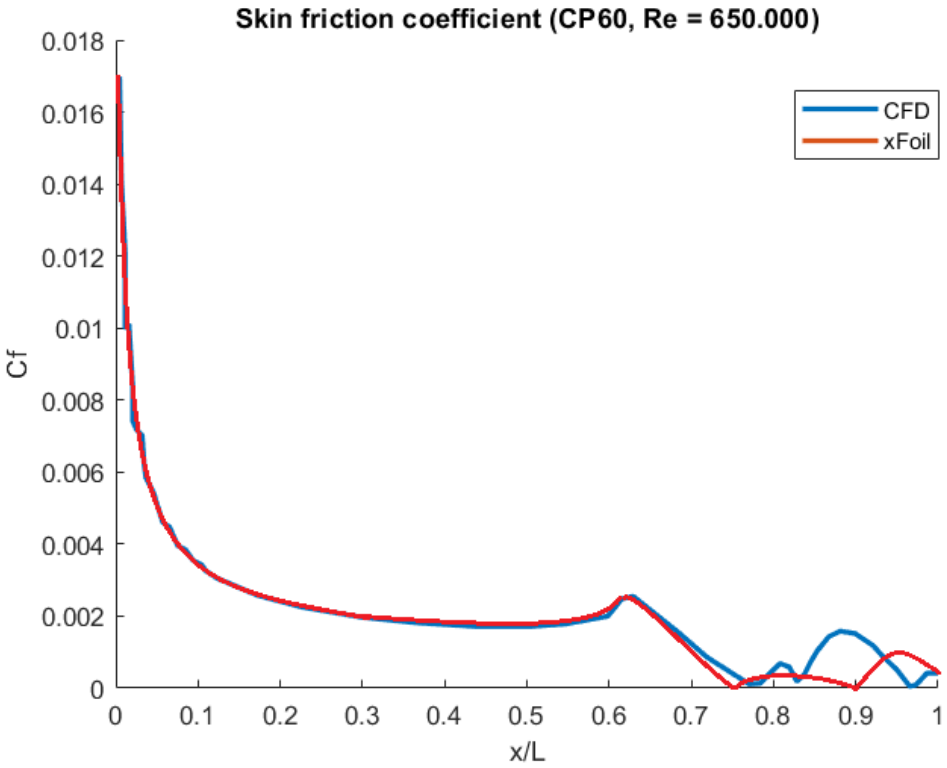

Figure 5.22: Skin friction coefficient over the 2D profile of the CP60 hull at Reynolds 650.000.

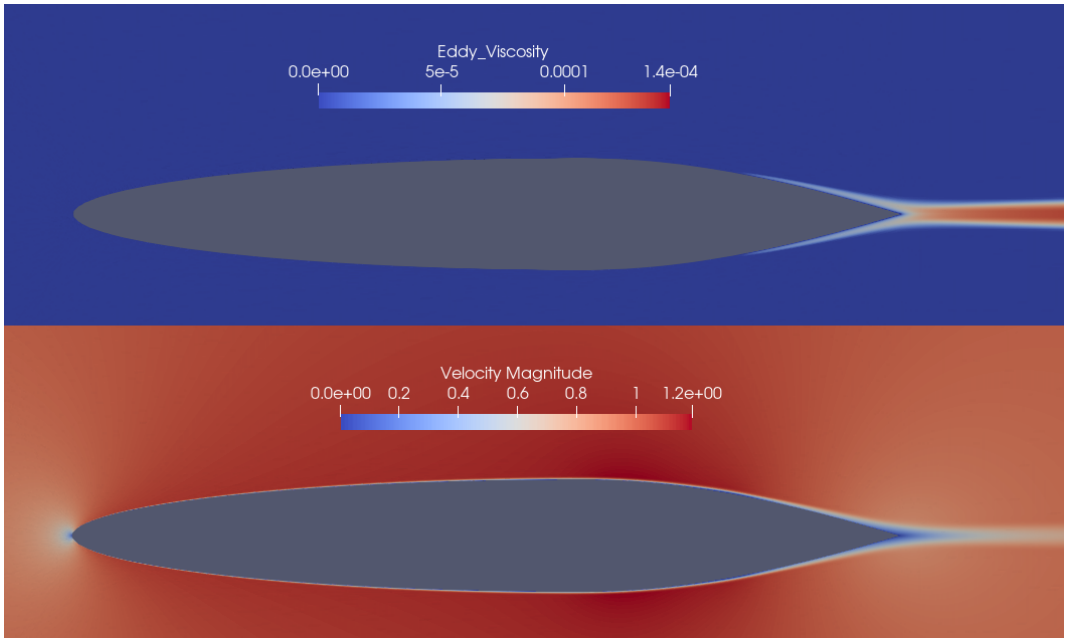

Figure 5.23: Render of eddy viscosity and velocity of the 2D profile of the CP60 hull at Reynolds 650.000.

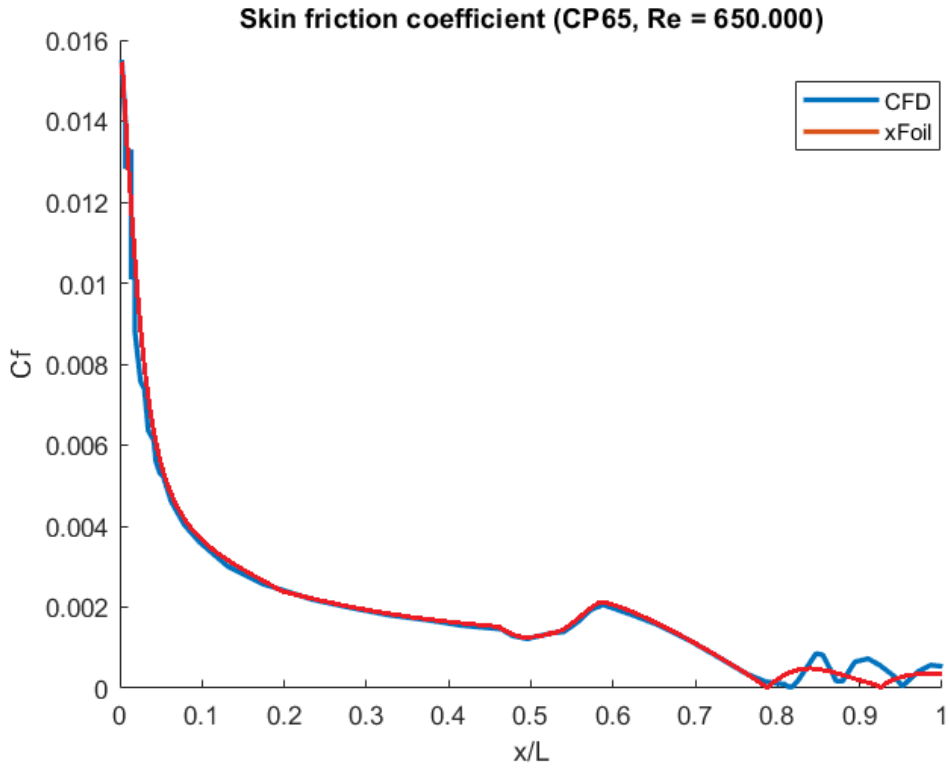

Figure 5.24: Skin friction coefficient over the 2D profile of the CP65 hull at Reynolds 650.000.

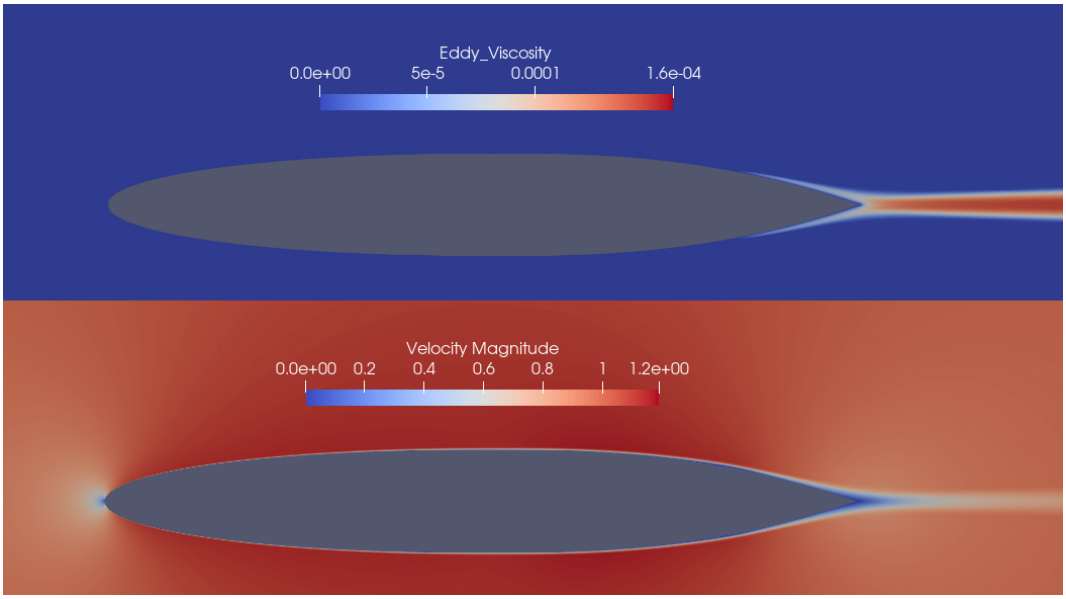

Figure 5.25: Render of eddy viscosity and velocity of the 2D profile of the CP65 hull at Reynolds 650.000.

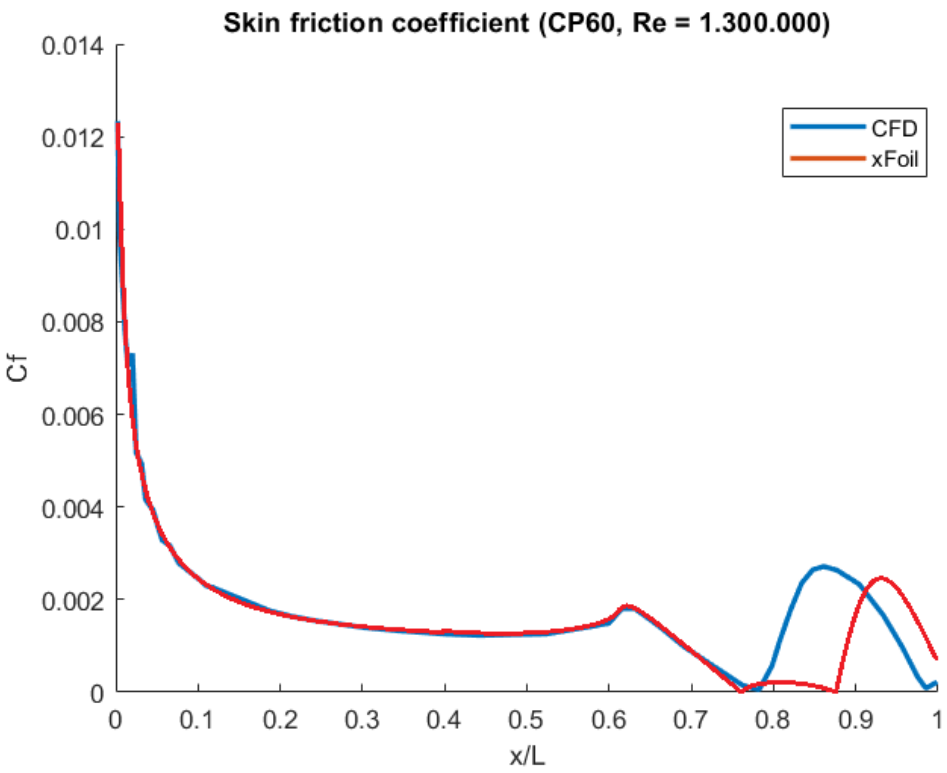

Figure 5.26: Skin friction coefficient over the 2D profile of the CP60 hull at Reynolds 1.300.000.

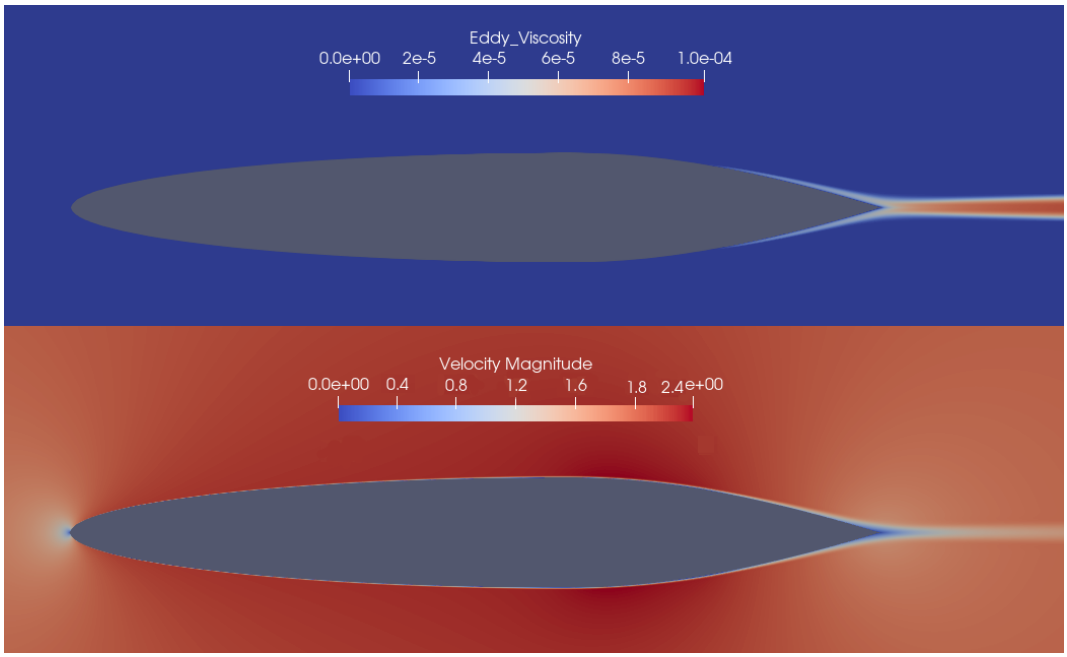

Figure 5.27: Render of eddy viscosity and velocity of the 2D profile of the CP60 hull at Reynolds 1.300.000.

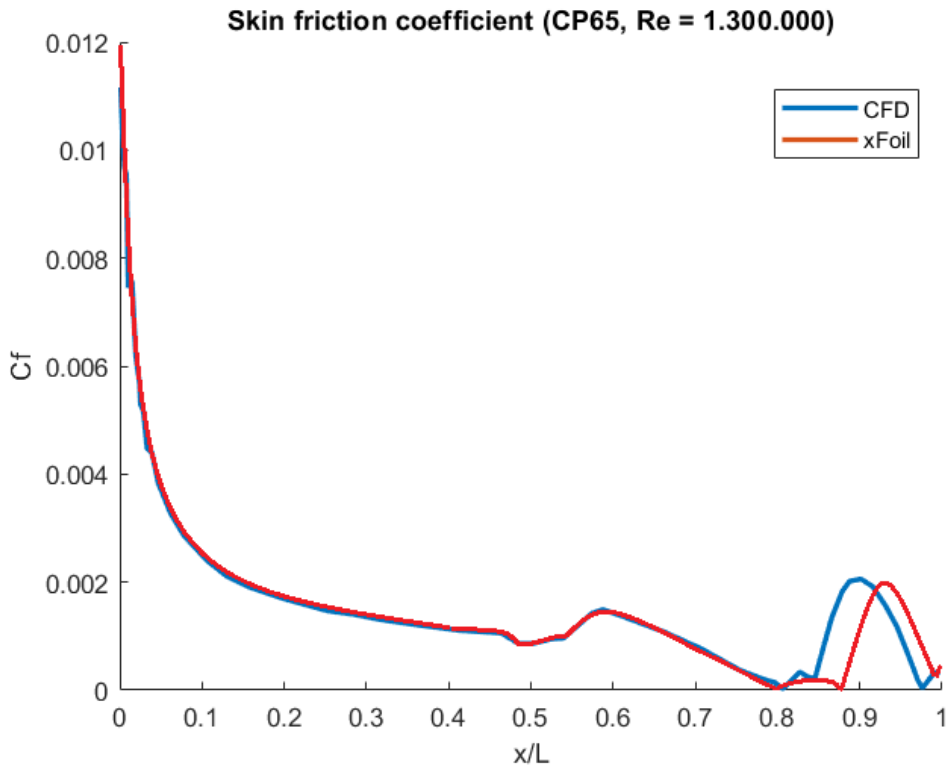

Figure 5.28: Skin friction coefficient over the 2D profile of the CP65 hull at Reynolds 1.300.000.

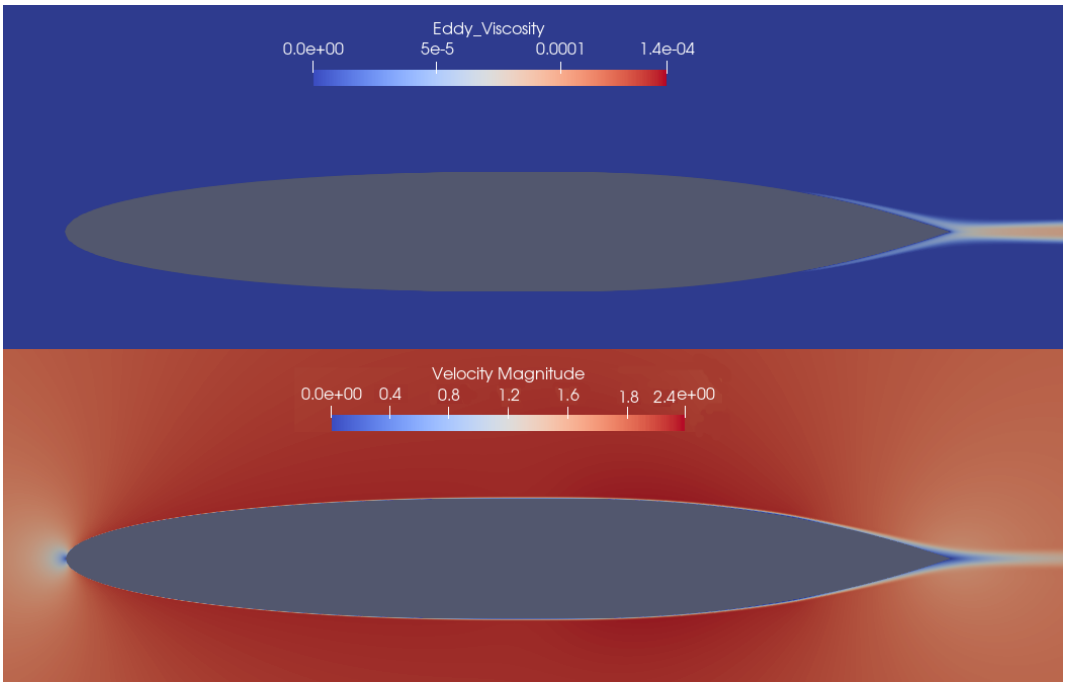

Figure 5.29: Render of eddy viscosity and velocity of the 2D profile of the CP65 hull at Reynolds 1.300.000.

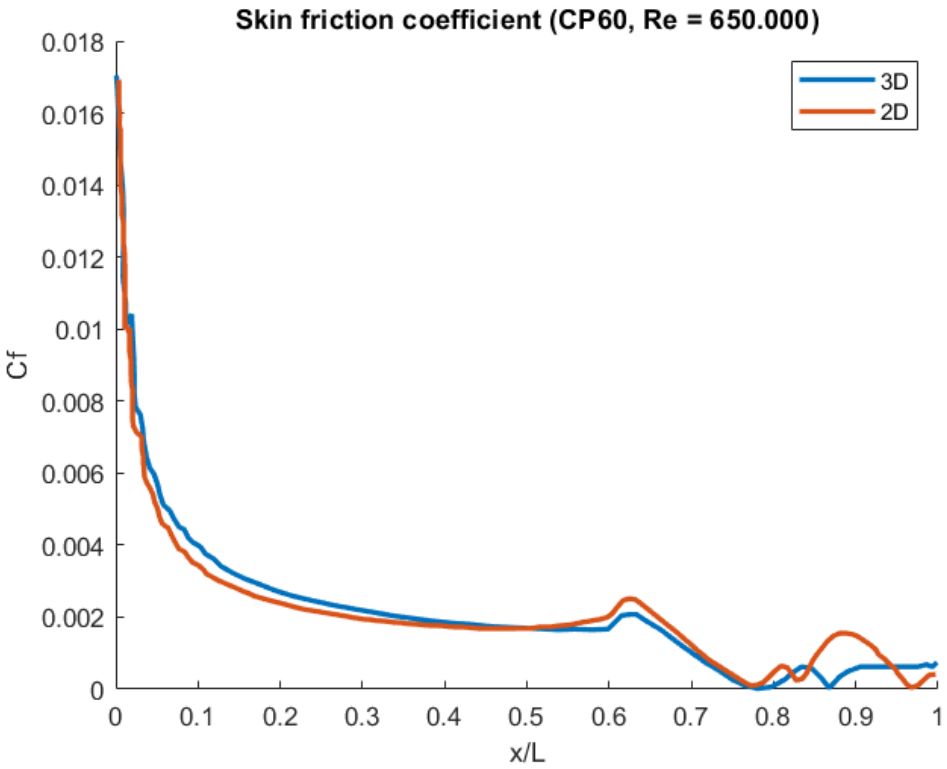

Figure 5.30: Skin friction coefficient over the 2D and 3D mesh of the CP60 hull at Reynolds 650.000.

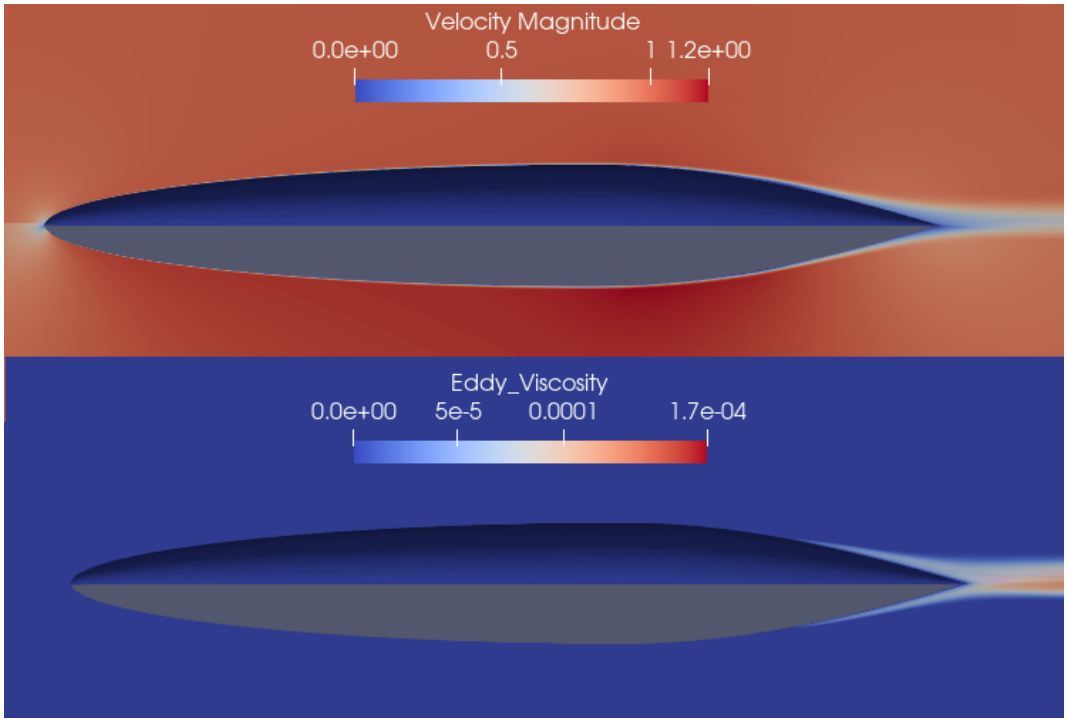

Figure 5.31: Render of eddy viscosity and velocity of the 2D and 3D mesh of the CP60 hull at Reynolds 650.000.

The tables below make a comparison between the drag coefficient values, total drag and transition points of the two hulls at velocities between 0.5 and 1.0 m/s, estimated by 2D and 3D CFD and analytically. It can be seen that even though the CP60 performs better than the CP65, the difference is not as remarkable as the results obtained during the hull design process.

Hull drag coefficient						
AUG	**CP60**			**CP65**		
Method	**CFD,2D**	**CFD,3D**	**GRAN**	**CFD,2D**	**CFD,3D**	**GRAN**
Re=650.000	0.00601	0.00613	0.00497	0.00614	0.00627	0.00610
Re=780.000	0.00570	0.00584	0.00485	0.00586	0.00598	0.00602
Re=910.000	0.00555	0.00567	0.00475	0.00569	0.00581	0.00595
Re=1.040.000	0.00531	0.00545	0.00463	0.00554	0.00566	0.00582
Re=1.170.000	0.00519	0.00533	0.00451	0.00530	0.00541	0.00571
Re=1.300.000	0.00491	0.00506	0.00441	0.00513	0.00524	0.00544

Table 5.2: Drag coefficient as a function of Reynolds number.

Flow transition point						
AUG	**CP60**			**CP65**		
Method	**CFD,2D**	**CFD,3D**	**GRAN**	**CFD,2D**	**CFD,3D**	**GRAN**
Re=650.000	0.750	0.747	0.461	0.783	0.778	0.291
Re=780.000	0.757	0.755	0.478	0.788	0.782	0.300
Re=910.000	0.761	0.758	0.490	0.791	0.783	0.308
Re=1.040.000	0.766	0.762	0.505	0.795	0.786	0.320
Re=1.170.000	0.770	0.764	0.512	0.798	0.790	0.337
Re=1.300.000	0.774	0.769	0.520	0.801	0.795	0.350

Table 5.3: Fraction of laminar flow over the length of the hull.

5.7 Grid convergence

It is necessary to make sure that the mesh used for the numerical methods is fine enough that results will not differ even when using finer grids. In order to do so, it's necessary to compare the results obtained from the same test case with different meshes and make sure that beyond a certain number of cells there are no more differences. If this is not the case, the grid will require to be refined. The best way to compare the results, rather than simply showing the renders, is to compare graphs of an arbitrary flow property across a certain region. To make the eventual differences more noticeable, it must be a region with large gradients of the chosen property. In this case, grid convergence will be shown for the 2D CP60 hull at a Reynolds number of 650.000. Three different meshes are compared, the coarsest of which will have 32.430 elements and 32.870 nodes, meaning that the finest mesh has approximately 50% more elements and nodes. The velocity magnitude over the boundary layer at the tip of the tail will be measured and is reported in the figure below.

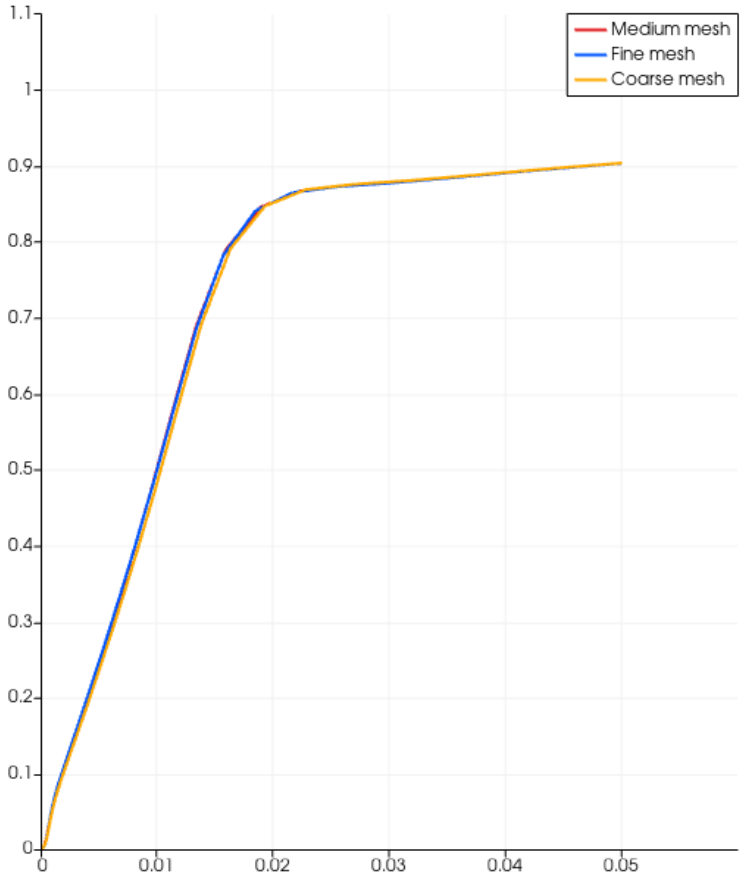

Figure 5.32: Grid convergence shown by comparing the boundary layer velocity profile at the tail of the CP60 hull at a Reynolds number of 650.000.

As it can be seen, despite the worse discretization, the coarsest mesh has very

similar results to the fine one, which overlaps almost perfectly with the medium mesh, suggesting a satisfactory level of grid convergence.

Bibliography

[1]https://www.cfdhub.polimi.it/user-facilities/

[2]Masayuki Anyoji, Daiki Hamada, 2019, *High-performance airfoil with low reynolds-number dependence on aerodynamic characteristics*, Flow Mechanics Research International Journal, Vol. 3, Issue 2, DOI: 10.15406/fmrij.2019.03.00055

[3]F. R. Menter, 1994, *Two-Equation Eddy-Viscosity Turbulence Models for Engineering Applications*, AIAA Journal, Vol. 32 No.8, DOI: 10.2514/3.12149

[4]P.R. Spalart, S.R. Allmaras, 1994, *A One-Equation Turbulence Model for Aerodynamic Flows*, 30th Aerospace Sciences Meeting and Exhibit, DOI: 10.2514/6.1992-439

[5]S.C. Cakmakcioglu, O. Bas, U. Kaynak, 2018, *A correlation-based, algebraic transition model*, Journal of Mechanical Engineering Science, Vol. 232, DOI: 10.1177/0954406217743537

Conclusions and possible future work

In this project the hydrodynamic surfaces for a new concept of an autonomous underwater glider were designed. While the flow can be considered incompressible throughout the entire journey of the glider, the main design difficulties were regarding flow transition. In the case of the wing design, significant hydrodynamic improvements were achieved without any unconventional hydrodynamic design practices, but simply by ignoring the symmetric constraint normally posed on the wings. In order to do so, it is necessary for the glider to perform a 180° roll when reaching the top of its ascent or the bottom of its dive, a task easily accomplished by rolling the asymmetric ballast by the same angle. By doing so, the glider's surfaces do not switch roles as pressure/suction sides, allowing it to have asymmetric wings, which are beneficial for airfoil and planform optimization and are less sensitive to the Reynolds number. Furthermore, having a non-zero wing incidence angle allows the hull to have a smaller angle of attack in specific configurations, further reducing the total drag of the glider. This could be a concrete innovation, since many of today's gliders use simple thin plates instead of airfoils, and even the most advanced ones only have symmetric airfoils and flat wing planforms. There is also confidence in the results obtained because the design methods and tools that were used are more than adequate for this type of flow: it has been shown time and time again that potential flow and thin airfoil theory work very well for flows dealing with small angles of attack, low Mach numbers and thin bodies. Despite this, some wind tunnel experiments and/or CFD simulations should be advised.

Less confidence can be posed on the design procedure to develop the glider's hull. The main intent was to achieve a mostly laminar flow over its surface. Because of the high computational cost of both 2D and 3D CFD simulations, a more alternative approach was adopted, using a combination of the Myring method to produce hull geometries, the Granville method to predict flow transition and a series of empirical formulas to predict the total drag. This way two different hulls were produced, one which has better hydrodynamic performances and one which suffers more the effects of drag but that has a more convenient volume distribution for the storage

of sensors and ballast. After the two hull concepts were designed, a series of CFD simulations were made, which showed that while the majority of the flow does actually manage to stay laminar, even for larger surfaces than the ones previously predicted, the models used during the design phase were inadequate to estimate pressure drag. So, while the overall design of the two hulls seems to still be quite effective towards the minimization of total drag, their geometries may not represent the ultimate optimization. It is to be noted that, despite some differences, 2D and 3D simulations did provide results similar enough for their comparison to be valid. This leads to the idea that perhaps a more effective optimization could be done with 2D CFD simulations. Initially the method described in Chapter 3 could be used to restrict the field of possible geometries. Then, once a series of viable geometries are obtained, a series of gradient method optimizations could be launched, where the drag coefficient would be predicted with 2D CFD simulations. Since a gradient method would be used, for each iteration only one geometry would need to be simulated. Additionally, even the mesh geometry modification could be automized, since reasonably small changes would occur between each iteration. Again, even with CFD, results can't be blindly trusted, especially because of the unknowns provided by turbulence. The transitional Spalart-Allmaras model provided fairly accurate results in terms of physical phenomena occurring to the flow, but these are not always exact. However, it can be trusted in predicting the trends in flow behavior, and therefore to get close to an optimal design. Approximately, a few hundred simulations would have to be executed, with each requiring five to twenty minutes for an average laptop pc. Therefore, for a slightly more powerful computer the whole optimization process could be done in less than a week.

Another aspect that was not considered was surface roughness. This can become a critical aspect in flow transition and, considering the fact that the AUG is meant to be underwater for consecutive months, it could significantly affect the glider's performances, varying them throughout the lifetime of the mission, as salt buildups accumulate on the hull, possibly increasing the hull's drag but perhaps also improving the wing's hydrodynamic qualities.

Many of these aspects will need to be tested with wind tunnel experiments and perhaps also by building a scaled model to test in water.

Appendix A

Design algorithms

A.1 Hull

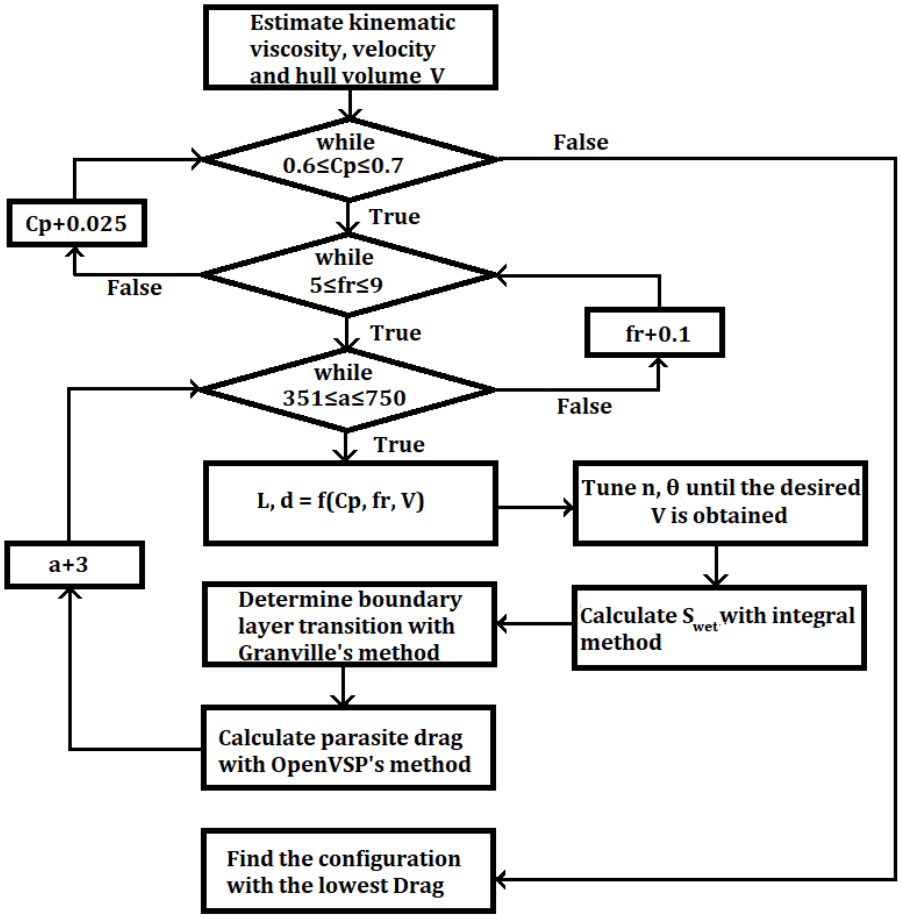

Figure A.1: Hull's design algorithm. V is the volume of the hull, Cp is the prismatic coefficient, fr is the fineness ratio, a is the nose length, L is the total length of the hull, d its maximum diameter, n the nose shape parameter, ϑ the tail angle.

A.2 Wing

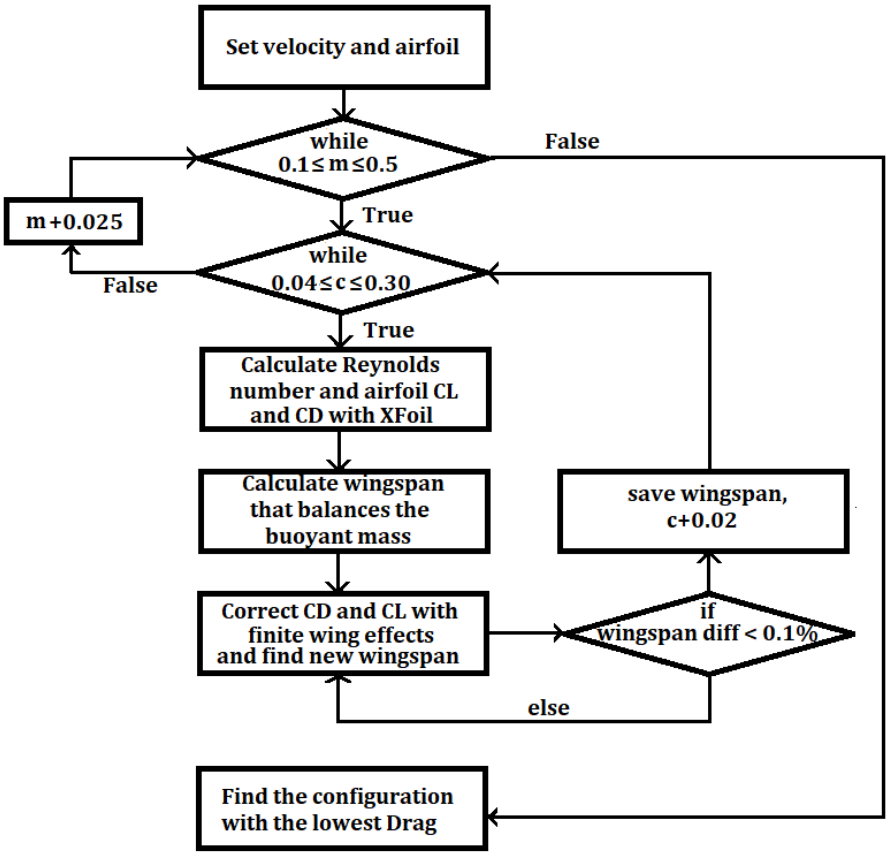

Figure A.2: Wing's design algorithm. m is the buoyant mass, c is the airfoil chord.